TROPOSPHERIC EMISSION SPECTROMETER (TES)

Validation Report

Edited by:
Gregory Osterman

Contributions by:

Kevin Bowman, Karen Cady-Pereira, Tony Clough, Annmarie Eldering, Brendan Fisher, Robert Herman, Daniel Jacob, Line Jourdain, Susan Kulawik, Michael Lampel, Qinbin Li, Jennifer Logan, Ming Luo, Inna Megretskaia, Gregory Osterman, Susan Paradise, Hank Revercomb, Nigel Richards, Mark Shephard, Dave Tobin, Solene Turquety, Helen Worden, John Worden, Lin Zhang

Version 1.00
August 15, 2005

Jet Propulsion Laboratory
California Institute of Technology
Pasadena, California

Table of Contents

Figures

Tables

1 Overview

This document is intended to serve two purposes:

Provide sample results from the effort to validate TES L1B and L2 data products.

Serve as an introduction to the TES data products and how to use them (as of the release date of this document.

Validation is defined, for purposes of this report, as comparison between quantities measured by TES and other data products that represent the state of the atmosphere. This definition will evolve as the validation effort matures. Data used in these figures come from processing at the TES Science Computing Facility and is not necessarily the data released to the public.

The TES L2 nadir products have undergone an initial set of quality control and validation. The effort to validate the TES L2 products is in the process of being expanded and will provide more comprehensive comparisons in the near future. Improved nadir products and initial limb retrievals should be available late in 2005.

Currently, the TES L2 products that are ready for scientific use are the nadir retrievals of ozone, carbon monoxide, temperature and water for ocean target scenes. Land scenes are reported but are not reliable due to a known processing issue that will be corrected in the next data release. In order to compare TES profile data with other measurements, vertical smoothing and sensitivity must be accounted for by applying the appropriate averaging kernels (such as those supplied with the TES data products). The error estimates included in the L2 data products are meaningful based on the current validation analysis. As a means of accounting for systematic errors in L1B radiances, current L2 profiles include the retrieval of a calibration scaling parameter.

The current TES L2 data products available to the public are considered a “beta” release as of July 6, 2005. The nadir products should be upgraded to “provisional” later in 2005. The terms “beta”, “provisional” and “validated” are defined in the appendix section 13.

2 Introduction to TES Data

2.1 TES Data Processing

TES data processing consists of the Level 1A, Level 1B and Level 2 subsystems. L1A produces geolocated interferograms. Radiometrically and spectrally calibrated spectra with Noise Equivalent Spectral Radiance (NESR) are generated by Level 1B. Level 2 produces atmospheric volume mixing ratios (VMRs) and temperature profiles. One or more Product Generation Executives (PGEs) are executed in support of each of these processing levels. HDF product files are generated at Level 1B and Level 2. The TES data processing stages are illustrated in Figure 1.

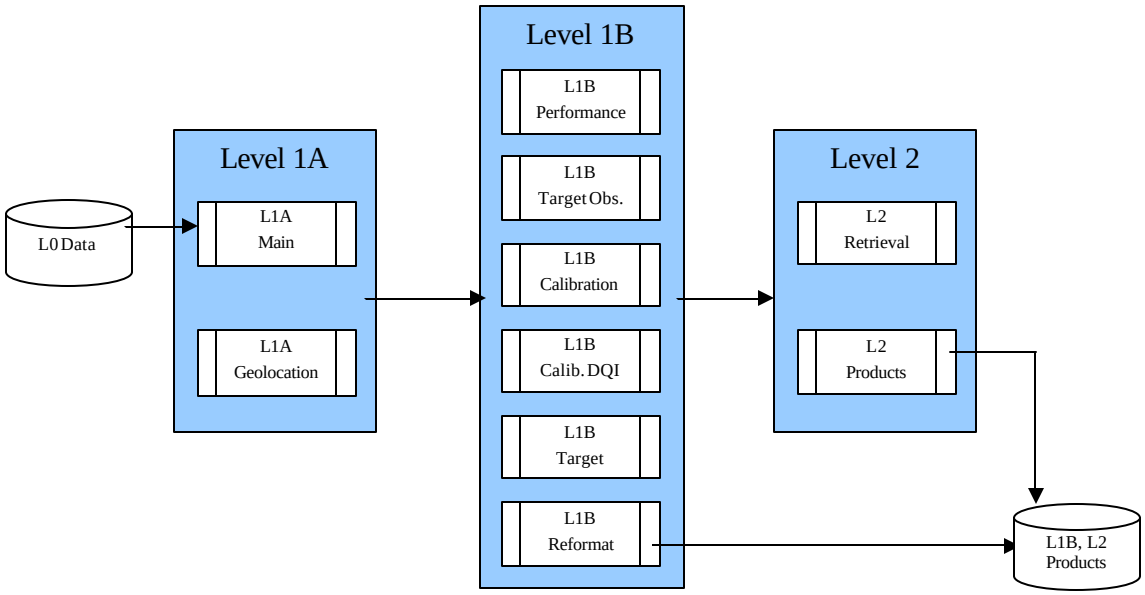

Figure 1: TES data processing stages.

2.2 Using TES Data

The Data Product Specification (DPS) can be found at

http://eosweb.larc.nasa.gov/PRODOCS/tes/DPS/ or

http://tes.jpl.nasa.gov/publications/documents/Data_Product_Spec_R7.doc

HDF product files are generated at Level 1B and Level 2. Level 1B HDF5 products are produced for every focal plane (1A, 1B, 2A and 2B) for each of the 16 orbits of a Global

Survey, for a total of 64 files, approximately 5 - 8 GB. Level 2 produces HDF-EOS5 files for each Global Survey for atmospheric temperature, H_2O, O_3, CH_4 and CO, and an ancillary file, for a total of 6 files, about 1 - 3 GB. Global Surveys are obtained approximately every other day.

Global Surveys (GSs) come in three types:

- Run IDs 2026, 2044, 2092, 2135 and 2345
  - 4 orbits per GS
  - Pairs of nadir observations pointing to the same target scene are averaged at Level 2.
  - Total of 72 pairs of nadir observations per orbit, or 576 nadir observations (288 target scenes) per GS.
- Run IDs 2147 – 2861, excluding 2345
  - 73 Global Surveys in this set
  - 16 orbits per GS
  - Pairs of nadir observations pointing to the same target scene are averaged at Level 2.
  - Total of 72 pairs of nadir observations per orbit, or 2304 nadir observations (1152 target scenes) per GS.
- Run IDs 2931 and above (starting May 21, 2005)
  - Current Global Survey format
  - 16 orbits per GS
  - All nadir observations point to different locations and are processed separately in Level 2.
  - Total of 216 individual nadir observations per orbit, or 3456 nadir observations (3456 target scenes) per GS.

A table of TES Run IDs, corresponding dates and TES observation type is provided in an appendix section (12).

2.2.1 Known issues and advisories:

2.2.1.1 L1B version 02_01

- Pixel 2 of focal plane 1A is dead. Data from this pixel should not be used. The adjacent pixels 1 and 3 for this focal plane are also suspect.
- L1B_General_Quality_Flag and L1B_General_Error_Flag should be combined to determine pixel usability.
- Brightness temperature attribute L1B_Nadir_BT_5 is not reliable.
- Geolocation data has Path_Number = 218 but the L1B-Common metadata has Orbital_Path_ID = 1. These two should match the Aura Path (1-233) at the South Pole crossing. This apparently only occurs in the last file of an orbit. By DPS convention, the orbital path in the metadata is the path number of the first scan following the southern apex.
- TES Level 1B limb data are currently unavailable

2.2.1.2 L2 version 01_01

- TES Level 2 retrievals of methane are currently unavailable.
- TES Level 2 limb retrievals are currently unavailable
- Land scenes are reported but are not reliable due to a known processing issue that will be corrected in the next data release.
- Data is not reported for failed target scenes. Consequently, file sizes will differ between runs.
- The Pressure array contains standard pressures for levels below the surface. These should be fill values. The user is advised to look at another field, such as VMR or Altitude, to determine the index of the surface, which is at the first non-fill value.
- Surface temperature and its error are reported from the last step it was retrieved. It should be reported from the step retrieving it with atmospheric temperature, water and ozone. This results in small errors in the reported surface temperatures, and unreliable reported surface temperature errors.
- SpeciesRetrievalConverged is underreported due to convergence criteria that are currently set too strictly.
- LandSurfaceEmissivity is incorrectly filled in (by initial guess values) for ocean scenes and should be ignored for these scenes.
- The following field is obsolete and contains fill: CloudTopHeight.
- CloudTopPressure is sometimes reported as a value greater than the surface pressure. These locations should be interpreted as being cloud-free.
- The following Ancillary file geolocation fields are obsolete:
    - SurfacePressure: Contains fill. Refer to the Pressure array instead, in the Species files.
    - SurfaceElevation: Contains values that should not be used.

2.2.2 Data Quality

We have identified a set of quality indicators that identify retrievals suspected to have converged to non-optimal solutions. These indicators include a large change of surface temperature from the *a priori* value, large mean or variance of the radiance residual, a large difference between the surface temperature and the lowest atmospheric temperature, and correlations between the radiance residuals and the spectral features of retrieved gases.

By comparing results with two different initial conditions for a global survey dataset, we have tested our quality indicators and estimated that our set of quality indicators reject roughly 75% of non-optimal retrievals and keep roughly 80% of optimal retrievals, where an optimal retrieval is expected to have converged to within the error estimates of the true state.

In an upcoming release the quality indicators will be reported as a master quality flag that will be included in the TES standard product. In the current release, the user can generate some of the flags used for the master quality flag using quantities included in the current TES standard product. Table 1 shows how the user can calculate a quality flag given the

values currently in the TES standard product files. A future release of TES data will contain a single, master flag to determine the quality of a given TES retrieval. The non-grayed values are those that can be calculated using the current release of the TES standard product.

Data product specification value(s) used	Allowed range
Nadir Associated Data Fields, radianceResidualRMS	0 to 1.5
Nadir Associated Data Fields, radianceResidualMean	-0.05 to 0.05
Nadir Associated Data Fields, SurfaceTemperature - Nadir Primary Data Fields, surface value for TATM (first non-fill value)	-15 to15K

Table 1: Shows how the user can calculate a quality flag given the values currently in the TES standard product files

2.3 TES Data for Assimilation, Inverse modeling and intercomparison

2.3.1 Introduction

The TES retrieval algorithm estimates an atmospheric profile by simultaneously minimizing the difference between observed and model spectral radiances subject to the constraint that the solution is consistent with an *a priori* mean and covariance. Consequently, the retrieved profile includes contributions from observations with random and systematic errors and from the prior. These contributions must be properly characterized in order to use TES retrievals in data assimilation, inverse modeling, averaging, and intercomparison with other measurements. All TES retrievals report measurement and systematic error covariances along with averaging kernel and *a priori* vector. We illustrate how to use these TES data with a couple of examples from a simulated CO source estimation and comparison of TES ozone retrieval to the GEOS-CHEM chemical transport model.

2.3.2 Characterization of TES retrievals and comparisons to models

If the estimate of a profile is spectrally linear with respect to the true state then the retrieval may be written as Rodgers, (2000)

$$\hat{\mathbf{y}}_t^i = \mathbf{y}_{t,c}^i + \mathbf{A}_t^i(\mathbf{y}_t^i - \mathbf{y}_{t,c}^i) + e_t^i$$

where $\hat{\mathbf{y}}_t^i$ is a vector containing the vertical trace gas profile at time *t* and location *i*, $\mathbf{y}_{t,c}^i$ is the constraint profile, $\mathbf{y}_t^i$ is the true state of the gas profile, $\mathbf{A}_t^i$ is the averaging kernel, and e_t^i is the observational error. A retrieval characterized by the averaging kernel and constraint vector can be used to quantitatively compare model fields and *in situ* measurements directly to TES vertical profiles. If the model fields are defined as

$$\mathbf{y}_t^{i,m} = \mathbf{F}(\mathbf{x}_t, \mathbf{u}_t, t)$$

where $\mathbf{x}$ is a vector of model fields, $\mathbf{u}$ is a vector of model parameters, e.g. sources and sinks of carbon monoxide, $\mathbf{F}$ is the model operator where the range is defined in terms of volume mixing ratio for trace gases. The *model TES retrieval* for a given trace gas is

$$\hat{\mathbf{y}}_t^{i,m} = \mathbf{y}_{t,c}^i + \mathbf{A}_t^i(\ln \mathbf{F}(\mathbf{x}_t, \mathbf{u}_t, t) - \mathbf{y}_{t,c}^i)$$

The *observation operator* can be written as

$$\mathbf{H}_t(\mathbf{x}_t, \mathbf{u}_t, t) = \mathbf{y}_{t,c}^i + \mathbf{A}_t^i(\ln \mathbf{F}(\mathbf{x}_t, \mathbf{u}_t, t) - \mathbf{y}_{t,c}^i)$$

From the standpoint of the model, the observations are now expressed in the standard additive noise model, Jones et al., (2004):

$$\hat{\mathbf{y}}_t^i = \mathbf{H}(\mathbf{x}_t, \mathbf{u}_t, t) + e$$

The TES ozone retrieval shown in Figure 2 was taken from an observation near the island of Sumisu-jima off the coast of Japan on Sept 20, 2004. The green profile was calculated by substituting the natural logarithm of a GEOS-CHEM model field (2x2.5 degrees) was substituted into the model TES retrieval equation.

Both the GEOS-CHEM model and the TES retrieval indicate elevated amounts of ozone in the upper troposphere. This distribution could be a combination of several chemical and dynamical processes including continental pollution outflow, *in situ* production, or small-scale ozone variability. Quantifying the contribution of these different processes requires assimilation of TES data using tools such as the averaging kernel, constraint vector, and error covariance.

2.3.3 Mapping (interpolation) and the averaging kernel

The averaging kernel, an example of which is shown in Figure 3, is the sensitivity of the retrieved profile to changes in the true state and is composed of 3 matrices:

$$\mathbf{A}_t^i = \frac{\partial \hat{\mathbf{y}}_t^i}{\partial \mathbf{y}_t^i} = \mathbf{M}^i \mathbf{G}_z^i \mathbf{K}_y^i$$

Mapping (interpolation) matrix:

$$\mathbf{y}_t^i = \mathbf{M}\mathbf{z}_t^i, \qquad \mathbf{M} : \circ^M \rightarrow \circ^N, \quad M < N$$

where $\mathbf{z}_t^i$ is a reduced state vector, e.g., a profile on a coarser pressure grid. The mapping matrix projects the retrieval coefficients to the forward model levels. This mapping represents a "hard" constraint on the estimated profile, *.i.e.,* restricts the profile to a subspace defined by **M**.

The second matrix is the gain matrix:

$$\mathbf{G}_z^i = \left(\left(\mathbf{K}_y\mathbf{M}\right)^{\mathrm{T}} \mathbf{S}_n^{-1}\mathbf{K}_y\mathbf{M} + \Lambda\right)^{-1} \left(\mathbf{K}_y\mathbf{M}\right)^{\mathrm{T}} \mathbf{S}_n^{-1}$$

The gain matrix projects the TES observed radiances to the TES estimated profiles based on the, hard constraints **M**, the prior or "soft" constraint Λ, and the TES spectral Jacobian

$$\mathbf{K}_y = \frac{\partial \mathbf{L}}{\partial \mathbf{y}}$$

The averaging kernel is supplied on the forward model pressure grid, which is nominally 87 levels where each level is approximately 1.5 km. The degrees of freedom for signal *(dofs)* for any TES retrieval are significantly less than 87. So, why do we store them on such a fine scale?

Averaging kernel on a fine pressure scale accommodates a variety of grids, e.g., balloons, tropospheric models, stratospheric models, column trace gas observations

Averaging kernel can be reduced without loss of information but not vice versa

Subsequent changes in the retrieval, e.g., changes in M, do not change file format.

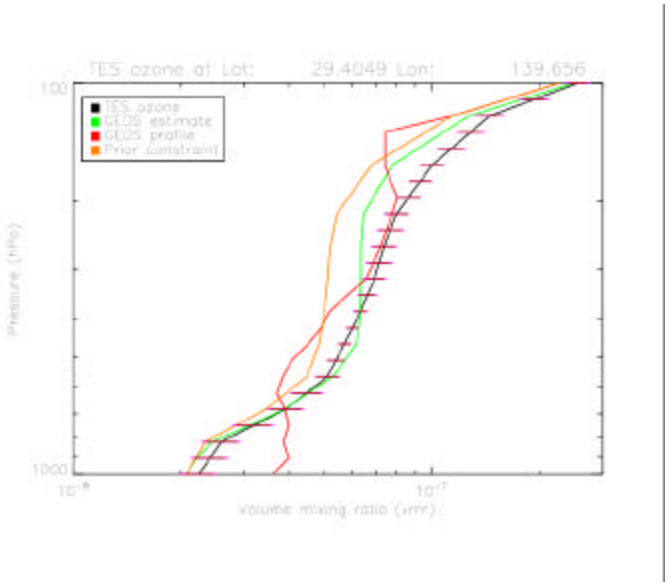

Figure 2: TES nadir ozone retrieval taken from an observation near the island of Sumisu-jima off the coast of Japan on Sept 20, 2004. The green profile was calculated by substituting the natural logarithm of a GEOS-CHEM model field x2.5 degrees) into the model TES retrieval equation.

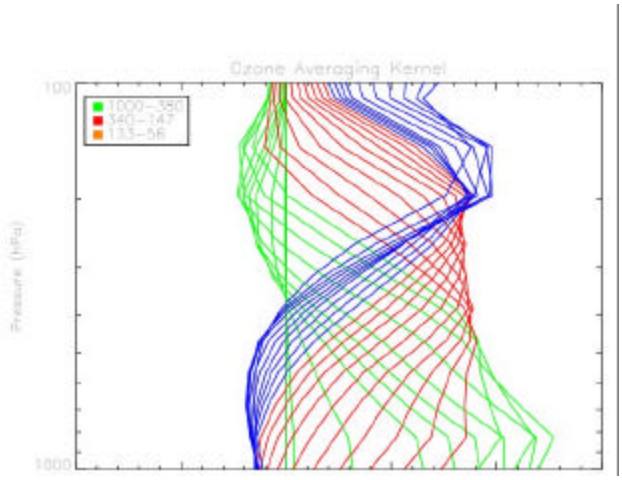

Figure 3: TES ozone logarithm averaging kernel from Sumisu-jima observation. Each vertical distribution is the contribution of the true state to the retrieved state at a given pressure levels. The 3 colors indicate three pressure regimes for which the averaging kernels have similar distributions.

2.3.4 Examples of Mapping

There are a variety of ways to implement mapping with TES data depending on the application. In the case of some chemistry and transport models or *in situ* measurements, the atmosphere is discretized on coarser pressure levels. A simple linear interpolation in logarithm can be used to map these coarser levels to the finer TES levels. This mapping is expressed as:

$$\mathbf{M}_{Trop} : \circ^{P} \rightarrow \circ^{N}$$

where $P < N$. The model retrieval is then

$$\hat{\mathbf{y}}_t^{i,m} = \mathbf{y}_{t,c}^{i} + \mathbf{A}_t^{i}(\mathbf{M}_{Trop} \ln \mathbf{F}(\cdot) - \mathbf{y}_{t,c}^{i})$$

Note that the product of the averaging kernel and the map can be calculated, which results in a smaller matrix. Some instruments produce a column quantity based on scaling a fixed climatological profile. These kinds of data can be compared to the TES retrieval by defining a column vector whose entries are the climatological profile. The mapping looks like

$$\mathbf{M}_c : \circ \rightarrow \circ^{N}$$

This quantity is scaled by the quantity α leading to the equivalent profile retrieval

$$\hat{\mathbf{y}}_t^{i} = \mathbf{y}_{t,c}^{i} + \mathbf{A}_t^{i}(\ln(\mathbf{M}_c a) - \mathbf{y}_{t,c}^{i})$$

This profile can then be compared directly to the TES retrieval.

2.3.5 Conclusions

- TES Level 2 products will include, along with retrievals of atmospheric trace gases, averaging kernels, constraint vectors, and error covariance matrices on the forward model levels
- These tools are critical for comparison of TES retrievals to *in situ* sonde measurements, aircraft and satellite measurements, along with comparison to chemical transport models.
- These techniques enable assimilation systems to properly incorporate TES data by characterizing the constraints and biases used in the retrieval without resorting to expensive and non-linear radiative transfer models

2.4 Cloud Retrievals in TES Atmospheric Retrievals

We have developed an approach to estimate and characterize nadir trace gas retrievals in the presence of clouds. This approach models the radiance contribution of clouds using a

frequency-dependent set of cloud optical depth parameters and a cloud height parameter using a forward model that does not include scattering. The cloud parameters are retrieved from TES spectral radiances jointly with surface temperature, emissivity, atmospheric temperature, and water vapor. We have shown that this approach is applicable to multiple scattering and heterogeneous cloud distributions, and is robust for low water clouds or high ice clouds over a wide range of optical depths. Using simulated data, we have shown that the predicted errors are accurate and that the retrieved values improve over the initial guess. Comparisons between initial TES retrievals of ozone, temperature and water to meteorological fields from NASA Goddard Space Flight Center's Global Modeling and Assimilation Office (GMAO) models, retrievals of temperature and water from the Atmospheric Infrared Sounder (AIRS) on NASA's Aqua spacecraft, and ozone retrievals from the Total Ozone Mapping Spectrometer (TOMS) show that this cloud retrieval approach does not introduce observable biases into TES retrievals.

The choice of cloud parameterization was driven by the desire for analytic Jacobians, computational tractability, and retrieval stability. To ensure computational tractability and retrieval stability we chose to implement a single layer cloud (this assumption can be expanded to multiple layers in the future) and an effective optical depth that is coarsely spaced in frequency by 25 to 100 wave-numbers. The effective optical depth accounts for both cloud absorption and scattering. In order to provide simply calculated analytic Jacobians for the cloud top height, we constrained the cloud to have a Gaussian profile in altitude. Consequently, cloud parameterization can be described as a frequency-dependent layer effective optical depth, t for a layer at pressure $\bar{P}_l$:

$$t(n_c, \bar{P}_l) = k(n_c) e^{-b(\ln \bar{P}_l - \ln P_c)^2} \Delta s$$

where k is the frequency-dependent layer-average effective extinction, b is the Gaussian width parameter, P_c is the cloud altitude (note that this is not frequency dependent) and Δs is the layer thickness. An example of the cloud is shown in Figure 4. Note that $\log(k_n)$ and $\log(P_c)$ are the retrieved parameters.

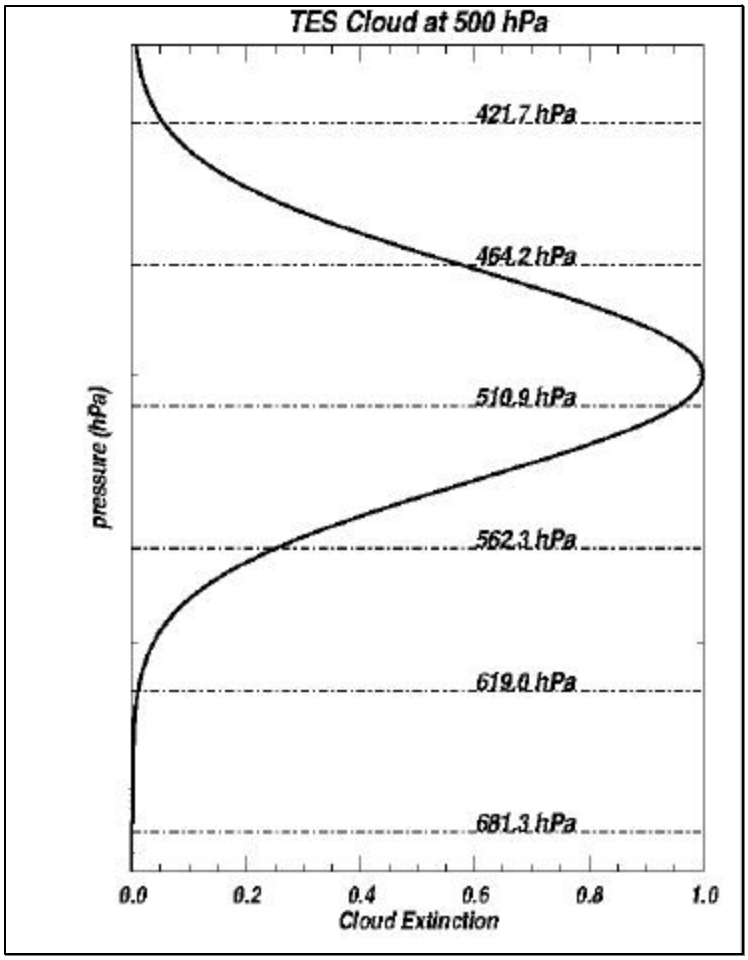

Figure 4: TES cloud at 500 mb. This cloud has non-negligible extinction in about 5 TES forward model layers (shown with dashed lines).

The retrieval of clouds is non-trivial because of the clouds' non-linear effects on the thermal radiance and on the other retrieved parameters. In addition to the forward model calculations, a retrieval strategy is necessary for the retrieval gases in the presence of clouds. The retrieval strategy includes determining the cloud initial guess, possible initial guess refinements, and the creation of a realistic and usable *a priori* covariance and constraint to regularize cloud retrievals. The choice and description of the sources and values of these are discussed in the following paragraphs. Another key component to the retrieval strategy is the decision to retrieve cloud extinction and cloud pressure in log. This allows the non-linear retrieval algorithm the capability of varying cloud extinction over orders of magnitude in the retrieval process, and also passively provides the constraint that cloud extinction is positive.

The cloud effective extinction initial guess and *a priori* are set using the average brightness temperature in the 11 µm region (867.04 - 900 cm^{-1}). The initial guess and *a priori* are set, as shown in Table 1, from the difference between the observed radiance

and a simulated radiance using a cloud-free initial guess based on GMAO temperature and water. The initial guess and *a priori* for cloud pressure are always set to 500 mb. An initial guess refinement step is done if the brightness temperature difference in the 11 µm region described in Section 2.4.1 is greater than 6K. In the refinement step, only the cloud effective extinctions and cloud pressure parameters are retrieved with the rest of the atmosphere fixed to the initial guess. Following this possible step, cloud parameters are retrieved in every step along with the atmospheric parameters of interest. The covariance for cloud effective extinction for TES retrieval and error analysis was created with the assumption that cloud optical depth is highly correlated over all frequencies, and that the cloud's effective extinction varies significantly from target to target. For the first reason, the off-diagonal elements were set to 0.9 * diagonal. For the second reason, the diagonal elements were set to 10 for the covariance of ln(effective extinction). The inverse of this covariance is used as the constraint for cloud effective extinction. The covariance of ln(Pc) is set to 1, which has 1-sigma range of about 183mb – 1300 mb.

Some results are shown that demonstrate that the errors due to our implementation of clouds into the TES forward model are less than the error in TES data, TES simulated retrievals of atmospheric parameters in the presence of clouds are well characterized, and that comparisons to GMAO, AIRS, and TOMS data do not show biases with respect to TES retrieved cloud effective optical depth or cloud height.

To determine the forward model errors which resulted from the cloud parameterization, TES simulated radiances were compared to a model that includes scattering without added noise, using the Code for High-Resolution Accelerated Radiative Transfer (CHARTS) model, (Moncet and Clough, 1997). The resulting radiance residuals indicate the forward model errors that result from our cloud parameterization and show that the effects of clouds of all heights and optical depths on the observed thermal infrared radiation field are adequately modeled by our approach to within the TES data error.

TES retrievals were performed using simulated CHARTS radiances in order to determine if the predicted errors for trace gas retrievals are accurate in the presence of clouds, and if TES can improve on the initial guess in the presence of clouds. Agreement of predicted and actual errors is important because it demonstrates that the errors reported by TES are accurate in the presence of clouds and improvement of the retrieved results over the initial guess in the presence of clouds means that the TES retrievals will add to knowledge of atmospheric composition.

Figure 5 shows results for tropospheric and total ozone columns vs. cloud optical depth and cloud height. The column initial error, retrieved error, and predicted error are shown vs. cloud optical depth and height, showing that the retrieved columns show little or no bias with cloud height and optical depth for the simulated data set, and that the reported errors increase appropriately with actual error. This shows a lack of bias in TES retrievals with respect to retrieved cloud properties, and that the TES reported errors are accurate using simulated data.

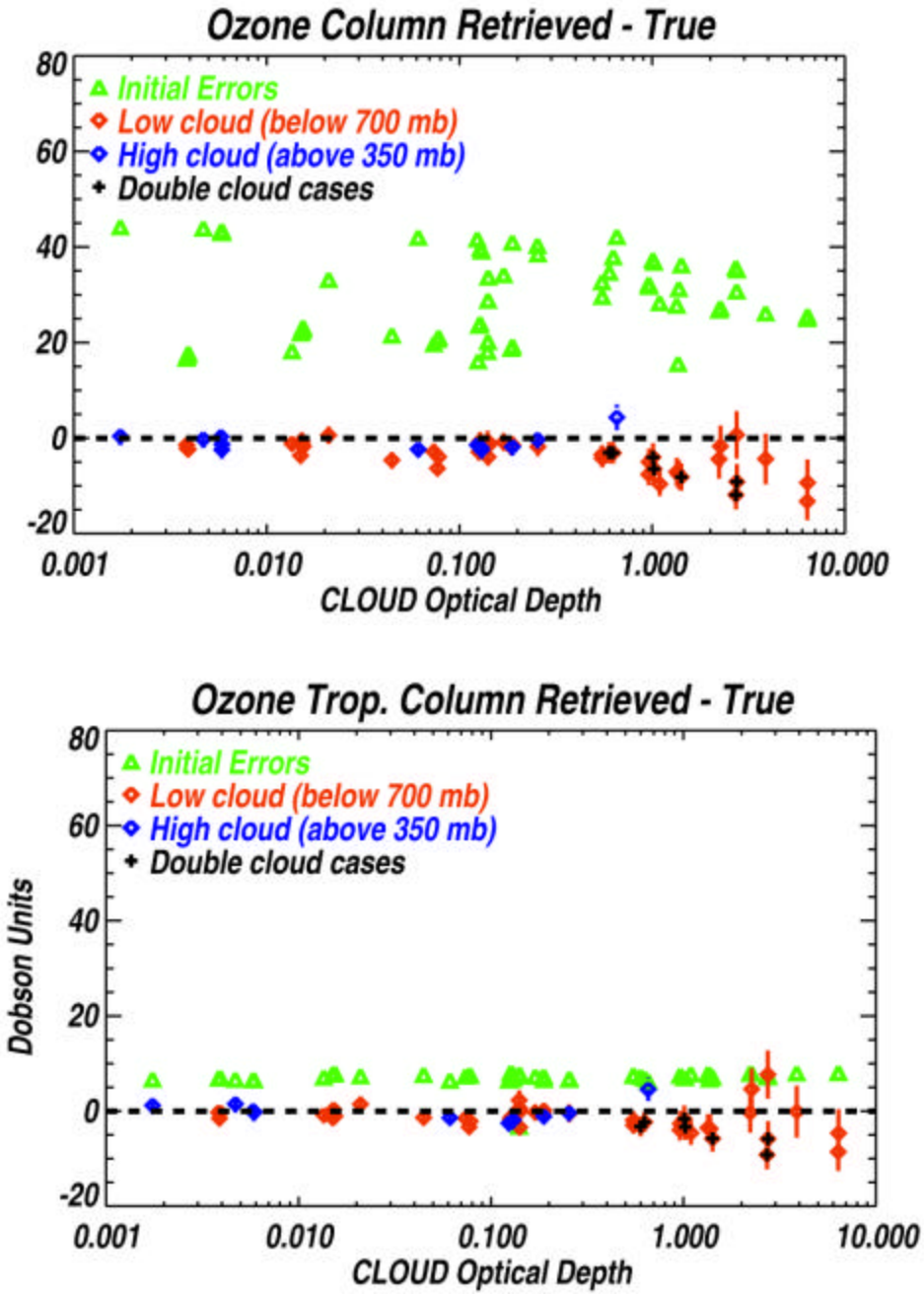

Figure 5: Tropospheric (bottom panel) and total column (top panel) results for simulated ozone retrievals in the presence of clouds. Green shows the initial error, (initial – true), red and blue show the actual retrieved error, (retrieved – true) for low and high clouds respectively, and reported errors are shown as error bars. Note that the error bars increase as the actual error increases. The double layer cloud cases are denoted by (+) and in general have larger errors that are somewhat underreported.

TES results are shown demonstrating TES retrievals in the presence of clouds with data collected by TES from space for some TES "Step and Stare" observations. A "Step and Stare" observation consists of 150 nadir observations spaced approximately 0.4 degrees apart, as shown in Figure. The results with data collected by TES from space validate our cloud approach, parameterization, and retrieval strategy. TES results are compared to TOMS for total ozone column, to GMAO and AIRS for average tropospheric temperature and tropospheric water (from the surface to 100 mb) for a Step & Stare that passes near Ascension Island on September 21, 2004 (TES Run ID 2151). The comparisons are preliminary and are intended to show that there are no biases introduced by the cloud algorithm and retrieval strategy described in this report.

Figure 6 shows TES vs. TOMS total ozone. Although there is a bias with respect to TOMS, there is no apparent dependence on cloud optical depth or height.

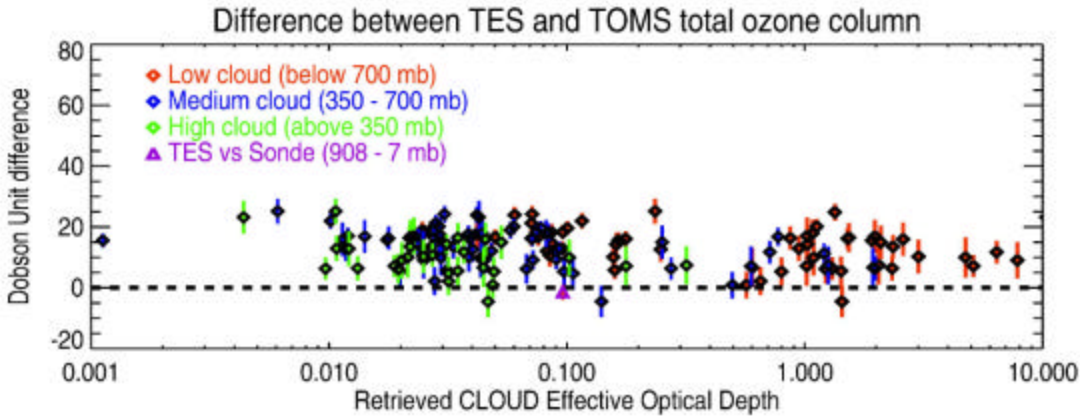

Figure 6: Difference between TES and TOMS results for total ozone column a TES special observation transect near Ascension Island on September 21, 2004. A single sonde comparison (between 908 and 7 mb) is shown in purple. Although there is a bias with respect to TOMS, there is no apparent dependence on cloud optical depth or height. The sonde shows no bias with respect to TES for the single data point.

For the TES vs. AIRS and GMAO comparisons, data was selected for TES completed retrievals (149 cases) and AIRS quality flag 0 or 10 (47 cases) for the closest AIRS retrievals. These same 47 cases were compared to GMAO for temperature linearly interpolated to TES observation latitude, longitude, and time. Although TES uses GMAO for the *a priori* and initial guess, temperature results from TES show a relatively consistent bias of 1.2K with respect to GMAO (Figure 7a). These results show a lesser bias of 0.6K with respect to AIRS data (Figure 7b). However, neither comparison shows a bias with respect to retrieved cloud optical depth or height.

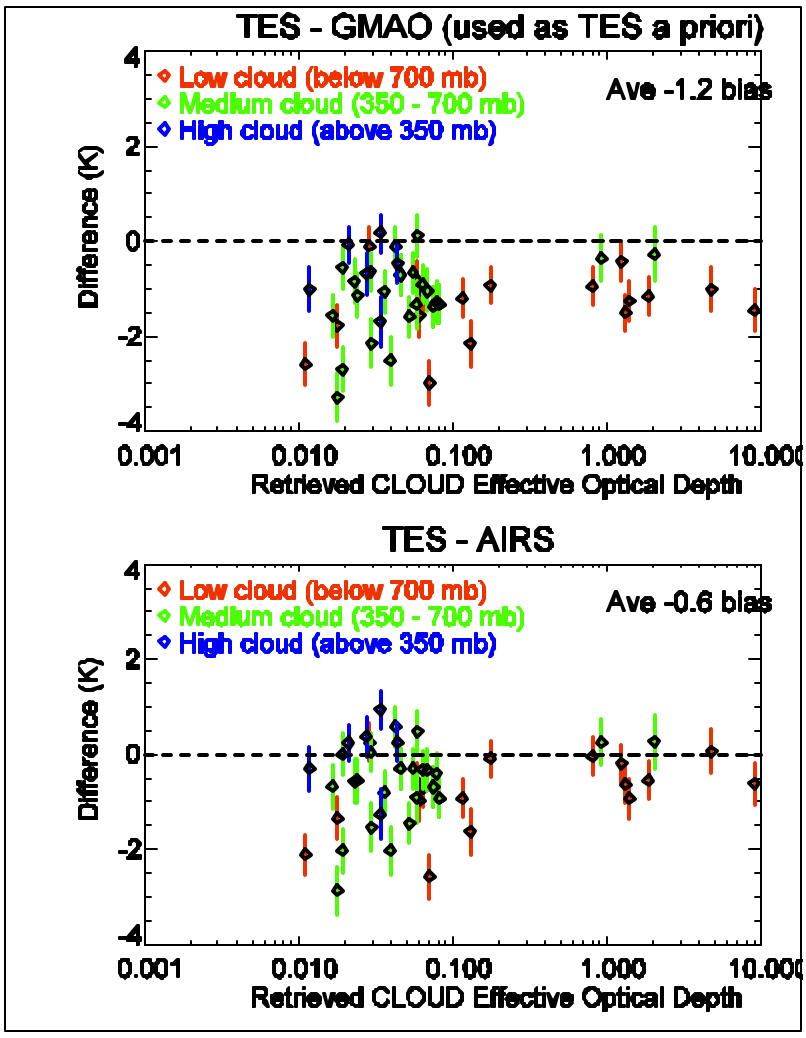

Figure 7: Comparison of average TES Tropospheric temperature to GMAO and AIRS. The TES - GMAO comparison (which is used for the TES a priori), left panel, shows an average 1.2K bias with respect to GMAO. However this bias does not show any trends with cloud height and optical depth. The TES- AIRS comparison show less average bias (0.6K) and also does not show an apparent trend with cloud height or optical depth.

In conclusion, we have determined that TES is able to model clouds in simulation and operationally using a single layer Gaussian shaped cloud with a retrieved effective extinction and cloud pressure. The errors in our forward model from cloud parameterization are less than the TES data noise error. Retrievals of simulated data in the presence of simulated scattering clouds show that TES can improve over the initial guess and that the predicted errors match the actual errors for atmospheric species. Comparisons between TES results and GMAO, AIRS, and TOMS for temperature, water, and ozone show no apparent biases with respect to TES retrieved cloud optical depth or cloud pressure.

3 Executive Summary

Below is a summary of each data validation section.

- Section 4 – TES L1B Radiances: At present, TES L1B data products have systematic errors that need to be resolved and/or mitigated. These errors are both target scene dependent and frequency dependent, especially across the 4 TES focal planes that measure different frequency ranges. The TES L1B nadir radiances have an estimated error of around 2% due to systematic errors. Comparisons between TES L1B radiance spectra and those from Aqua-AIRS show that they agree to less than 1K in brightness temperature. Comparisons between TES and the aircraft instrument Scanning HIS show similar results.

- Section 5 – Ozone: TES ozone profiles have been compared to both ozonesonde measurements and model results. These comparisons show a consistent bias toward larger ozone concentrations in the upper troposphere measured by TES even after applying the TES averaging kernels. In addition, comparisons of TES total column ozone with TOMS show a 5% bias, with TES measuring more ozone. The source of these systematic biases is currently under investigation.

- Section 6 – Water Vapor: TES total column water vapor is 10% drier than AMSR-E and AIRS. Comparison of the water vapor profiles from TES and AIRS show that most of the difference in the column is accounted for by the 700-900mb layer. Initial comparisons of TES water retrievals show good qualitative agreement.

- Section 7 – Atmospheric Temperature: Initial comparisons of AIRS and TES temperature profiles show that the temperature profiles agree to within 2K, The vertical structure of the difference between TES and AIRS profiles is consistent from day to day.

- Section 9 – Carbon Monoxide: Initial comparisons have been carried out between TES carbon monoxide retrievals and those from Terra-MOPITT. The results show that for pressure layers where both instruments are most sensitive, the retrievals agree to within roughly 10%. Comparisons to the aircraft instruments show agreement within the estimated TES retrieval errors.

4 Validation of TES L1B Radiances

4.1 TES L1B Radiance Validation – Comparison with AIRS

Initial validation of TES L1B radiances was performed by comparing calibrated TES radiances with AIRS radiances in regions of spectral overlap. Since AIRS radiances have be validated to 0.1 K in brightness temperature (Hagan *et. al.* 2003, Pagano *et. al.* 2003), they provide an established radiance reference. The range of spectral overlap between TES and AIRS is approximately 655-1135 cm^{-1}, which spans two TES filters.

Using TES global survey data taken on September 20-21, 2004, we first selected a small subset of the data in which the inter-pixel variability was very small, indicating a uniform target area (uniformly clear or cloudy). The subset of data was then further reduced by requiring that the corresponding AIRS footprint also show a uniform target area. The resulting data set contains 50 TES target scenes spanning the 16 orbit TES global survey time period and containing a variety of target radiance levels. Since TES has much higher spectral resolution than AIRS, the spectral resolution of the TES radiances was reduced to match the AIRS resolution by convolving the TES spectra with the AIRS spectral response function. An example target is shown in Figure 8 and Figure 9 for the TES filters 2B1 (650-950 cm^{-1}) and 1B2 (925-1135 cm^{-1}) for a single TES pixel. The top panels show the full resolution TES spectra with the AIRS and convolved TES spectra over-plotted in brightness temperature units. The middle panel shows the AIRS and convolved TES spectra without the distraction of the full resolution spectra. The lowermost panel shows the difference between the AIRS and the convolved TES spectra along with our expected noise equivalent delta temperature (NEDT) limits.

Since the screening process necessary to ensure minimal target scene differences between TES and AIRS is so difficult, this type of comparison can only be made on a limited basis. The comparison sets, however, have proved useful in helping the TES team determine and correct errors in the TES calibration methodology.

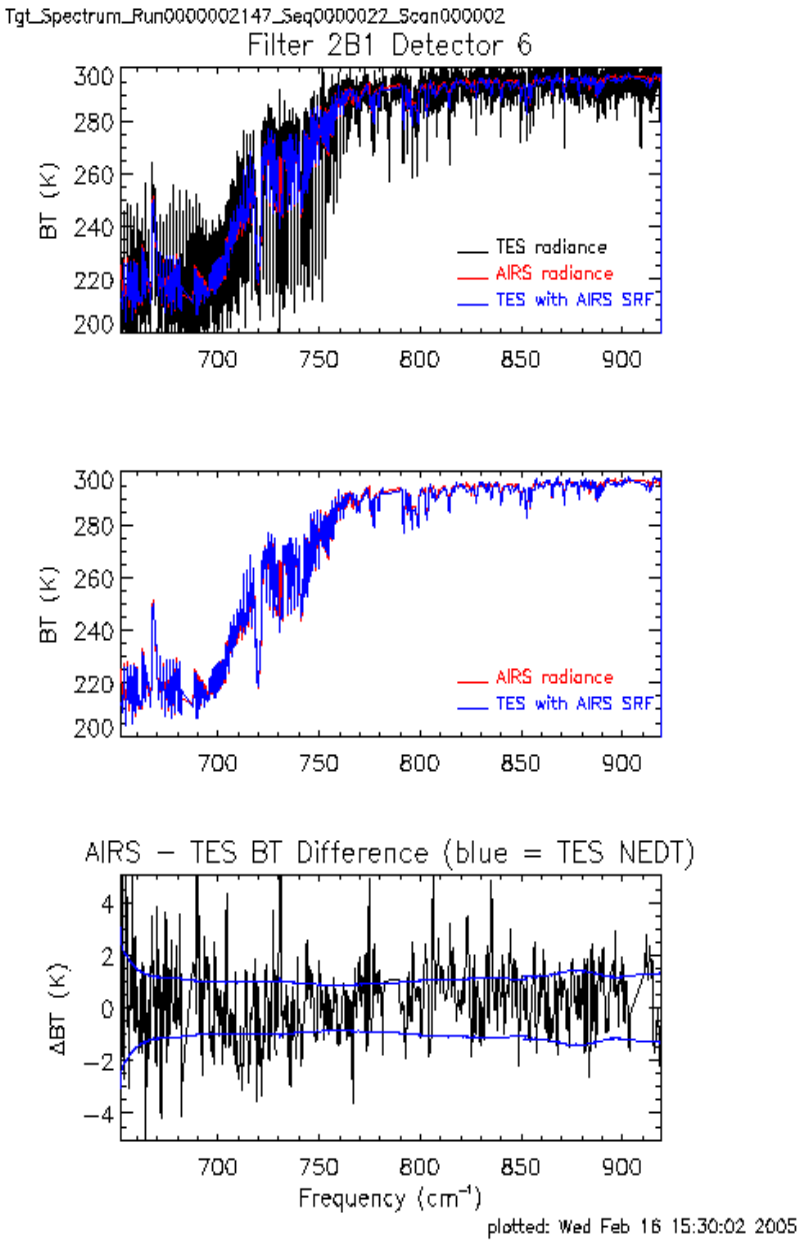

Figure 8: Comparison between TES radiances and AIRS radiances for a single pixel from a single target scene for detector 2B1, covering the range of 650-920 cm-1. The top panel shows the full resolution TES spectrum (black) in brightness temperature units with the AIRS radiance (red) and TES radiance with the AIRS spectral response function applied (blue). The middle panel shows the comparison between the AIRS radiance (red) and TES radiance with the AIRS spectral response function applied (blue) without the distraction of full resolution TES spectrum, illustrating good general agreement. The bottom panel shows the difference (in Kelvin) between the AIRS and TES radiance with the AIRS spectral response function applied (black) with the TES noise equivalent delta temperature (NEDT) overplotted (blue) for reference.

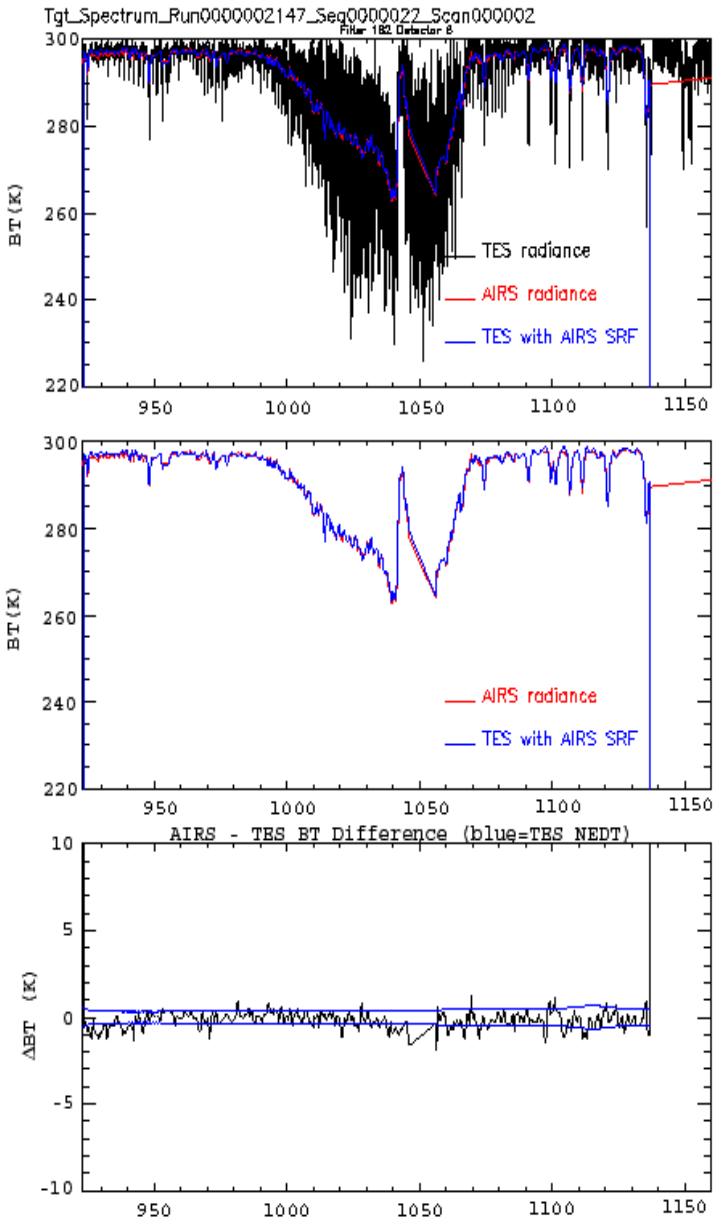

Figure 9: Comparison between TES radiances and AIRS radiances for a single pixel from a single target scene for detector 1B2, covering the range of 925-1160 cm-1. The top panel shows the full resolution TES spectrum (black) in brightness temperature units with the AIRS radiance (red) and TES radiance with the AIRS spectral response function applied (blue). The middle panel shows the comparison between the AIRS radiance (red) and TES radiance with the AIRS spectral response function applied (blue) without the distraction of full resolution TES spectrum, illustrating good general agreement. The bottom panel shows the difference (in Kelvin) between the AIRS and TES radiance with the AIRS spectral response function applied (black) with the TES noise equivalent delta temperature (NEDT) overplotted (blue) for reference.

4.2 Summary of TES Spectral Radiance Validation with Scanning-HIS Underflights

4.2.1 The Scanning-HIS

This section provides an introduction to the Scanning-HIS including an overview of its design and calibration approach. The Scanning-HIS is a follow-on of the original University of Wisconsin HIS (Revercomb et al. 1988a, 1988b, 1996) that was flown successfully on the NASA ER2 aircraft from 1986 to 1998. Its design and calibration techniques have matured from experience with the HIS and from the ground based Atmospheric Emitted Radiance Interferometer (AERI) instruments developed for the DOE Atmospheric Radiation Measurement (ARM) program. The nadir-only spatial sampling of the original HIS has been replaced by programmable cross-track coverage with similar ~2 km footprints, while at the same time the Scanning-HIS is smaller, more robust, and easier to operate. In addition to the NASA ER2, the Scanning-HIS has been successfully flown on the NASA DC8, the Scaled Composites Proteus, and most recently on the NASA WB-57. Applications of the data include satellite validation, development and validation of clear and cloudy sky absorption models, retrieval of atmospheric state, surface, and cloud properties, and design trades and risk reduction for future satellite sensors.

The basic components of the Scanning-HIS include a scene mirror module, telescope, Michelson plane mirror interferometer, aft optics, detector module with mechanical cooler, laser metrology, calibration blackbodies, and on-board signal processing and solid state storage. Figure 10 is a diagram of the Scanning-HIS opto-mechanical layout. Following the basic optical flow, scene radiance incident on a 45 degree gold-coated scene mirror passes through an afocal telescope, through the interferometer, and is focused at the entrance to the detector module where a field stop is located. The field stop limits angles through the interferometer to 40 mrad (full angle). The telescope has an a focal ratio of 2.5 resulting in a 100 mrad spatial field of view, producing 2 km diameter nadir footprints from an altitude of 20 km. A 4.5 cm aperture stop is located on the fixed mirror of the interferometer, and its image is focused onto the detectors via refractive optics within the detector assembly. The detector package is a “sandwich” configuration with three physically overlapping detectors with a shared focal plane, eliminating the need for multiple coolers and dichroic beamsplitters and providing a compact and simplified optical design. All three detectors share the same physical field and aperture stops. Two high emissivity calibration blackbodies, one at flight ambient temperature (ABB) and one maintained at an elevated temperature (HBB), are viewed by rotation of the scan mirror. The scan mirror sequence is programmable; the sequence used for the TES validation cases presented here consists of 13 cross track earth scene views followed by 5 HBB views and 5 ABB views. On the Proteus and WB-57, zenith view data may also be collected. Wavelength separation is provided by a dynamically aligned plane mirror interferometer with a voice coil driven linear slide mechanism. A stable HeNe metrology laser source and detectors are introduced along the center of the interferometer optical axis for fringe counting and for dynamic alignment of the fixed mirror. The scan speed is 4 cm/s and the maximum optical path difference (MOPD) is

±1.037 cm, resulting in the collection of an interferogram with spectral resolution (1/2/MOPD) of about 0.48 cm^{-1} (FWHM ~ 0.58 cm^{-1}) every 0.5 s. The raw interferograms from each view are compressed in real time using a numerical filter and decimation process performed on a digital signal processor (DSP), while a second DSP is used for controlling the instrument.

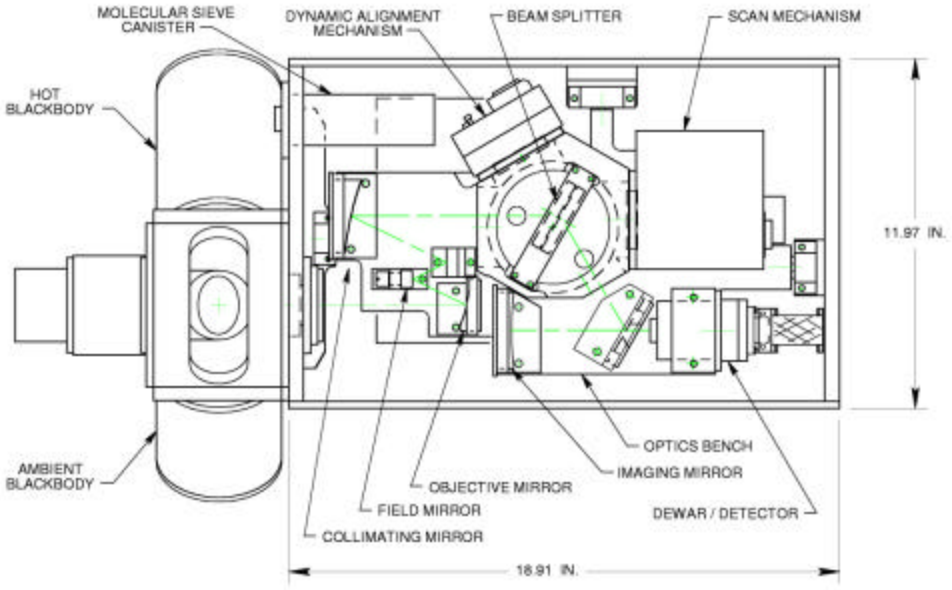

Figure 10: Diagram of the Scanning-HIS opto-mechanical design viewed from the nadir perspective. The dashed grey line is the optical axis.

As with the original HIS and ground-based AERI instruments, accurate calibration has been a primary objective of the Scanning-HIS. For a comprehensive description of the AERI calibration approach and algorithms, which are very closely related to those used for the Scanning-HIS, the reader is referred to Knuteson et al. (2004a, 2004b). Accurate radiometric calibration of the Scanning-HIS is achieved primarily by frequent viewing of the on-board blackbody calibration references. The ABB is unheated but is thermally coupled to the aircraft pod temperature while the HBB is maintained at approximately 310 K when in-flight. The onboard blackbodies were built at the University of Wisconsin Space Science and Engineering Center with NIST traceable calibration and have formal 3 sigma (i.e. not to exceed) absolute uncertainties for temperature and cavity emissivity of 0.10 K and 0.001, respectively (Best et al. 1997, 2003). Linear calibration using these references and proper handling of phase is achieved following the complex calibration approach introduced by Revercomb et al. (1988a). Nonlinearity corrections are applied to the photo-conductive HgCdTe longwave and midwave band complex spectra following the same general approach used for the AERI instruments.

Perturbation analysis of the radiometric calibration shows that the Scanning-HIS has formal 3-sigma (not to exceed) absolute radiometric uncertainties of less than 0.15 K for scene brightness temperatures greater than 250 K.

In addition to the on-board calibrations, characterization tests are performed at the University of Wisconsin before and after field campaigns to verify radiometric nonlinearity, spectral calibration, and other issues relevant to the calibration. The pre- and post-deployment efforts typically include blackbody thermistor and electronics calibration, blackbody alignment verification, views of external calibration targets (LN_2 bath and high emissivity blackbodies at various temperatures), analysis of out-of-band harmonics, and comparisons of ground-based zenith view data with coincident clear sky data measured by an AERI. Along with other analyses, the character and magnitude of the radiometric nonlinearity of the longwave and midwave bands (and the linearity of the shortwave InSb band) are characterized using these data. A check of the Scanning-HIS calibration by direct comparison to a NIST-maintained TXR radiometer is planned for later this calendar year. Previous comparisons of the University of Wisconsin designed blackbodies against NIST maintained standards have shown agreement to within 0.03 K over a range of blackbody temperatures (Minnett et al. 2001).

Accuracy of the in-flight data is also assessed directly by inspection of the imaginary part of the calibrated spectra, inspection of spectral regions of detector band overlap (1030-1200 cm^{-1} and 1760-1810 cm^{-1}), and inspection of numerous housekeeping variables. Recently added is the ability to collect and record 128 unfiltered interferogram data points (bypassing the numerical filter and decimation processes) centered on zero optical path difference, allowing the out-of-band harmonics to be monitored. When flying on the Proteus and WB-57 aircraft, zenith view sky spectra collected from high altitude can serve as a pseudo space view and is used to assess the calibration in spectral regions with low opacity.

Spectral integrity of the Scanning-HIS spectra is achieved through use of a stable HeNe metrology laser, which provides fixed interval optical path difference sampling. Self-apodization effects are removed based on the optics geometry (yielding constant spectral resolution and lineshape as a function of wavenumber) and the spectra are resampled to a standard wavenumber grid following the same approaches as used for AERI. The absolute spectral calibration is determined by adjusting the effective metrology laser frequency to create optimal agreement with the positions of well-known spectral features present in clear sky calculated spectra. Analysis of ensembles of such cases (Tobin et al. 2003) has determined the Scanning-HIS spectral calibration with an uncertainty of ±0.5 ppm (3 sigma uncertainty in the mean) with no detectable changes with time.

4.2.2 Scanning-HIS underflights of TES

The Scanning-HIS has participated in the October/November 2004 and June 2005 AVE missions on the high altitude NASA WB-57 aircraft, with the primary objective of providing validation of the TES spectral radiance observations. Other objectives include tropospheric ozone sensing and TES ozone product validation, upper level water vapor,

and surface emissivity studies. Validation of the TES spectral radiances with the Scanning-HIS is achieved by underflying AURA at high altitude (~20 km) and comparing the collocated Scanning-HIS and TES observations. Adjustments are made to account for the differing spectral resolutions and viewing geometries of the two sensors. This same approach has been used to provide accurate and detailed assessment of the AIRS spectral radiance observations (Tobin et al. 2005).

Several good underflights for radiance validation were obtained during AVE 2004. Figure 11 shows the Scanning-HIS mounted on the left wing pod of the WB-57 during AVE 2004. The AVE 2004 flight tracks are summarized in Figure 12. TES was just coming out of safe mode at the end of AVE 2005 and no data was therefore collected for TES radiance validation during this mission. The AVE 2004 flights on October 31 and November 7 included clear sky underflights of TES over the Gulf of Mexico. Preliminary TES/Scanning-HIS comparisons for these cases have been created and are presented below.

Figure 11: The Scanning-HIS installed on the left wing pod of the WB-57 during AVE 2004.

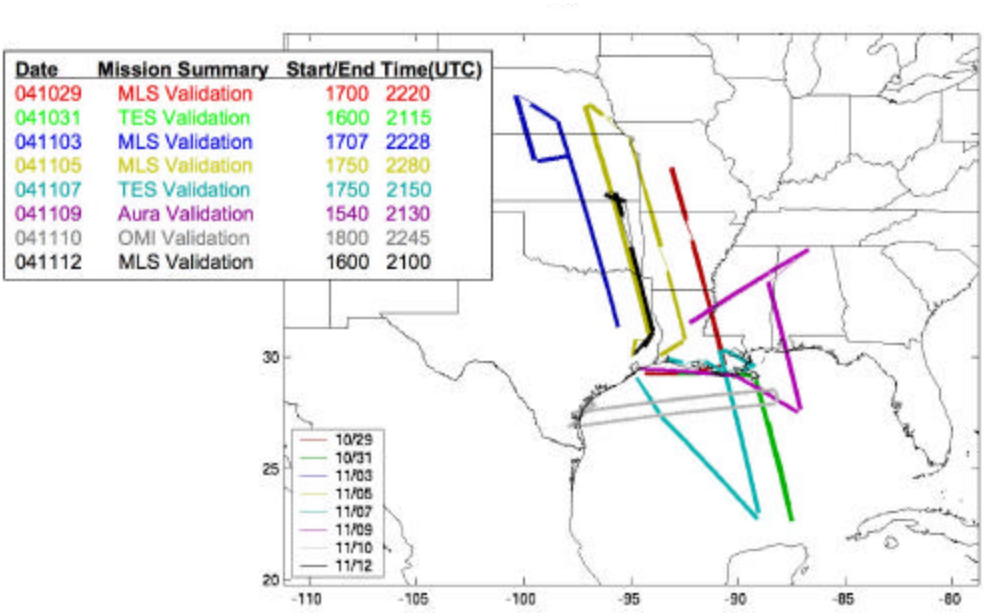

Figure 12: AVE 2004 flight tracks.

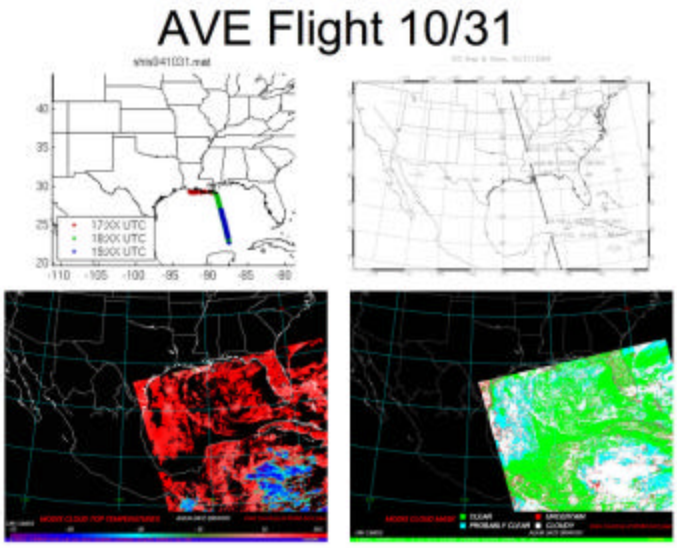

Figure 13: Scanning-HIS flight track (upper left), TES footprints (uppe r right), and MODIS cloud top temperature (lower left) and cloud mask (lower right) for the October 31 flight.

4.2.3 Scanning-HIS / TES comparisons

4.2.3.1 October 31, 2004

A good validation case was obtained on October 31 2004, with mostly clear sky scenes encountered over the Gulf of Mexico. Figure 13 presents some of the details from this flight. Figure 14 shows a spatial map of the Scanning-HIS window region brightness temperatures along the flight track, overlaid with three TES footprints. These footprints, scans 0, 5, and 6, of this Earth view sequence, contain mostly clear sky ocean with some small scale low altitude cumulous clouds. S-HIS/TES collocation times for these scans range from 6 to 14 minutes.

Figure 15, Figure 16 and Figure 17 show comparisons of Scanning-HIS and TES radiance spectra for TES scans 0, 5, and 6. For these comparisons, the TES footprints are represented as 8x5 km rectangles, and the mean of all the Scanning-HIS footprints within the TES footprint is computed and compared to each TES spectrum. The TES spectra are reduced to the Scanning-HIS spectral resolution. For the comparisons presented here, no adjustments are made to account for the different viewing altitudes and scan angles of the two sensors.

Figure 16 demonstrates that the agreement between Scanning-HIS and TES is good (< 1K) in the center of the 2A1 spectral band. Figure 17 shows comparisons of Scanning-HIS and TES band 1B2, Scanning-HIS and TES band 2A1, and TES bands 1B2 and 2A1. For each comparison, histograms of observed brightness temperatures from each sensor for a given wavelength region are compared. A detailed of the comparisons for all three scans and for spectral bands 1B2 and 2A1 show that 1) the agreement between TES in the 1B2/2A1 spectral overlap region is variable, on the order of +/- 0.5 K from scan to scan, and similarly 2) the agreement between Scanning-HIS and TES on the edges of spectral bands 1B2 and 2A1 is also variable, of nearly the same magnitude.

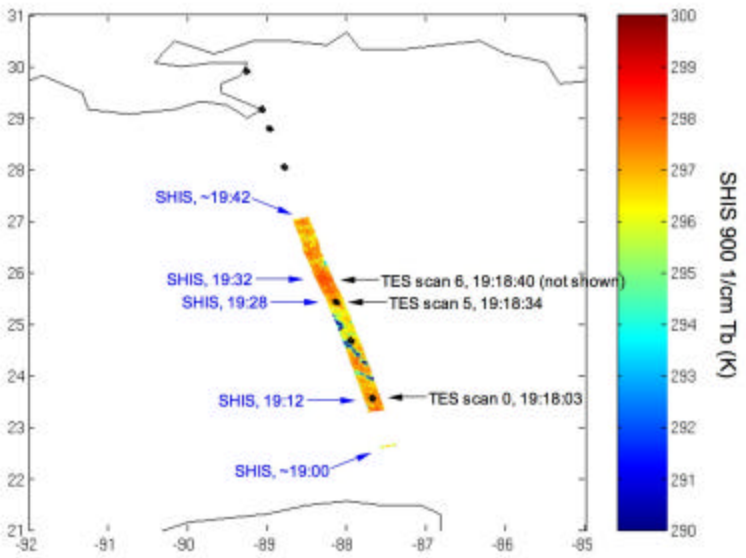

Figure 14: Map of Scanning-HIS window region brightness temperatures overlaid with the locations of selected TES footprints.

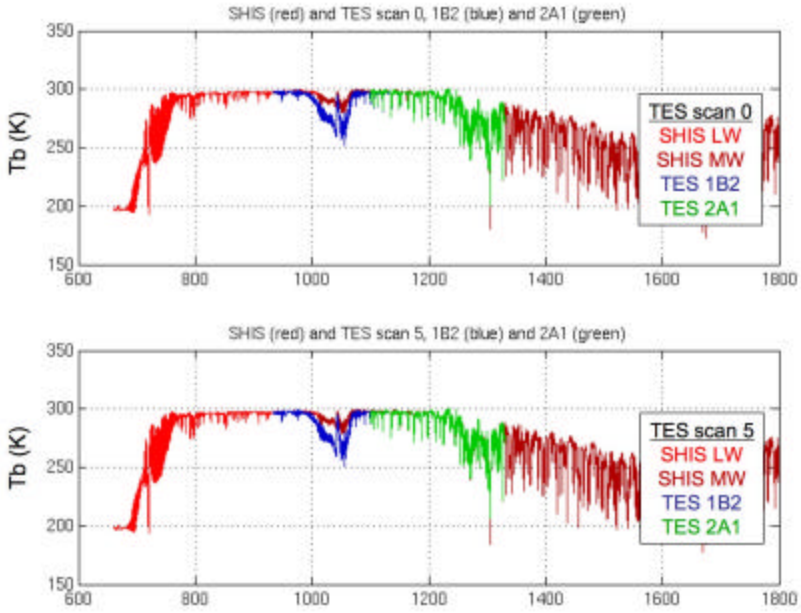

Figure 15: Comparisons of Scanning-HIS and TES spectra for TES scans 0 and 5 and spectral bands 1B2 and 2A1.

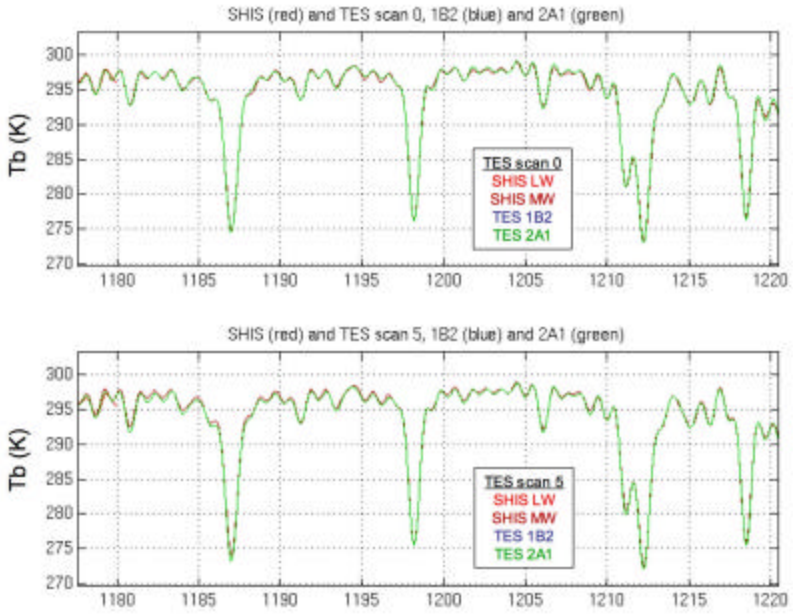

Figure 16: Comparison of Scanning-HIS and TES band 2A1.

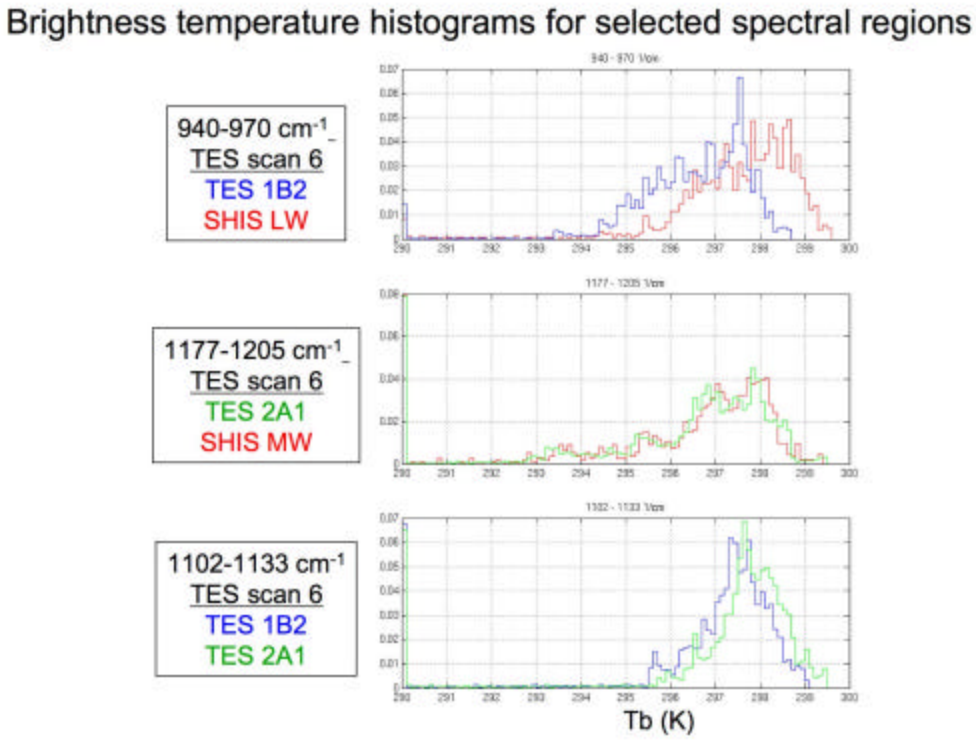

Figure 17: Comparisons of Scanning-HIS and TES band 1B2, Scanning-HIS and TES band 2A1, and TES bands 1B2 and 2A1.

4.2.3.2 November 7, 2004

Analogous to the previous section, this section presents comparisons of Scanning-HIS and TES spectra obtained on November 7, 2004. This underflight also occurred over the Gulf of Mexico, with very clear sky conditions. Figure 18 and Figure 19 present the logistics of the case, and Figure 20 through Figure 25 show the comparisons. The findings are similar to the October 31 case: 1) agreement on the order of 1K or better is found between Scanning-HIS and TES, 2) the agreement between TES in the 1B2/2A1 spectral overlap region is variable, on the order of +/- 0.5 K from scan to scan, and similarly 3) the agreement between Scanning-HIS and TES on the edges of spectral bands 1B2 and 2A1 is also variable, of nearly the same magnitude. Also, at the Scanning-HIS spectral resolution, no signs of spectral calibration errors are observed in the comparisons.

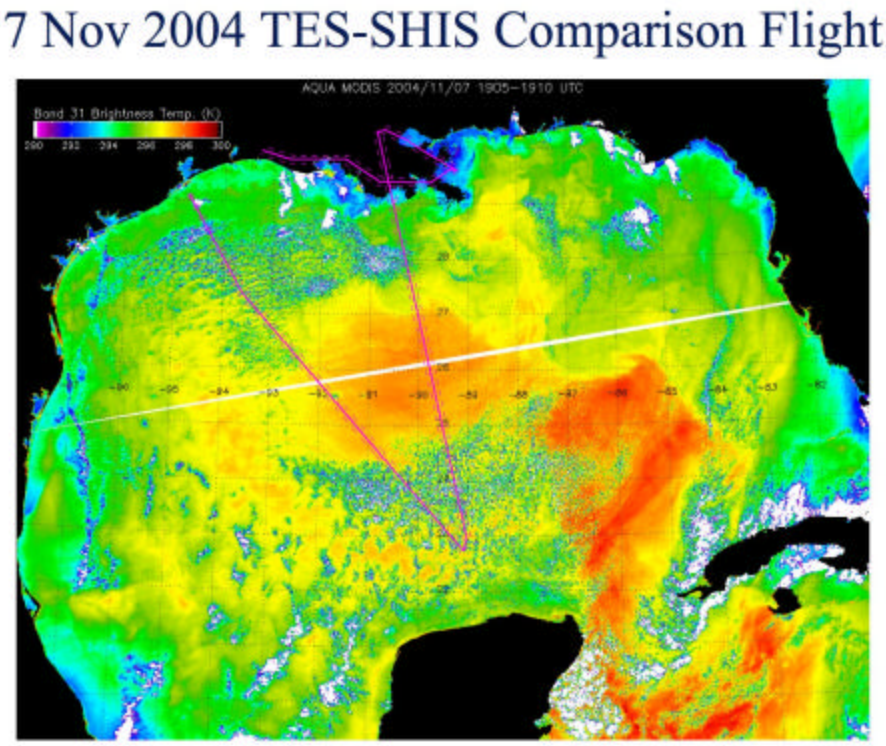

Figure 18: The flight track (magenta line) for the November 7 flight overlaid on a MODIS window region brightness temperature image. The northbound (eastern) flight leg is coincident with the TES nadir track.

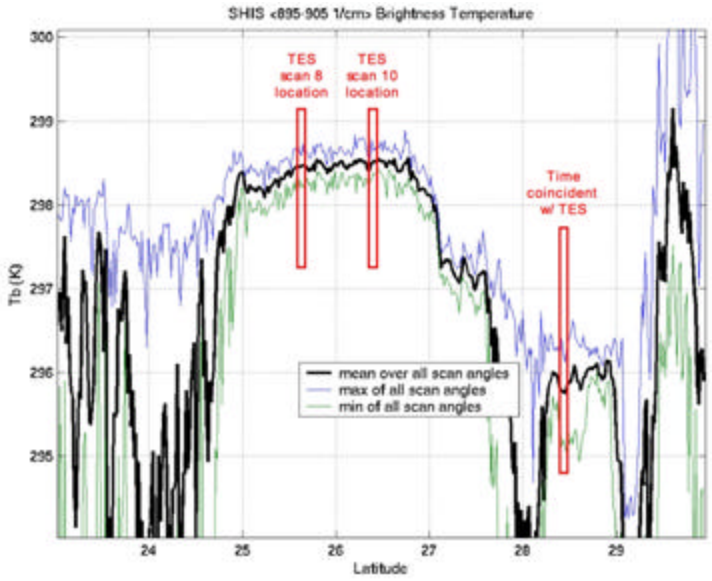

Figure 19: Scene variability along the northbound flight leg, overlaid with the positions of selected TES scans.

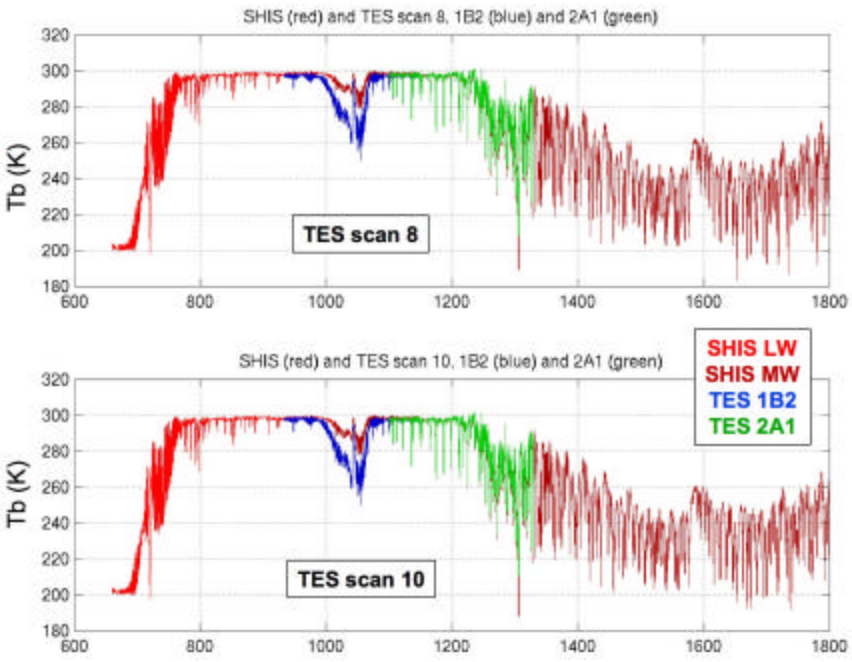

Figure 20: Comparisons of Scanning-HIS and TES spectra for TES scans 8 and 10 and spectral bands 1B2 and 2A1.

Figure 21: Comparison of Scanning-HIS and TES spectra for scans 8 and 10 for band 2A1.

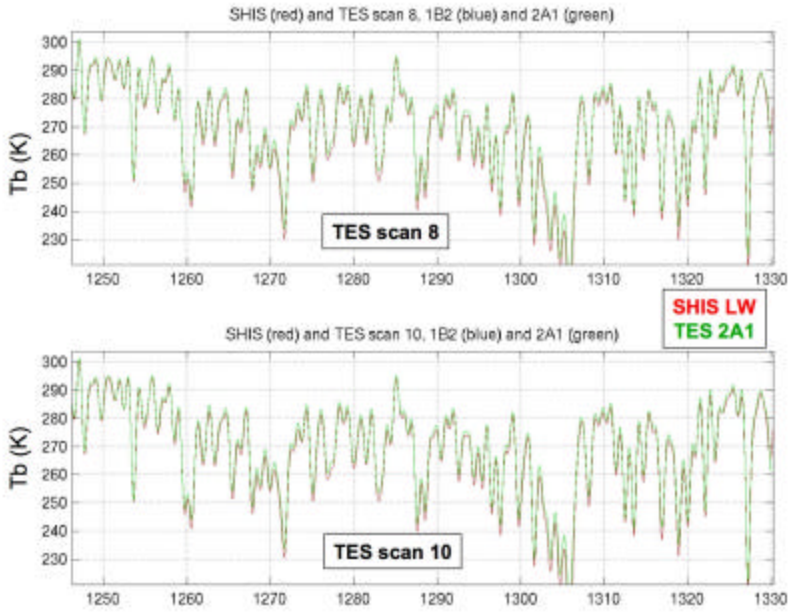

Figure 22: Comparison of Scanning-HIS and TES spectra for scans 8 and 10 for band 2A1.

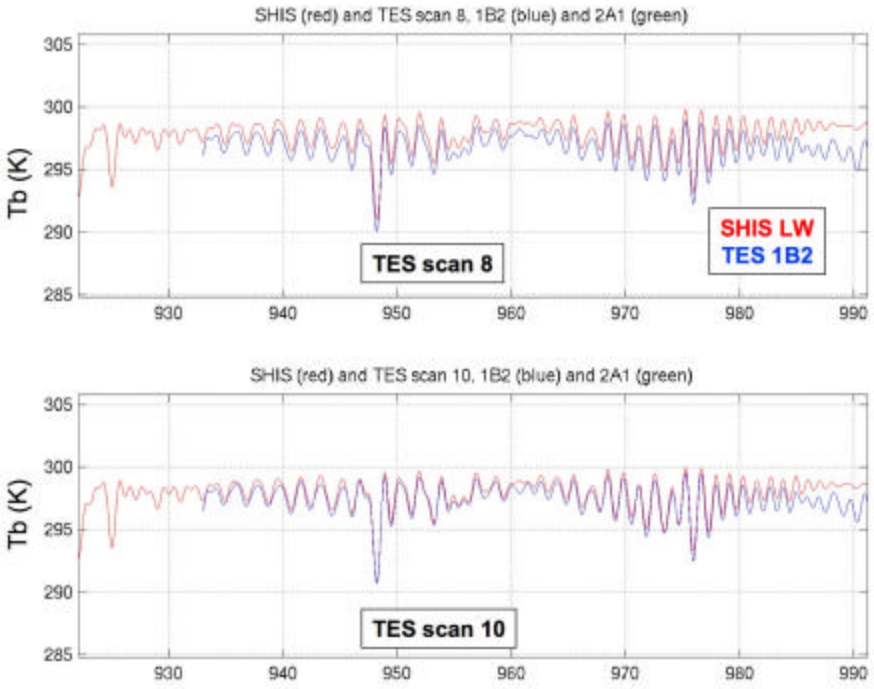

Figure 23: Comparison of Scanning-HIS and TES spectra for scans 8 and 10 on the edge of TES band 1B2.

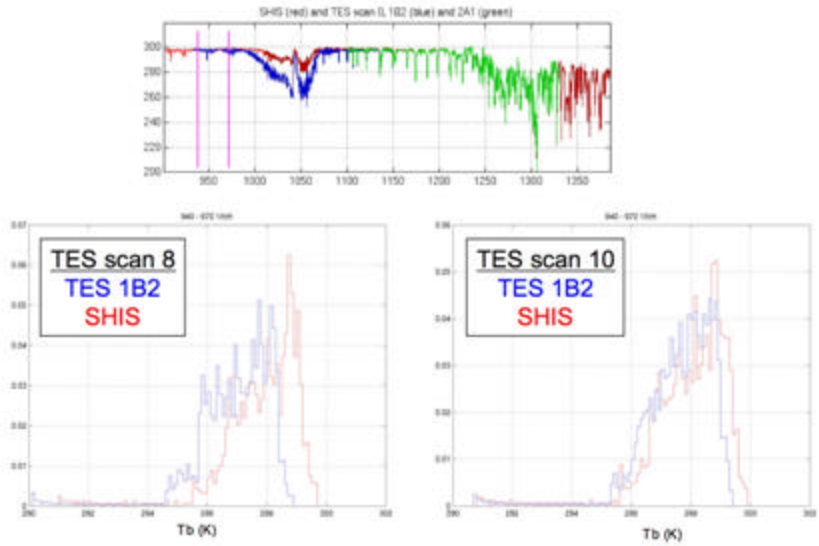

Figure 24: Histograms of Scanning-HIS and TES radiances within the 940-970 1/cm spectral range, on the edge of TES band 1B2.

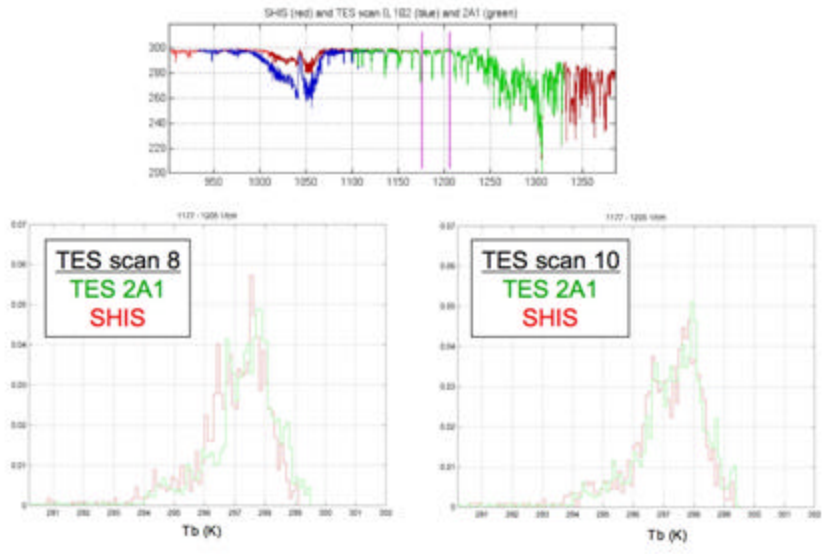

Figure 25: Histograms of Scanning-HIS and TES radiances within the 1177-1205 1/cm spectral range, on the edge of TES band 2A1.

4.2.4 Summary

The Scanning-HIS has participated in the AVE 2004 and 2005 field campaigns with a primary objective of providing an assessment of the TES spectral radiance accuracy. Preliminary analyses of two clear sky cases from AVE 2004 collected over the Gulf of Mexico have been performed. The Scanning-HIS / TES comparisons show agreement on the order of 1 K, but also show Scanning-HIS / TES differences and TES-1B2 / TES-2A1 brightness temperature differences on the order of +/- 0.5 K on the edges of the spectral bands which are variable from scan to scan. We consider these differences to be significant and warrant investigation into the underlying cause and development of correction algorithms.

5 Validation of TES Level 2 Ozone

5.1 TES Total Ozone Column

TES measures ozone through the regions of the troposphere and stratosphere where the vast majority of atmospheric ozone is found. As a result, TES can make a determination of the total column ozone abundance. In order to examine the quality of the total ozone measured by TES, total column ozone amounts determined by TES have been compared to data from the Total Ozone Mapping Spectrometer (TOMS). A typical comparison is made from data for a TES "Step & Stare" special observation on January 22, 2005 (Figure 26). This comparison is typical and shows a consistent bias of about 5% between the column values measured by TES and TOMS. The data from this particular TES special observation was taken mostly over ocean. Differences between land and ocean do not seem to affect the bias that we see between TES and TOMS data. It should be noted that despite the fact that TES sees consistently higher column values that TOMS, both instruments show similar structure in the ozone column as a function of latitude. This is true for nearly all comparisons done between the instruments to date.

A comparison for several TES special observations from January, 2005 is shown in Figure 27. The figure shows that the bias is consistent over the latitude range 40°S to 40°N with the difference being somewhat less in the southern hemisphere and increasing as latitude increases in the northern hemisphere. The data in Figure 27 include land and ocean target scenes, as well as day and night observations.

Another comparison is shown in Figure 28 which shows data from a TES global survey taken on September 20-21, 2004. The results are similar to those seen in the January 2005 special observations. The discrepancy between TES and TOMS clearly gets worse as latitude increases to the North.

The cause for the discrepancy between the two instruments is still under investigation. The bias could be due to a combination of factors, both the bias in the upper troposphere seen by TES and the calibration error affecting TOMS likely contribute. Also these comparisons do not take into account the fact that TES and TOMS are sensitive (or lose sensitivity) to ozone over different regions of the atmosphere. A more thorough comparison using TES averaging kernels and including the effects of the *a priori* information used by the two instruments is currently underway.

Comparisons with other instruments that measure total ozone column amounts, such as SBUV and OMI are also in progress but not presented in this version of the TES validation report.

5.2 TES Tropospheric and Stratospheric Column Values

Because TES is sensitive to ozone in several layers of the atmosphere it is possible to make a determination of the column ozone abundance in the troposphere and

stratosphere. In this version of the TES validation report we do not show any of the results of validation of the TES tropospheric column determinations. We are currently working at getting a better characterization of the errors in column values, particularly those associated with the location of the tropopause.

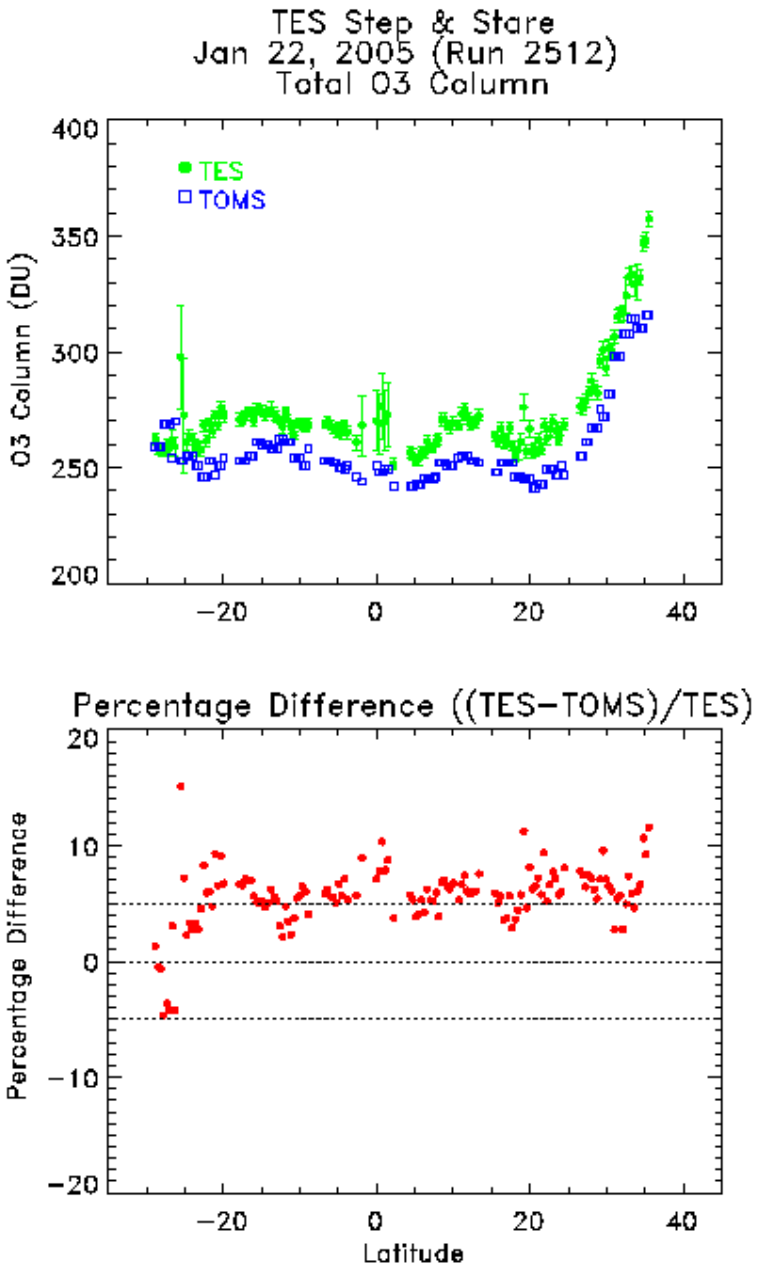

Figure 26: TES total column ozone for measurements made on January 22, 2005. The TOMS data are the values closest to the location of the TES footprint.

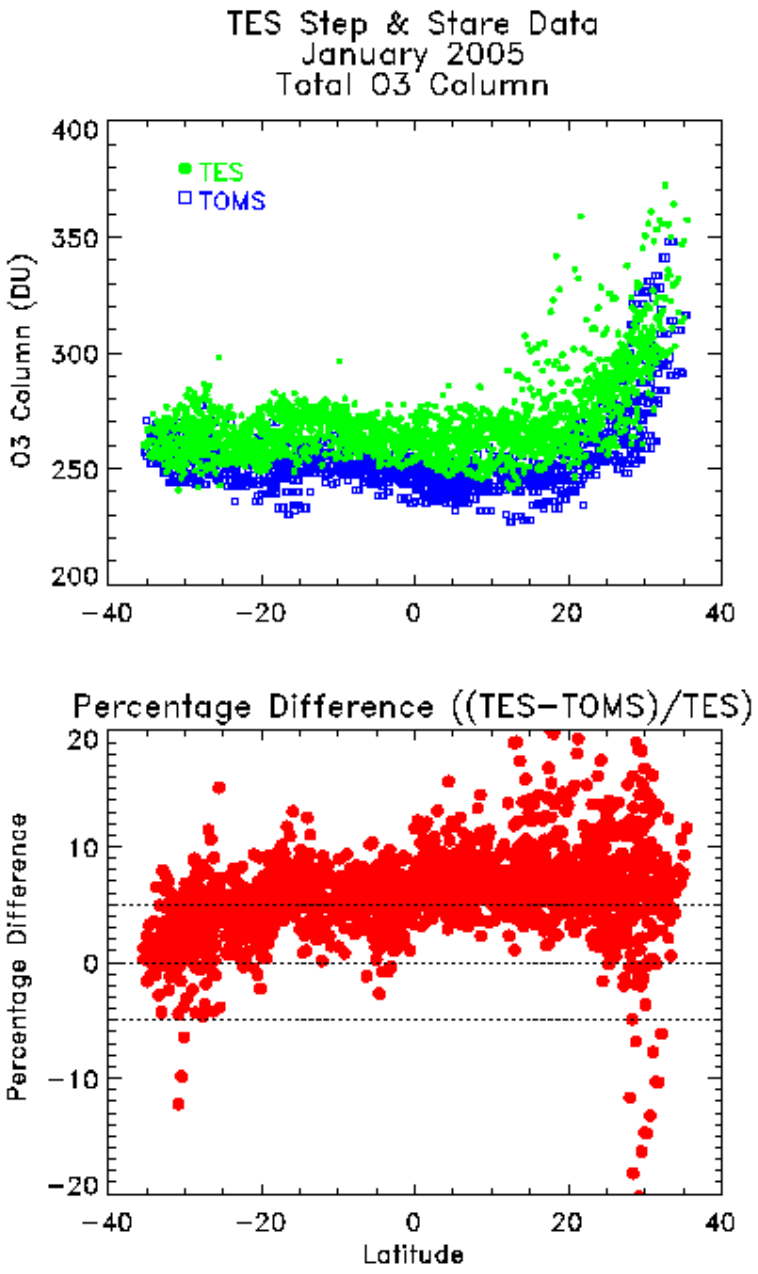

Figure 27: Comparison between TES and TOMS data from 16 special observations for the time period January 22-26, 2005.

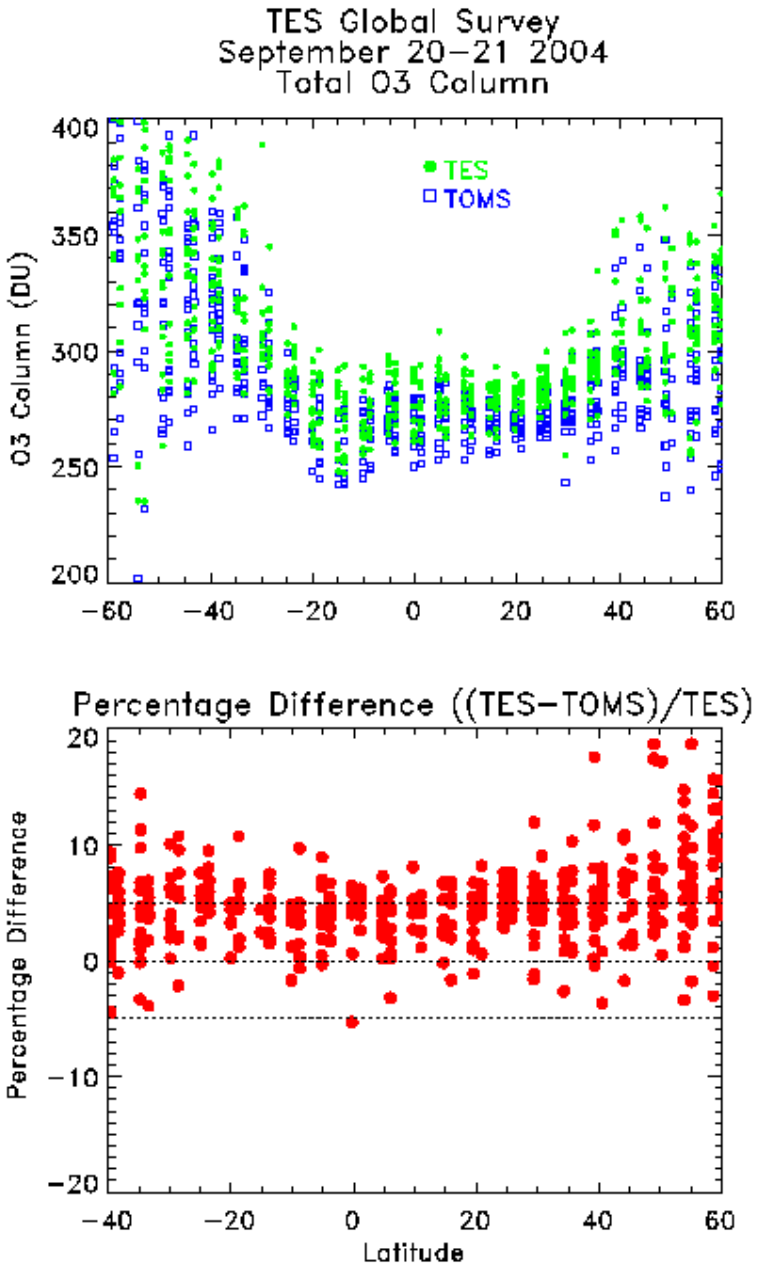

Figure 28: Figure similar to Figure 26 only for a TES Global Survey from September 2004.

5.3 Comparison of TES Ozone Profiles to Ozonesondes: Methods and Initial Results

5.3.1 Introduction

Ozone profiles are retrieved from TES infrared radiances with roughly 6 km vertical resolution for nadir observations. The principal source of validation for TES O3 retrievals are ozonesonde measurements. In some cases, we have sonde data from dedicated launches to match the Aura overpass, while other comparisons are performed with standard data available from the SHADOZ and WOUDC networks. In order to make TES-ozonesonde comparisons, we must account for TES measurement sensitivity and the disparities in vertical resolution. This is done by applying the TES averaging kernel and constraint to the ozonesonde profile.

5.3.2 Ozonesonde data provided to the TES Science Team.

Jennifer Logan et al. at Harvard University obtained and processed all the ozonesonde data from September 1, 2004, onwards (Table 2) that were available from four sources: the World Ozone and Ultraviolet Data Centre (WOUDC; http://www.woudc.org), the SHADOZ data archive (Thompson et al., 2003; http://croc.gsfc.nasa.gov), the NOAA/CMDL ozone measurement program (S. Oltmans, personal communication), and the NASA/Wallops ozone measurement program (F. Schmidlin, personal communication). These data were processed into a common data format, quality checks applied, and the data provided as ASCII files in April and May, 2005. More data have become available in the past 2-3 months, but these later data have not yet been obtained and processed. In addition, there are now sonde data available at WOUDC for September-December, 2004, for: Edmonton, Churchill, and Eureka (Canada), and Syowa (Antarctica). There are also now data at the SHADOZ site for all of 2004 and part of 2005 for: Paramaribo, San Cristobal, Watukosek, Fiji, Reunion, and a new site, Cotonou, Benin (6ºN, 2ºE). None of the data mentioned were available at the Aura Validation Data Center (AVDC, http://avdc.gsfc.nasa.gov) when they were given to the TES team. The SHADOZ data were posted at AVDC starting in June, but the other sonde data are not yet at AVDC. It is clear that there are many potential opportunities for validation of TES and other Aura instruments using the sonde data.

Gary Morris of Valparaiso University provided the ozonesonde launches and data during the Fall 2004 AVE campaign out of Houston, TX with corresponding sponsorship from the Shell Center for Sustainability and NASA's IONS program. Mike Newchurch of the University of Alabama in Huntsville also provided ozonesonde launches and data during the Fall 2004 AVE campaign.

Name, Country	Lat.	Long.	Alt.	Data Source	WOUDC ID No.	Last Date[1] Provided	Last Date[2] as of Jul. 9
Lindenberg, Germany	52	99	112 m	WOUDC	174	2005/02/23	2005/03/30
Hohenpeissenberg Germany	47.8	11.01	975 m	WOUDC	99	2005/02/28	2005/05/30

Name, Country	Lat.	Long.	Alt.	Data Source	WOUDC ID No.	Last Date[1] Provided	Last Date[2] as of Jul. 9
Payerne Switzerland	46.5	6.6	490 m	WOUDC	156	2004/12/29	
Sapporo, Japan	43.06	141.3	19 m	WOUDC	12	2005/01/31	2005/04/27
Trinidad Head, USA	40.8	-124.2	0 m	S. Oltmans	4xx	2005/03/02	
Boulder[3] USA	39.95	-105.25	1743 m	S.Oltmans	67	2004/12/28	
Wallops Is. USA	37.9	-75.5	14 m	F. Schmidlin	107		
Tateno, Japan	36.06	140.1	31 m	WOUDC	014	2004/01/31	2005/04/27
Huntsville, USA	35.28	-86.59	196 m	S.Oltmans	418	2005/03/26	
Kagoshima, Japan	31.58	130.57	157 m	WOUDC	7	2005/01/26	2005/03/30
Naha, Japan	26.2	127.68	27 m	WOUDC	190	2005/01/25	2005/04/27
Hilo, Hawaii USA	19.43	-155.04	11 m	S. Oltmans	109	2004/12/28	
Sepang Airport Kuala Lumpur[4]	2.73	101.7	17 m	WOUDC SHADOZ	443	2004/12/01	2005/06/20
Nairobi, Kenya	-1.27	36.8	1745 m	SHADOZ	175	2005/03/22	
Natal, Brazil	-5.84	-35.21	32m	SHADOZ	219	2005/03/29	2005/06/28
Ascension Is.	-7.98	-14.42	91 m	SHADOZ	328	2004/11/17	2005/06/28
Samoa	-14.23	-170.56	10 m	SHADOZ	191	2005/02/09	
Irene, South Africa	-25.56	28.19	1524 m	SHADOZ	265	2005/04/04	2005/05/25
Lauder New Zealand	-45.04	169.68	370 m	WOUDC	256	2004/12/22	
Neumayer Antarctica	-70.	-8.22	38 m	WOUDC	323	2005/04/06	2005/06/22

1. Last date for which data were provided to the TES team in April-May, 2005.
2. No date is given if there are no measurements beyond those given in the previous column.
3. Data for 2005 are available but are not yet normalized to the ozone column, which the earlier data are.
4. In the SHADOZ archive, this site is referred to as Kuala Lumpur, but is called Sepang Airport at WOUDC.

Table 2: Sonde data provided for TES validation.

5.3.3 Comparison Methods

In comparing TES O3 profiles with ozonesonde data, we can neglect the averaging kernels associated with the sonde profiles since they would be close enough to the identity matrix due to the fine vertical sampling. (This would not be possible for comparisons to other remotely sensed data, as shown in C. Rodgers and B. Connor, 2003.)

The procedure for applying the TES averaging kernel to the sonde measurements is as follows:

1. Map O3 sonde profile to the TES 87 pressure level grid;

$$\mathbf{x}_{sonde}^{pTES} = \mathbf{M}_{pTES \Rightarrow Psonde}^{-1} \mathbf{x}_{sonde}$$

2. Apply averaging kernel, A_{TES}, and *a priori* constraint:

$$\mathbf{x}_{sonde}^{TES_{AK}} = \mathbf{x}_{apriori} + \mathbf{A}_{TES}[\mathbf{x}_{sonde}^{pTES} - \mathbf{x}_{apriori}]$$

3. Compare to TES profile using the measurement and cross-state error terms. The total error estimate is:

Where **A** is the averaging kernel, **M** is a linear mapping matrix on pressure levels, **G** is

$$\mathbf{S}_{\%} = \quad \text{(Total Error Covariance)}$$

$$(\mathbf{A}_{xx} - \mathbf{I})\mathbf{S}_a(\mathbf{A}_{xx} - \mathbf{I})^T + \quad \text{(Smoothing Error)}$$

$$(\mathbf{A}_{xx_{CT}})\mathbf{S}_a^{x_{CT}x_{CT}}(\mathbf{A}_{xx_{CT}})^T + \quad \text{(Cross-Term Error – includes T, H2O for joint retrieval with O3)}$$

$$\mathbf{M}\mathbf{G}_z\mathbf{S}_n\mathbf{G}_z^T\mathbf{M}^T + \quad \text{(Measurement Error)}$$

$$\sum_i \mathbf{M}\mathbf{G}_z\mathbf{K}_b^i\mathbf{S}_b^i(\mathbf{M}\mathbf{G}_z\mathbf{K}_b^i)^T \quad \text{(Systematic Errors)}$$

the gain matrix and **K** is Jacobian matrix. (See C. Rodgers, 2000, J. Worden, *et al.*, 2004 and K. Bowman *et al.,* 2005 for more details on notation and definitions). Figure 29 shows the TES averaging kernel for a tropical nadir view near Ascension Island.

5.3.4 TES comparisons to ozonesondes for Fall 2004

Table 1 lists the sonde stations with sufficient coincidence to TES measurements, nominally 600 km and 4 hours, but some exceptions are also included. Table 1 includes average differences (in ppbV) for the upper troposphere (UT) and lower troposphere (LT). Those given for lower troposphere are for the surface to 500 mb. Average differences given for the upper troposphere are for 500 mb to the tropopause, (as defined by the lapse rate in TES temperature profiles with a minimum pressure of 100 mb), or the lowest sonde pressure, for sondes that did not reach the tropopause such as those launched in Houston for the AVE campaign.

Figure 30, Figure 31 and Figure 32 show selected comparison examples. Figure 33, Figure 34 and Figure 35 show the ensemble of comparison differences in ppbV, relative difference and error-weighted difference, respectively.

5.3.5 Conclusions

Figure 33, Figure 34 and Figure 35 show a consistent bias in the upper troposphere for large O3 values as measured by TES, even after accounting for vertical smoothing and sensitivity. The figures also show reasonably good agreement in the lower troposphere. For ozonesondes that were launched during Aura overpasses in September and October, 2004, specifically for early validation studies of the TES nadir ozone product, we found that the coincident profile for Ascension Island (9/21) was typical for the tropical south

Atlantic in austral spring, but the Natal profiles (9/20 and 10/20) were relatively low for the season, as shown in Figures 20 and 21. Thus the three profiles gave a range of values for validation purposes. The first validation showed that TES was able to discriminate between the higher Ascension profile and the lower Natal profiles in the middle troposphere.

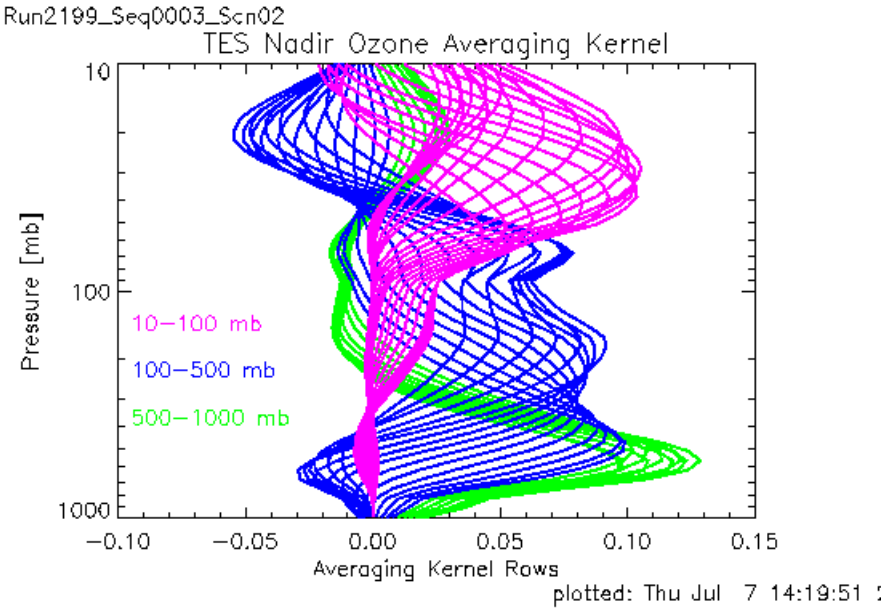

Figure 29: Example of TES ozone averaging kernel for nadir view in tropics (near Ascension Island).

Sonde Station	**Sonde location (lat/lon deg.)**	**TES ID run seq, scan**	**TES time (date UTC)**	**Dtime TES-sonde (hr)**	**Ddist (km)**	**Avg. diff sonde-TES in upper troposphere (ppb)**	**Avg. diff sonde-TES in lower troposphere (ppb)**
Payerne	47 N/ 7 E	2147 388 2/3	9/20 12:55	1.9	339	-16.2	2.1
Natal	6 S/ 35 W	2147 522 2/3	9/20 15:59	1.3	269	-18.5	3.6
Ascension	8 S/ 15 W	2151 3 3	9/21 15:02	0.4	438	-12.3	18.0

Sonde Station	**Sonde location (lat/lon deg.)**	**TES ID run seq, scan**	**TES time (date UTC)**	**Dtime TES-sonde (hr)**	**Ddist (km)**	**Avg. diff sonde-TES in upper troposphere (ppb)**	**Avg. diff sonde-TES in lower troposphere (ppb)**
Ascension	8 S/ 15 W	21993 2	10/11 14:38	0.8	229	-15.3	5.6
Natal	6 S/ 35 W	22223 6	10/20 16:10	1.0	158	-42.2	-1.6
Houston (AVE)	30 N/ 95 W	22623 20	10/31 19:20	1.2	580	0.4	3.9
Houston (AVE)	30 N/ 95 W	22823 16	11/03 19:50	0.1	145	-20.9	11.6
Hohenpei-ssenberg	48 N/ 11 E	2286100 2/3	11/04 12:23	-17.6	232	-18.9	-6.2
Naha	26 N/ 128E	2286816 2/3	11/04 04:47	-0.7	154	-33.1	-0.8
Houston (AVE)	30 N/ 95 W	22903 19	11/05 19:38	0.1	146	-19.4	10.4
Houston (AVE)	30 N/ 95 W	23053 24	11/09 19:14	0.4	720	-49.9	8.3
Huntsville (AVE)	35 N/ 87 W	23054 2	11/09 19:15	-0.3	216	-41.5	8.1
Nairobi	1 S/ 37 E	231090 2/3	11/10 11:33	3.7	563	-32.9	-4.3
Sonde Station	Sonde location (lat/lon deg.)	TES ID run seq, scan	TES time (date UTC)	Δtime TES-sonde (hr)	Δdist (km)	Avg. diff sonde-TES in upper troposphere (ppb)	Avg. diff sonde-TES in lower troposphere (ppb)
Ascension	8 S/ 15 W	2310233 2/3	11/10 14:49	-0.2	101	-16.9	14.9

Sonde Station	**Sonde location (lat/lon deg.)**	**TES ID run seq, scan**	**TES time (date UTC)**	**Dtime TES-sonde (hr)**	**Ddist (km)**	**Avg. diff sonde-TES in upper troposphere (ppb)**	**Avg. diff sonde-TES in lower troposphere (ppb)**
Kago-Shima	32 N/ 131E	2310 336 2/3	11/10 17:10	27.2	291	-14.5	-0.6
Hohenpei-ssenberg	48 N/ 11 E	2310 693 2/3	11/11 01:21	20.4	256	-16.6	3.2
Natal	6 S/ 35 W	2317 305 2/3	11/12 16:16	1.1	378	-19.5	-6.2
Payerne	47 N/ 7 E	2328 172 2/3	11/14 13:01	-22.0	432	7.5	6.4
Tateno	36 N/ 140 E	2336 336 2/3	11/16 16:33	-22. 5	323	-15.8	2.1
Natal	6 S/ 35 W	2336 848 2/3	11/17 04:16	-4.0	520	-17.0	-4.1
Sepang	3 N/ 102 E	2336 955 2/3	11/17 06:44	-3.0	285	-17.4	10.2

Table 3: TES – ozonesonde coincidences for fall 2004.

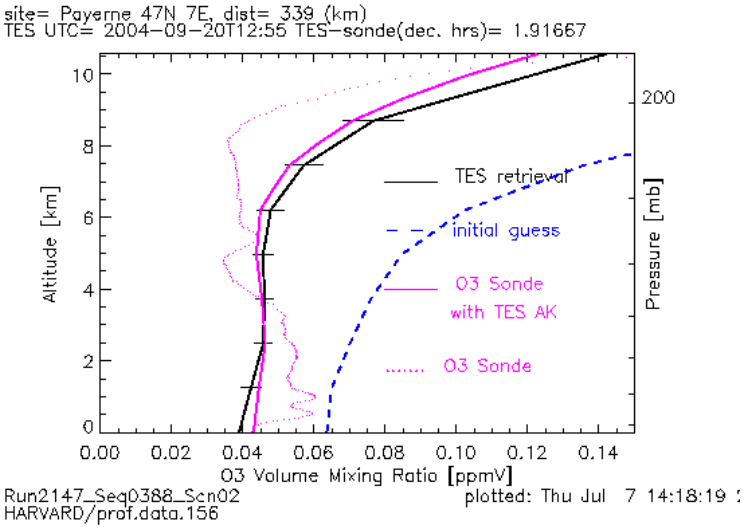

Figure 30: Comparison for Payerne sonde station (47° N).

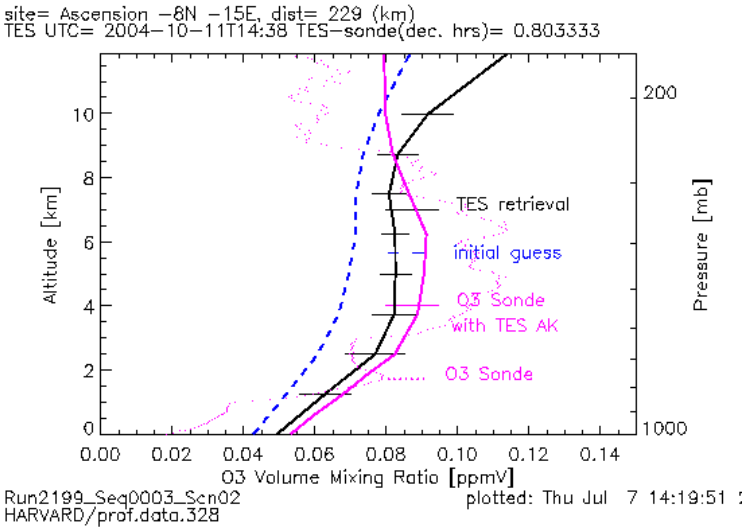

Figure 31: Comparison for Ascension Island sonde station (8° S). Note enhanced O3 in lower troposphere.

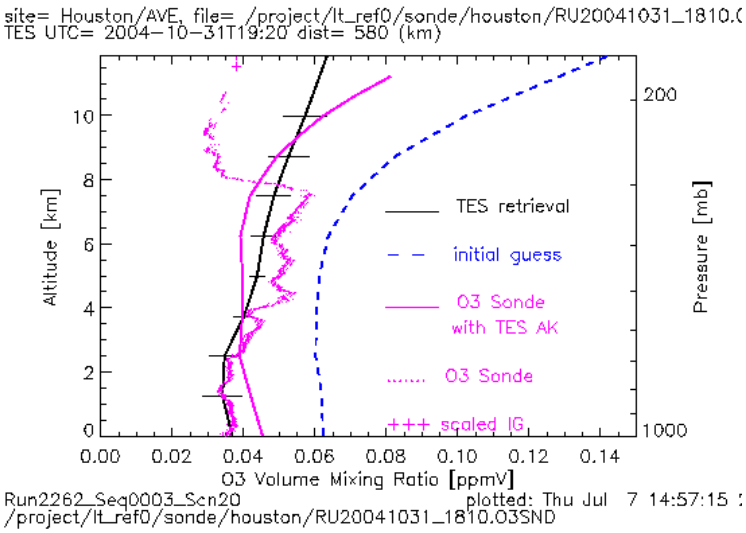

Figure 32: Comparison for sonde launched to coincide with Aura overpass during the Houston AVE campaign in October/November 2004.

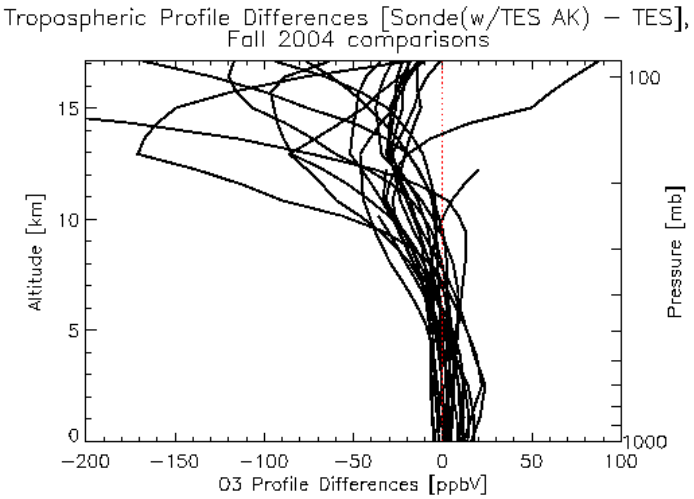

Figure 33: Differences (ppbV) between sonde (after applying TES averaging kernel and constraint) and TES measurements for the sonde launches given in Table 1. Note the consistent bias in the upper troposphere for large O3 values as measured by TES, even after accounting for vertical smoothing and sensitivity. Also note the reasonably good agreement in the lower troposphere.

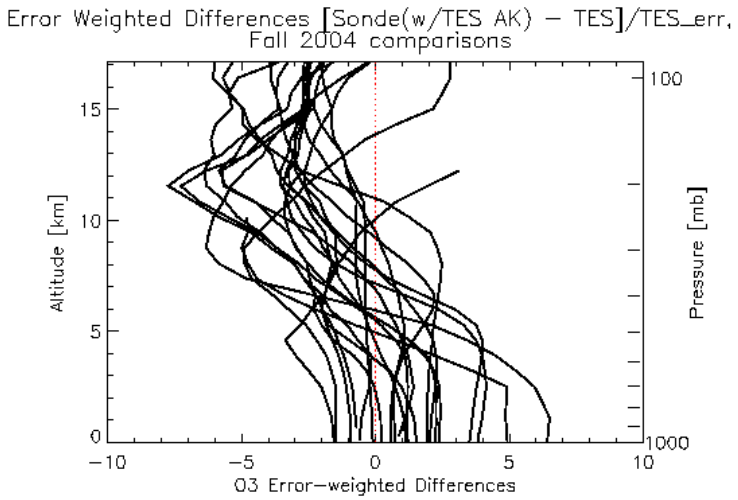

Figure 34: TES error-weighed differences (ns) between sonde (after applying TES averaging kernel and constraint) and TES measurements for the sonde launches listed in Table 3.

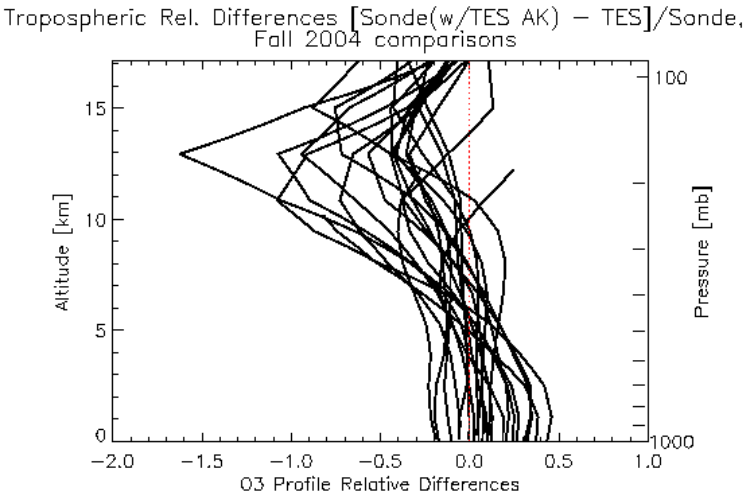

Figure 35: Relative differences (fractional) between sonde (after applying TES averaging kernel and constraint) and TES measurements for the sonde launches listed in Table 3.Figure 29: Example of TES ozone averaging kernel for nadir view in tropics (near Ascension Island).

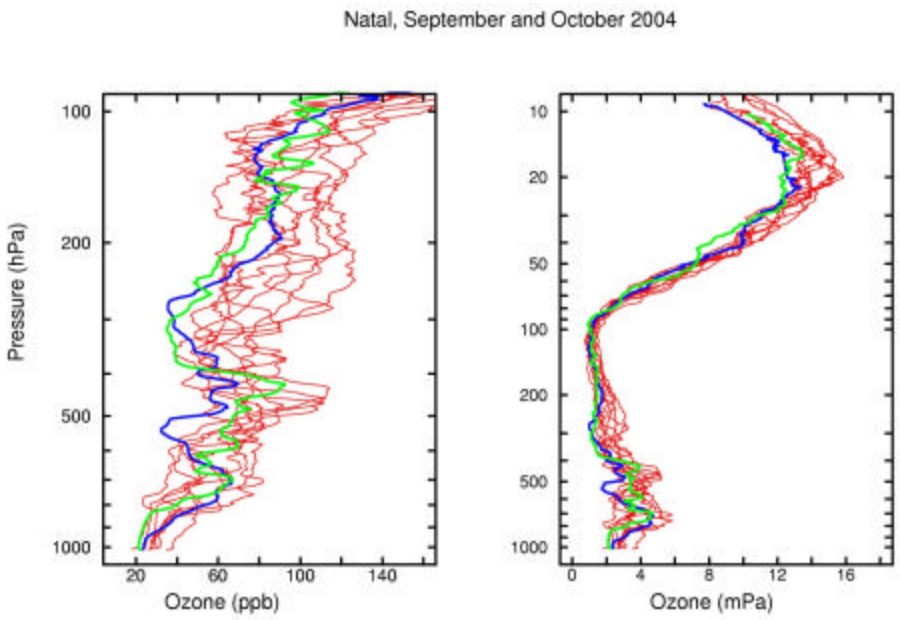

Figure 36: Profiles of ozone in September and October, 2004, at Natal (red). The green (10/20) and blue (9/21) lines show the profiles coincident with TES overpasses.

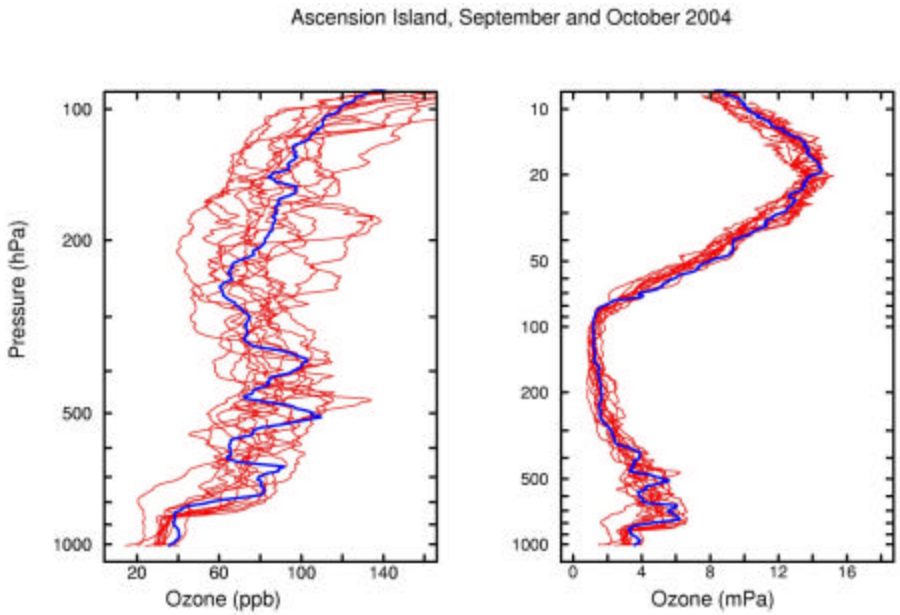

Figure 37: Profiles of ozone in September and October, 2004, at Ascension Island (red). The blue (9/21) line shows the profile coincident with TES overpasses.

5.4 Comparison of TES Tropospheric Ozone Retrievals with the GEOS-Chem Model

5.4.1 Introduction

Retrieved tropospheric ozone profiles from the first TES global survey on 20-21 September 2004 are compared with results from GEOS-Chem Near-Real-Time (NRT) simulations (http://coco.atmos.washington.edu/cgi-bin/ion-p?page=geos_nrt.ion) at the same observation time. NRT simulations employ GEOS-Chem v7.01.02 driven by GEOS-4 first-look assimilated meteorological observations from the NASA Global Modeling and Assimilation Office (GMAO) [*Bey et al., 2001*]. The GEOS-4 dataset has a temporal resolution of 6 hours (3 hours for surface variables and mixing depths), and a horizontal resolution of 1° × 1.25° with 55 layers in the vertical. For computational efficiency, we degrade to 2° latitude × 2.5° longitude horizontal resolution.

Averaging kernels describe the sensitivity of the retrieval to the true state. A sample set of averaging kernels for the TES nadir ozone retrieval in the tropics (11°N, 37°W, sequence number 525) from the global survey on 20-21 September 2004 is shown in the left panel of Figure 38. Each row of the averaging kernel describes the response of the retrieval at a particular pressure level to a perturbation in the true state vector at different pressures [*Rodgers, 2000*]. The black crosses indicate the pressure levels for the corresponding row of averaging kernel. They also show the diagonal terms of the averaging kernel, whose sum measures the number of independent elements of the retrieved state, the degrees of freedom for signal (*dofs*). The *dofs* for ozone retrieval is about 1.7 in the troposphere [*Worden et al., 2004*].

To compare the GEOS-Chem ozone profile with the TES retrieved profile, it is necessary to simulate the retrieval by applying the averaging kernel matrix. Model simulated ozone profiles on the GEOS-Chem eta grid are interpolated to the TES pressure grid, converted to natural logarithms, and then vertically smoothed by TES averaging kernels using the following transformation:

$$\ln \hat{\mathbf{x}}_{\text{model}} = \ln \mathbf{x}_{\mathbf{a}} + \mathbf{A}\left(\ln \mathbf{x}_{\text{model}} - \ln \mathbf{x}_{\mathbf{a}}\right)$$

where $\mathbf{A}$ is the TES averaging kernel matrix and $\mathbf{x}_{\mathbf{a}}$ is the TES initial guess. Since GEOS-Chem has a parameterized stratospheric chemistry, we have replaced the model simulated ozone profiles above the TES-defined tropopause with the TES retrievals.

The right panel of Figure 38 shows the corresponding tropical ozone profiles for that tropical scene including TES initial guess, TES retrieval, GEOS-Chem, and GEOS-Chem with TES averaging kernel applied. GEOS-Chem simulated ozone profile agrees well with TES retrieval up to 500 hPa, where it is within TES error range. The largest discrepancy exists in the upper troposphere, where model simulated ozone values are lower than TES retrieved values by as much as 20 ppbv or even larger. From the plot of averaging kernels, the rows of upper troposphere levels are peaked at about 70 hPa which indicates that the retrievals in the upper troposphere are sensitively influenced by the

lower stratosphere. The large discrepancy in the upper troposphere will be discussed in the following text.

5.4.2 First TES Global Survey of Tropospheric Ozone

Figure 39 displays the tropospheric ozone distributions from the first TES global survey on 20-21 September 2004 at 800, 500 and 300 hPa. We discard retrievals with radiance residual RMS > 1.3 or radiance residual mean > 0.3. GEOS-Chem simulated concentrations are sampled along TES orbit track at the observation time, and processed through the local TES averaging kernels. GEOS-Chem complete daily ozone maps without averaging kernel processing are also included in Figure 39.

The ozone distribution at 800 hPa (Figure 39a) reflects the source regions of ozone precursors. Both TES observations and GEOS-Chem simulations display high values over polluted regions at northern mid-latitudes and in the biomass burning regions of the austral tropics. Ozone structures are broader at 500 hPa and extend to higher latitudes (Figure 39b). High ozone concentrations over East Asia and the South Atlantic are primarily due to convective outflow [*Liu et al., 2002*]. GEOS-Chem predicts a regional maximum over the Middle East in the middle troposphere which *Li et al.* [2001] attributes to a complex interplay of dynamical and chemical factors, and of anthropogenic and natural influences. TES observations reproduce this maximum. At 300 hPa (Figure 39c), ozone distributions show high values poleward 60°, which results from the low tropopause. Both TES and GEOS-Chem display low values in the tropics.

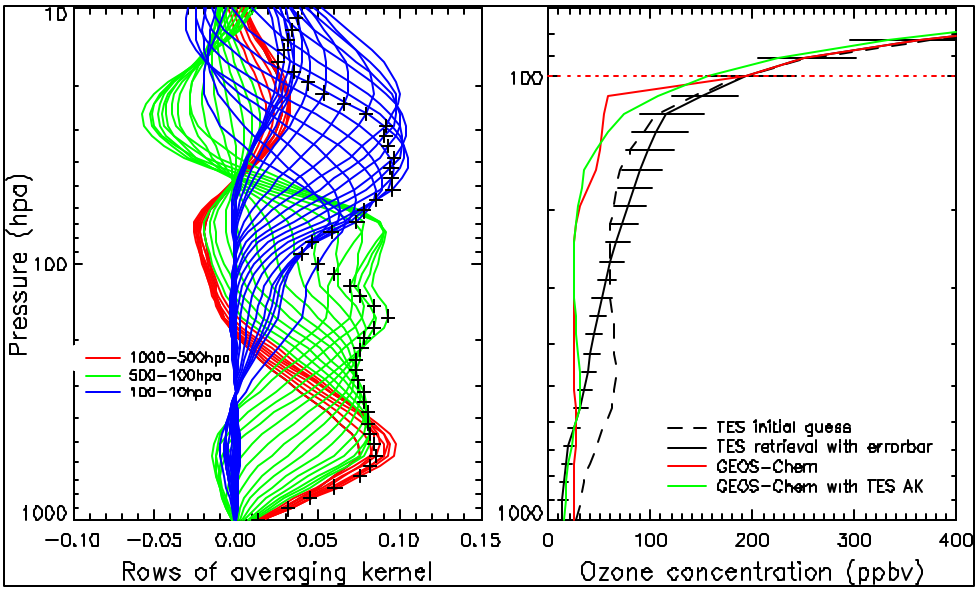

Figure 38: Left panel: Sample averaging kernel matrix for TES nadir retrieval of ozone at 11°N, 37°W (sequence number 525) for pressure levels between 1000 and 100 hPa. The black crosses indicate the pressure levels for the corresponding row of averaging kernel. Right panel: Ozone profiles corresponding to the left panel. The red dashed line indicates the tropopause level.

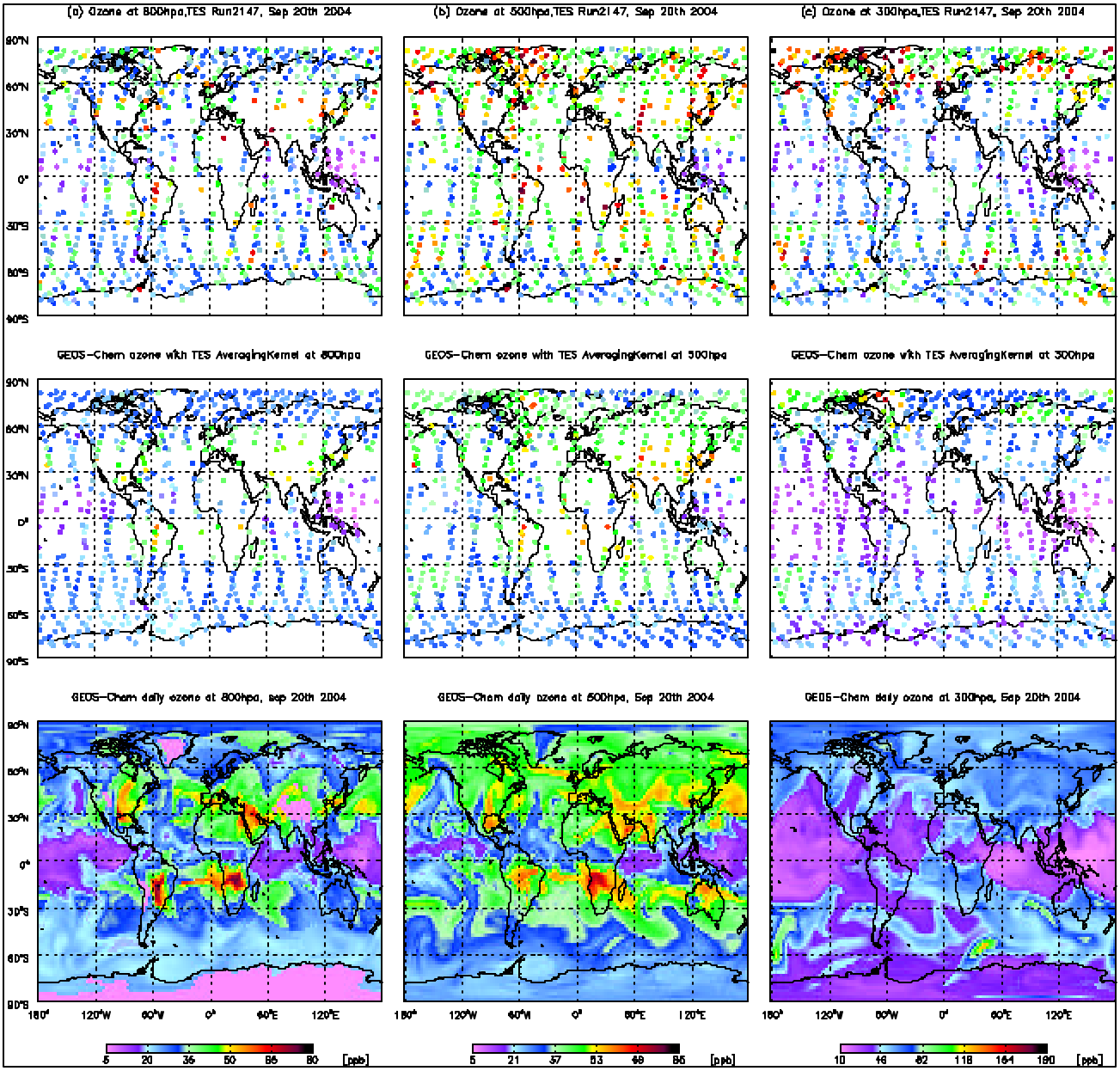

Figure 39: Tropospheric ozone distributions on 20-21 September 2004 at (a) 800, (b) 500 and (c) 300 hPa, respectively. TES nadir observations are about 5° apart along the orbit track and the actual nadir footprint is about 5.3×8.5 km. GEOS-Chem simulations are sampled along TES orbit track at the right observation time and then processed with TES averaging kernels.

5.4.3 Comparisons with GEOS-Chem Model

There are larger TES vs. GEOS-Chem discrepancies at high than at low latitudes. This may be due to several reasons: First, TES radiance shows warm bias at cold radiances

that could affect ozone retrieval at cold temperatures, e.g., near the tropopause or high latitudes (*J. Worden*, TES weekly meeting). Second, the GEOS-Chem ozone evaluation is not well constrained in the upper troposphere at high latitudes where small shifts in tropopause height can introduce considerable variability in ozone concentration [*Bey et al., 2001*]. Also, TES retrievals at high latitudes have less information in the troposphere than low latitudes [*Kulawik et al., 2005*], and a larger contribution from stratosphere may be expected. Here we compare TES ozone observations with GEOS-Chem results at low latitudes (e.g. 40°S to 40°N) for three pressure levels 800 hPa (Figure 40), 500 hPa (Figure 41) and 300 hPa (Figure 42).

At 800 hPa within the 40°S-40°N band, TES ozone observations agree very well with the GEOS-Chem simulation with TES averaging kernels applied (hereafter GC-AK for short). There is a small positive bias of 2.6 ppbv relative to GC-AK, and the slope of the regression line is unity with $R^2 = 0.53$. Figure 41 indicates a larger positive bias of 5.6 ppbv at 500 hPa, with still a large $R^2 = 0.57$ and a regression slope not significantly different from unity. At 300 hPa, TES ozone observations and GC-AK show similar latitudinal distributions with low values in the tropics and high values in the middle latitudes, but TES observations are generally higher than GC-AK (Figure 42). The mean TES vs. GC-AK difference is 18.2 ppbv. This appears to be a systematic bias as the correlation between model and observations is still good ($R^2 = 0.64$) with a slope of unity.

Comparison of TES and GEOS-Chem thus indicates a positive bias of TES relative to GEOS-Chem that is small in the lower troposphere but increases with altitude. Several factors may be responsible. As mentioned before, the warm bias of TES radiances could affect ozone retrieval at the cold temperatures of the upper troposphere. Another factor is that upper tropospheric ozone profiles can be highly influenced by the lower stratospheric ozone from the analysis of ozone averaging kernels [*Bowman et al., 2005*]. Also, the NRT simulations presented here have a much smaller global lighting NO_x source of about 2.5 Tg N yr^{-1} compared with that in the TOMS TTOCs study of *Martin et al.*, [2002] which has 6 Tg N yr^{-1} and produces a simulation consistent with TOMS and *in situ* observations. The new NRT simulations (using GEOS-Chem v7.02.04) have a lighting NO_x source of 4.72 Tg N yr^{-1} and roughly increase the ozone levels in the upper troposphere by 3-7 ppbv. However, it is not sufficient to solve the TES vs. GEOS-Chem discrepancies. More analysis including *in situ* observations is needed.

5.4.4 TES vs. GEOS-Chem Discrepancy and Cloud Optical Depth

Clouds are ubiquitous in the atmosphere and have a large effect on the observed infrared radiation field. The TES science team has developed an algorithm to model clouds as a frequency-dependent effective optical depth localized at a single pressure level for the TES nadir retrievals [*Bowman et al., 2005*]. And the retrievals in the presence of clouds need extensive validation.

We examine the ozone retrievals over cloudy scenes by analyzing whether the existence of clouds affect TES vs. GEOS-Chem discrepancies. Figure 43 shows the correlation between the TES retrieved cloud optical depth and the differences of tropospheric column

ozone (TES minus GC-AK) within the 40°S-40°N band. Tropospheric ozone column values are calculated by integrating the vertical profiles of TES or GEOS-Chem with averaging kernels applied to the TES-defined tropopause. The plotted points in the figure are fairly scattered, indicating a poor relationship between these two. The regression line even have a negative slope with a small $R^2 = 0.007$. It appears that TES vs. GEOS-Chem ozone discrepancies are uncorrelated with the TES retrieved cloud optical depth, and TES ozone retrievals over cloudy scenes do not have significant additional error.

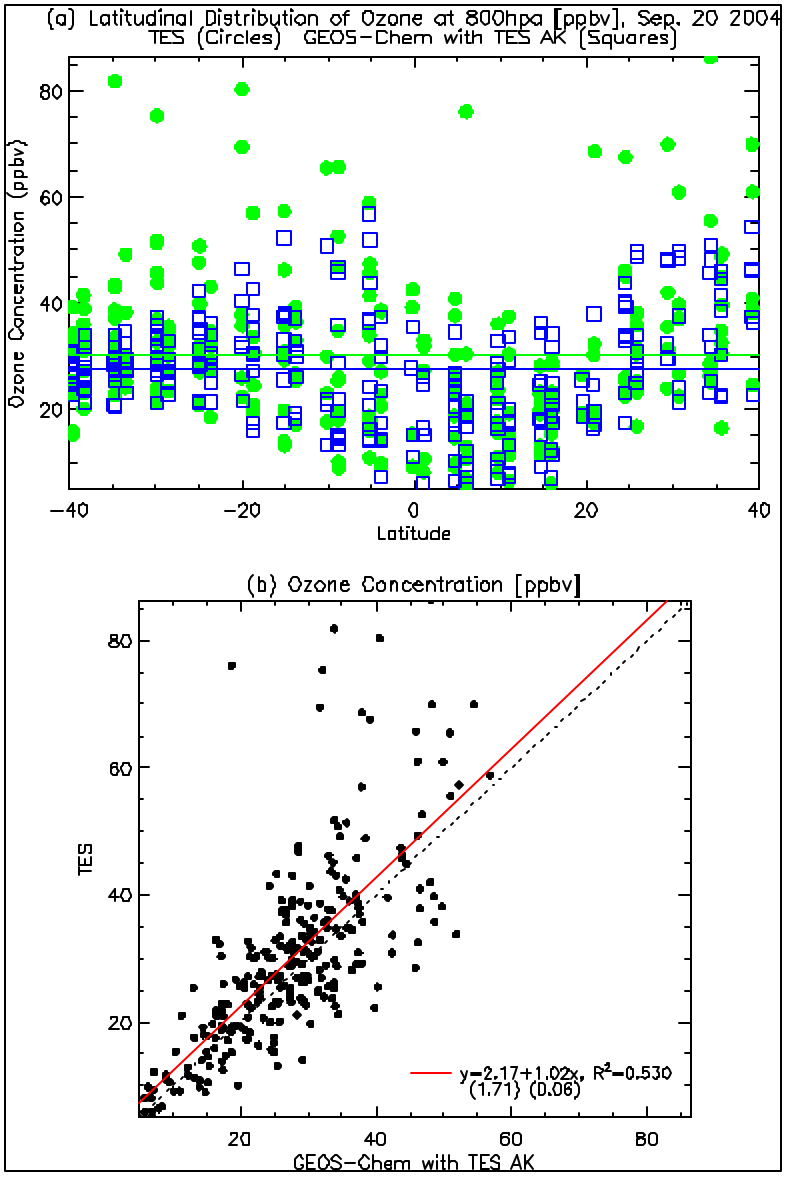

Figure 40: (a) Latitudinal distribution of ozone at 800hpa in the 40°S-40°N band for TES observations and GEOS-Chem simulations. The straight lines indicate the mean ozone concentration. (b) Correlation between TES ozone observations and GEOS-Chem simulations at 800hpa. The red line shows the linear regression. The slope and R^2 are indicated and the values in the parentheses are error estimates of the fitted parameters.

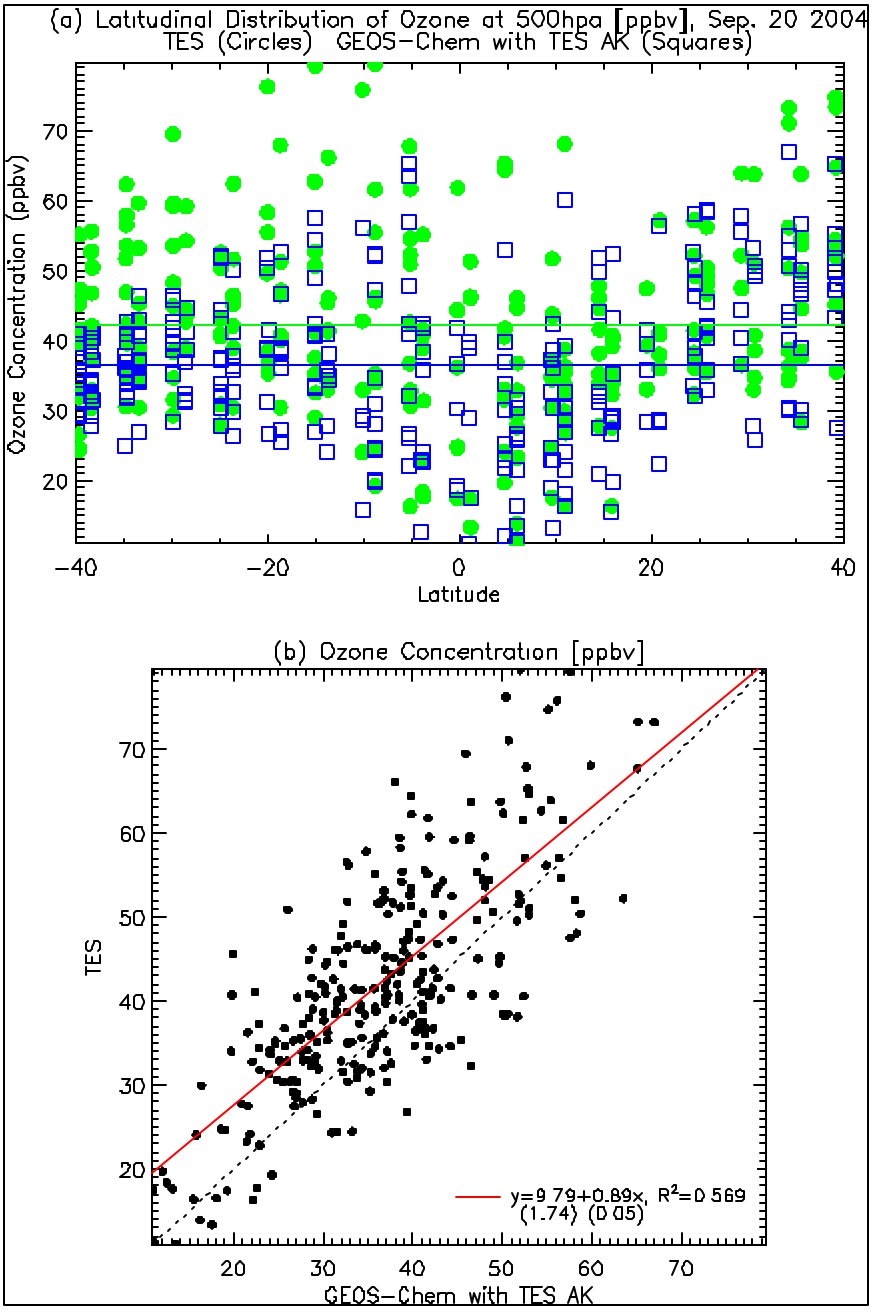

Figure 41: The same as Figure 3, but at 500hpa.

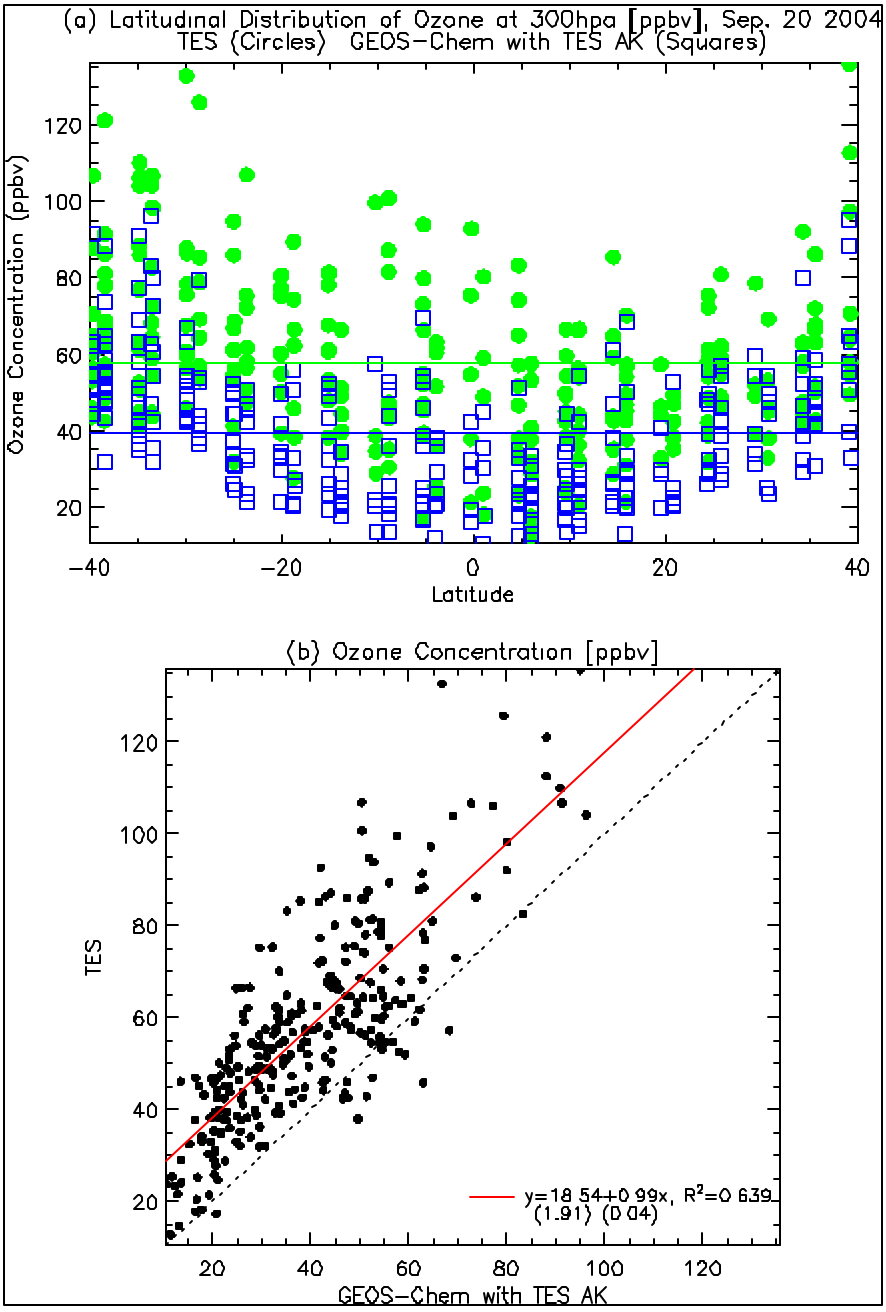

Figure 42: The same as Figure 3, but at 300hpa.

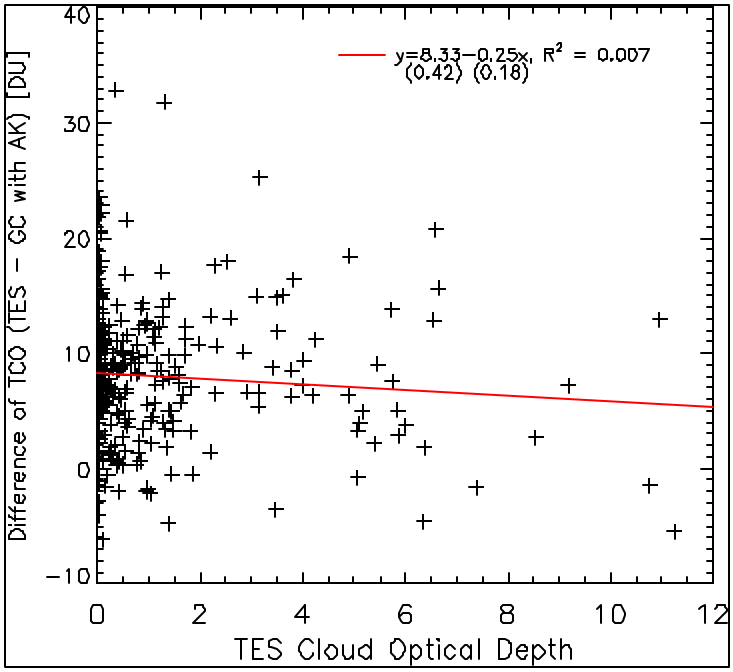

Figure 43: Correlation between the difference of tropospheric column ozone (TCO) (TES minus GC-AK) and the TES retrieved cloud optical depth. The red line shows the linear regression. The slope and R^2 are indicated and the values in the parentheses are error estimates of the fitted parameters.

5.4.5 Latitudinal Structure of Ozone

TES and GEOS-Chem data show the same broad latitudinal structure in ozone at all altitudes. The latitudinal variability in TES ozone is strongly related to the *a priori* variability. In the lower troposphere (below 500 mb) TES exhibits a predominantly negative bias compared to GEOS-Chem of less than 5%. This bias also has a latitudinal dependence with the Southern Hemisphere showing closer correspondence between the two datasets. In the mid troposphere at 500 mb the bias between TES and GEOS-Chem is negative in the Southern Hemisphere and switches sign in the Northern Hemisphere to give an overall mean positive bias of just 2.7%. Upper tropospheric TES ozone observations show a considerable positive bias of up to 200% at some latitudes, with larger biases observed in the southern tropics and the Northern Hemisphere.

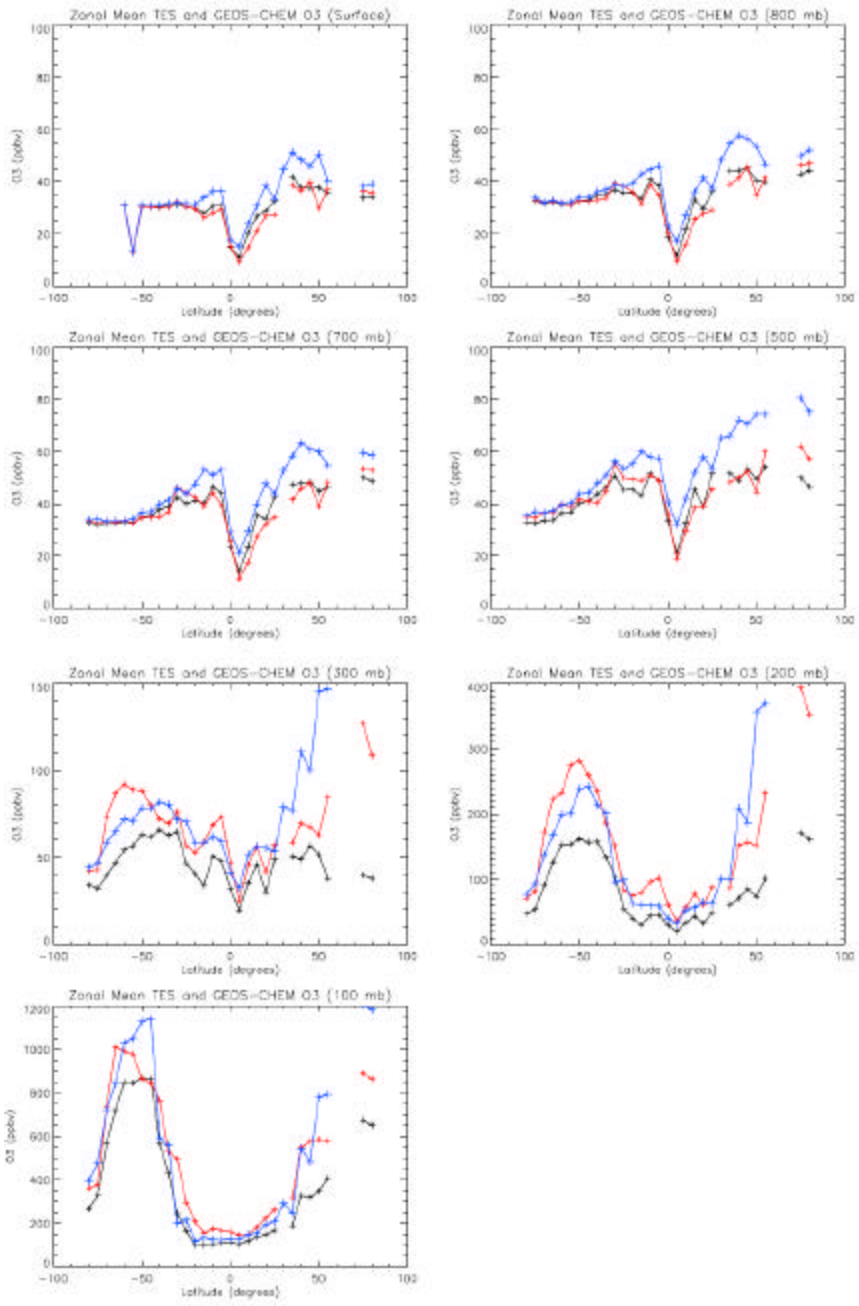

Figure 44: TES (Red), GEOS-Chem (black) and TES a priori (blue) zonal mean O3 profiles for TES Run ID 2147 (September 20/21 2004). Both TES and the transformed GEOS-Chem profiles are averaged over all longitudes into 5 degree latitude bins to obtain zonal mean profiles for comparison.

5.4.6 Comparison for TES Step & Stare Special Observations Over the Tropical Atlantic

Both TES and GEOS-Chem show enhanced ozone concentrations in the middle and upper troposphere over tropical South Atlantic, related to convective outflow of southern Africa and South America biomass burning, and lower values in the lower and upper troposphere around the ITCZ (Figure 45). Largest discrepancies in ozone concentrations are seen in the upper troposphere (Figure 46), where the differences are 2-3 times the retrieval errors. This is in agreement with the comparison between TES and ozonesondes in the tropics which indicates that TES ozone retrievals in the upper troposphere are biased high. Tropospheric ozone columns calculated from TES and GEOS-Chem show similar latitudinal variation with enhanced values over the tropical South Atlantic and low values around the ITCZ (not shown here). Partial tropospheric ozone columns calculated from TES and GEOS-Chem are highly correlated (Figure 47). Again, the largest difference is seen in the partial ozone columns between 500 hPa and the tropopause.

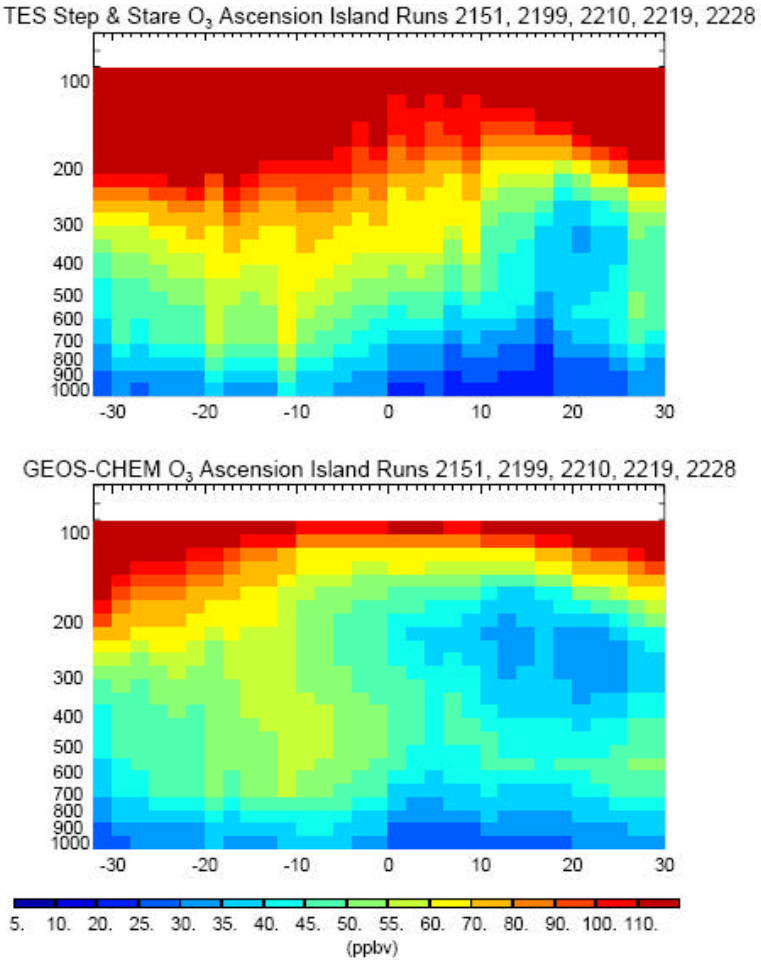

Figure 45: TES ozone retrievals and GEOS-Chem simulated ozone concentrations averaged over the five step & stare special observations at Ascension Island between 09/21/04 and 10/21/04.

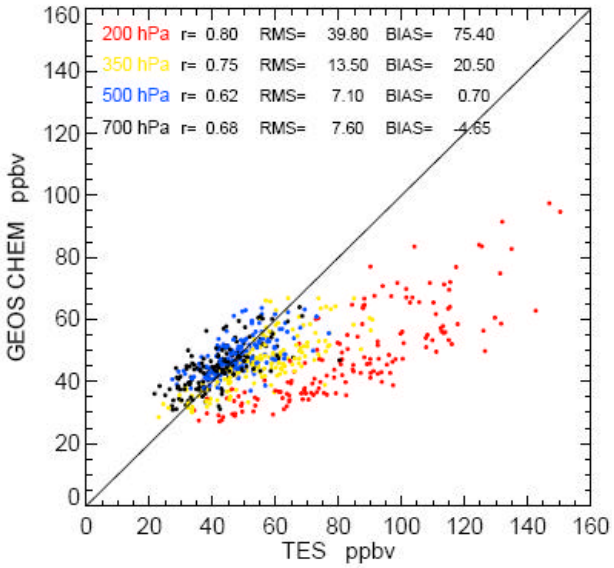

Figure 46: Correlation between TES ozone retrievals and GEOS-Chem values for the same step & stares as Figure 45 at 200, 350, 500, and 700hPa. Bias is defined as (TES GEOS-Chem)/TES.

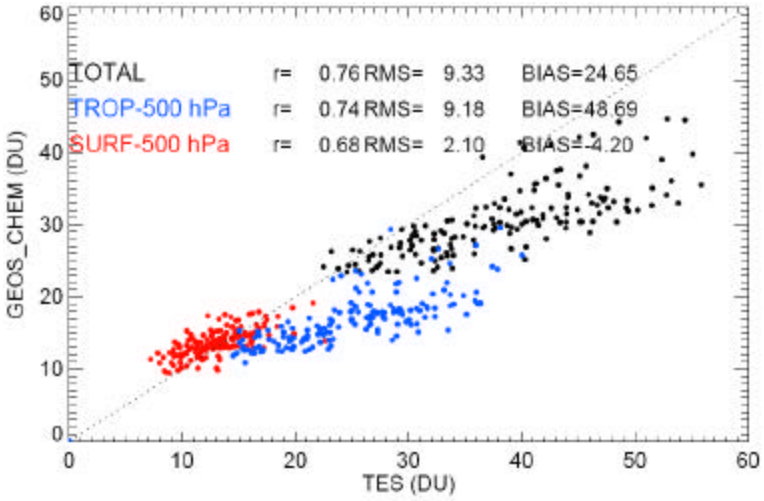

Figure 47: Correlations between TES and GEOS-Chem calculated partial tropospheric ozone columns.

6 Validation of TES Water Vapor

6.1 Validation of TES Column Water Vapor

Total column water vapor as retrieved from TES was compared with the total water vapor column from AIRS and AMSR-E. The AIRS/AMSU suite (Atmospheric Infrared Sounder and Advanced Microwave Sounding Unit) is on the EOS-Aqua satellite, which flies on the same orbit track as TES, approximately 15 minutes ahead. AIRS provides vertical profiles of water vapor and temperature on 45km circular footprints. The AIRS data shown is v4 unless otherwise noted. The AIRS products have been validated against dedicated radiosondes and aircraft measurements (AIRS validation report, Gettelman et al, 2004). AMSR-E (Advanced Microwave Scanning Radiometer-EOS) is a passive microwave radiometer, and among other products, column water vapor is retrieved and L3 data is reported on a 0.25 by 0.25 latitude and longitude grid. Thus, the data that are compared here are matched in space, and have a 15 minute difference in time.

Figure 48 is a plot of the total water vapor from TES for Run ID 2286. This shows the latitudinal variation that is typical for total water vapor. The following set of four figures (Figure 49, Figure 50, Figure 51 and Figure 52) show comparisons of total water vapor column, and differences in mm of precipitable water (TES-AIRS). The second set of four plots (Figure 53, Figure 54, Figure 55 and Figure 56) shows absolute differences of TES-AMSR for the same set of global surveys. The third set of plots (Figure 57, Figure 58, Figure 59 and Figure 60) show comparisons between TES and AMSR for the same global surveys, but the differences are plotted in percent difference (TES-AMSR)/TES.

The data usage recommendations for AIRS and AMSR-E are similar, only over ocean, and in a restricted latitude range. The data quality flags of AIRS (retrieval type less than or equal to 10) and AMSR were used in the data selection. TES data were used if they met three criteria: Radiance residual rms less than or equal to 1.4, radiance residual mean less than 0.05, and average effective cloud optical depth less than 0.8.

The differences of TES-AIRS and TES-AMSR-E have very similar characteristics. TES is about 12% drier than AIRS and AMSR-E, with little latitudinal dependence in the percentage difference. These statistics are based on about 300 matches per global survey. Ninety percent of the differences are in the range of -40% to 10%. Each global survey has a small number of points with differences greater than +/- 70%.

It should be noted that AMSR-E is a microwave instrument, so the method of measuring the total water vapor column is completely different than the methods used by TES. The data reported by AIRS comes from a multi-step retrieval that includes a regression step and a physical retrieval and data from both a microwave and infrared instrument. Recent analysis suggests that the total water vapor column reported by AIRS is strongly influenced by the AMSU microwave measurement (Barnet, personal communication).

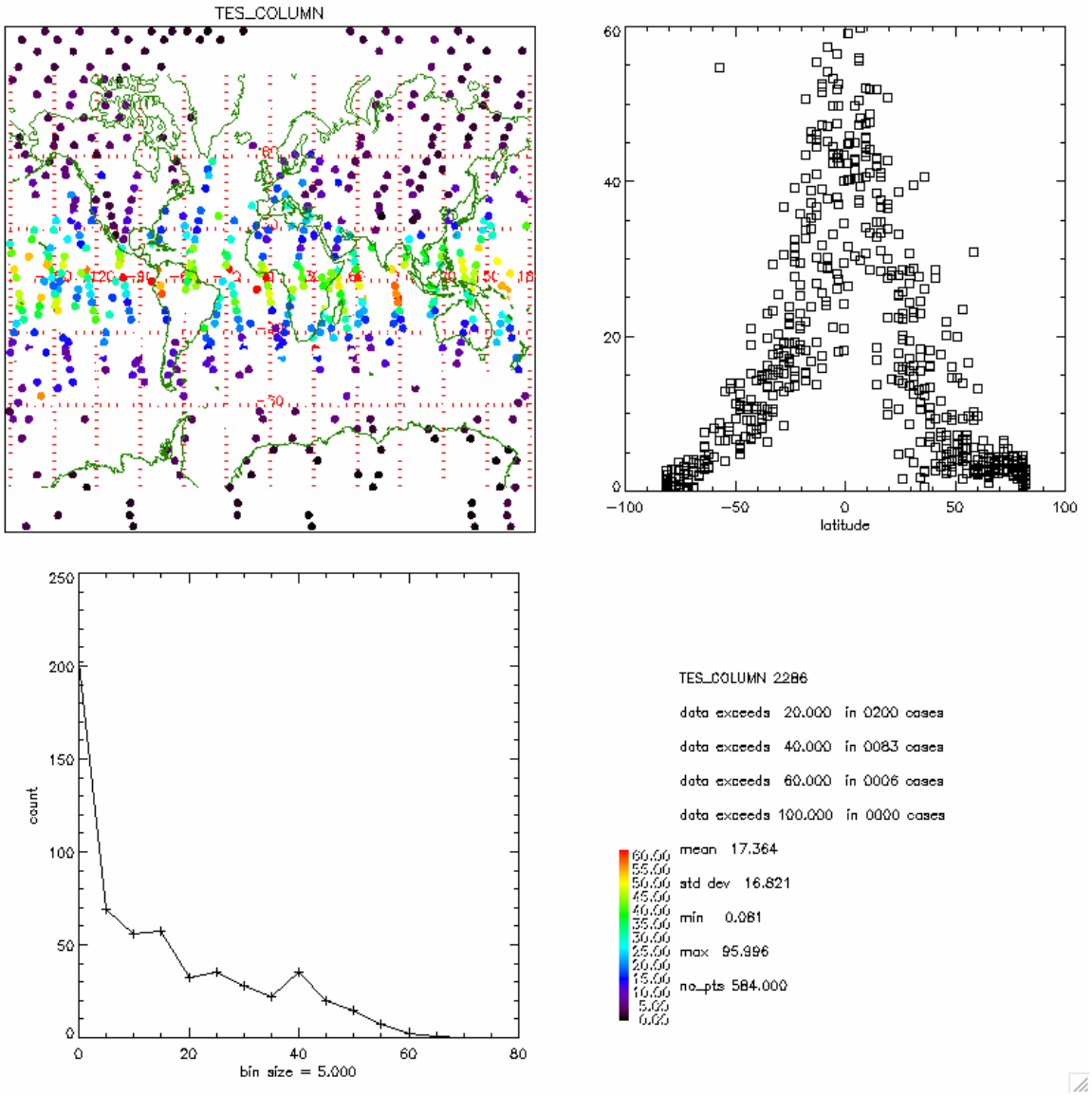

Figure 48: Total water vapor column as retrieved by TES for Run ID 2286. The column is reported in mm of precipitable water.

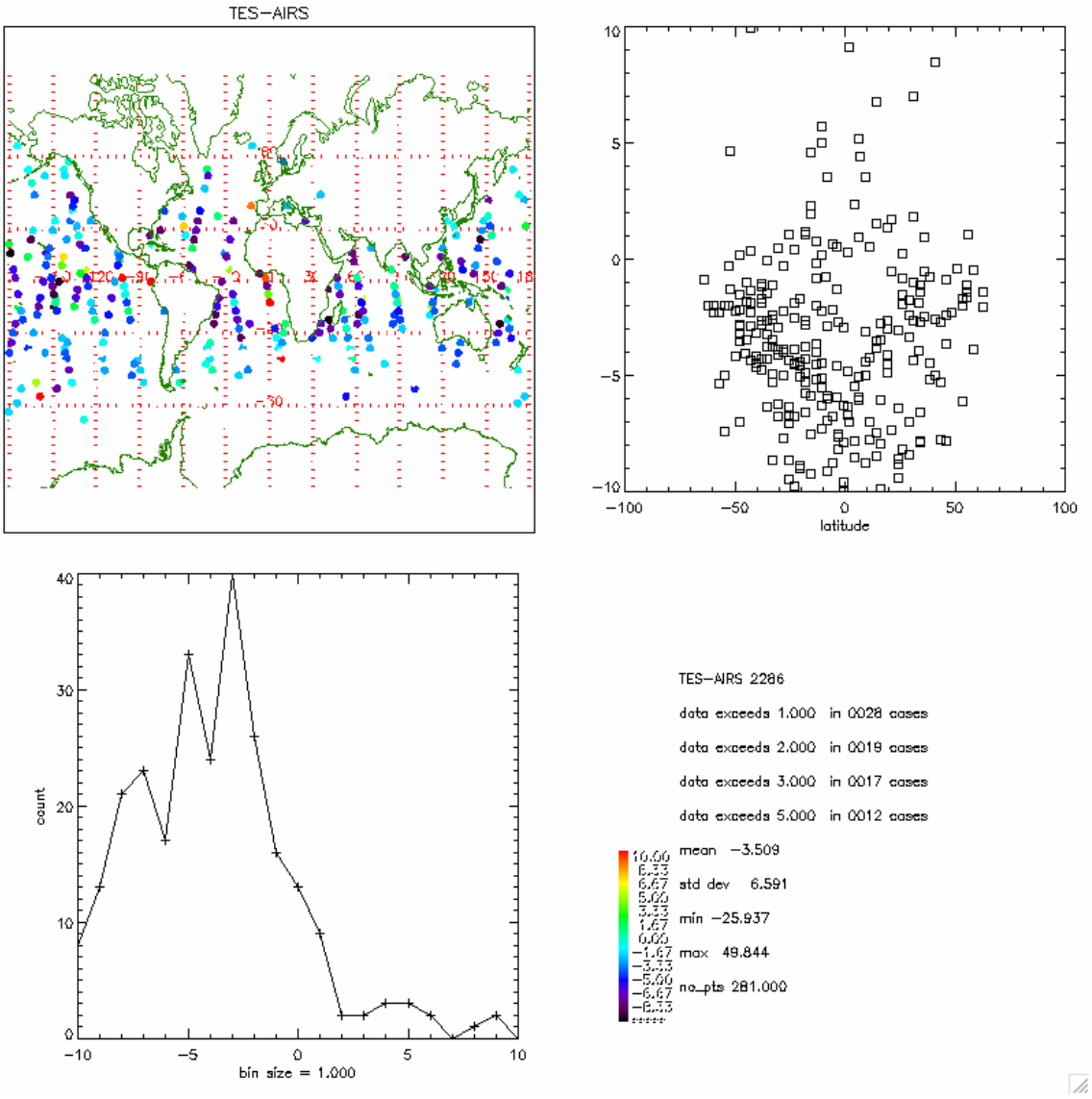

Figure 49: Comparisons of TES and AIRS total column water for Run ID 2286. The upper left panel is a map of the differences in mm of precipitable water (TES – AIRS). The upper right hand panel is a plot of the absolute differences (in mm precipitable water) as a function of latitude; the lower left is a histogram of the difference. Some statistics about the differences are shown in the lower right of the figures.

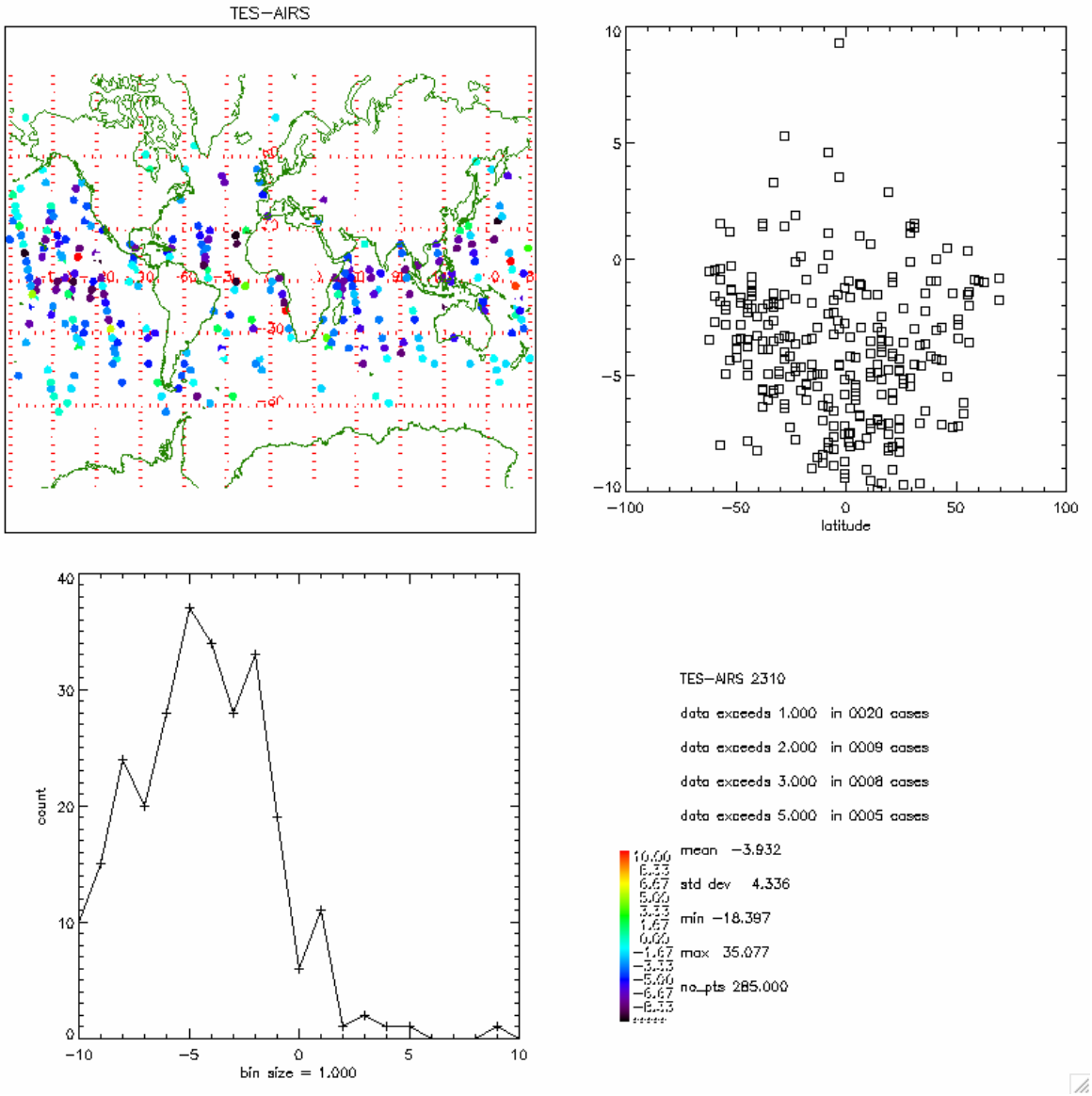

Figure 50: Comparisons of TES and AIRS total column water for Run ID 2310.

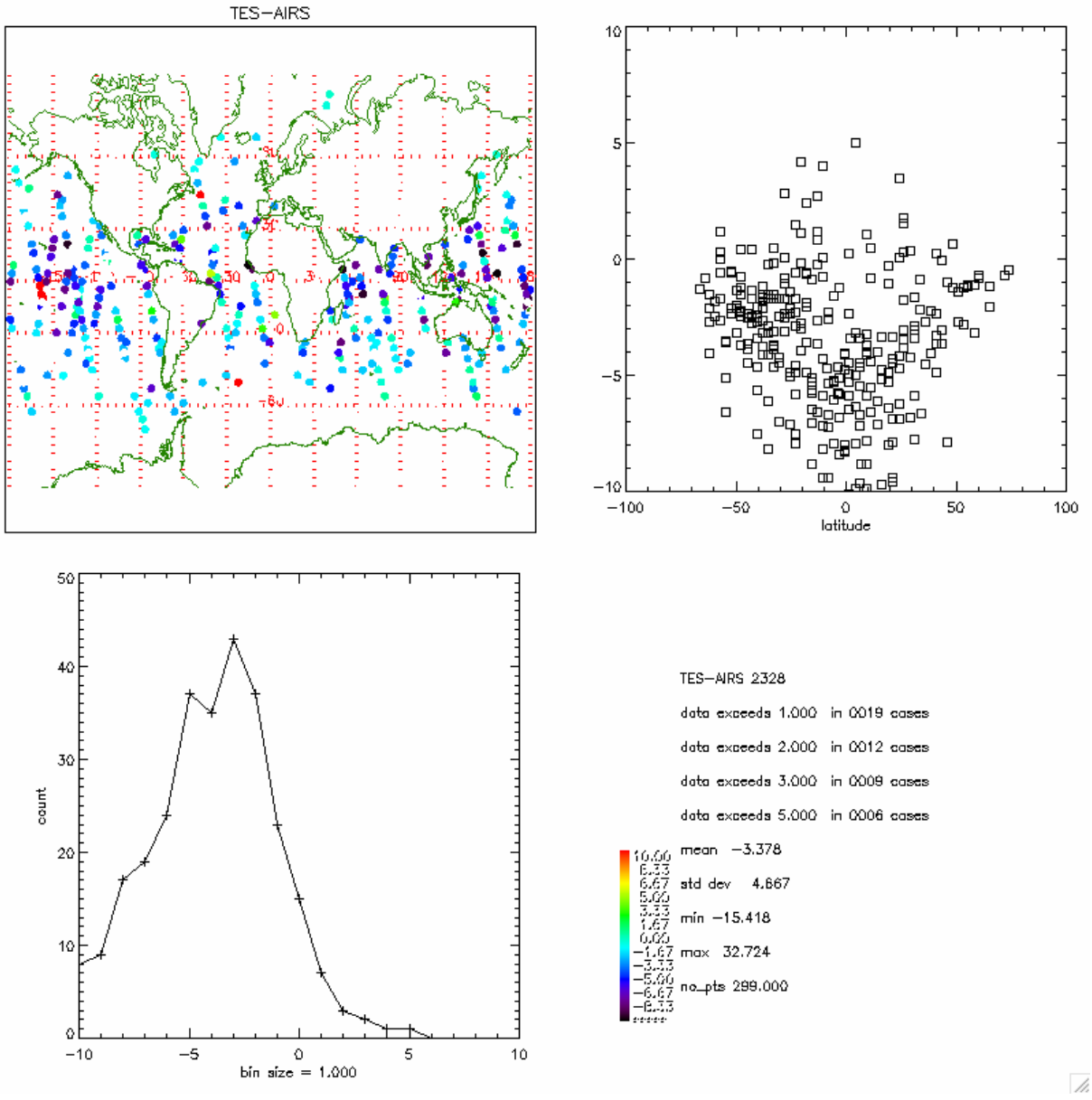

Figure 51: Comparison of TES and AIRS total column water for Run ID 2328.

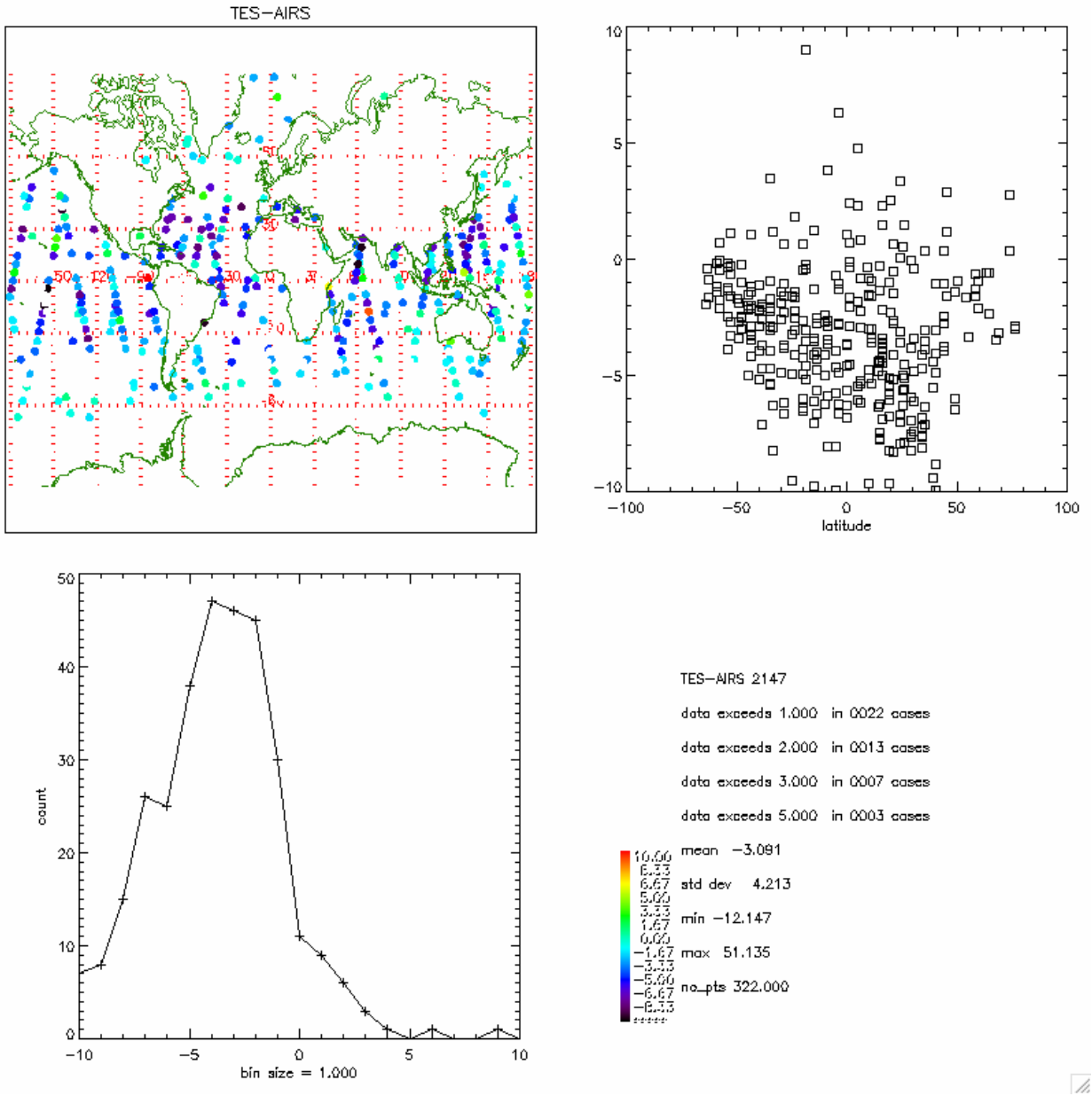

Figure 52: Comparison of TES and AIRS total column water for Run ID 2147. AIRS v3 data is used on this comparison.

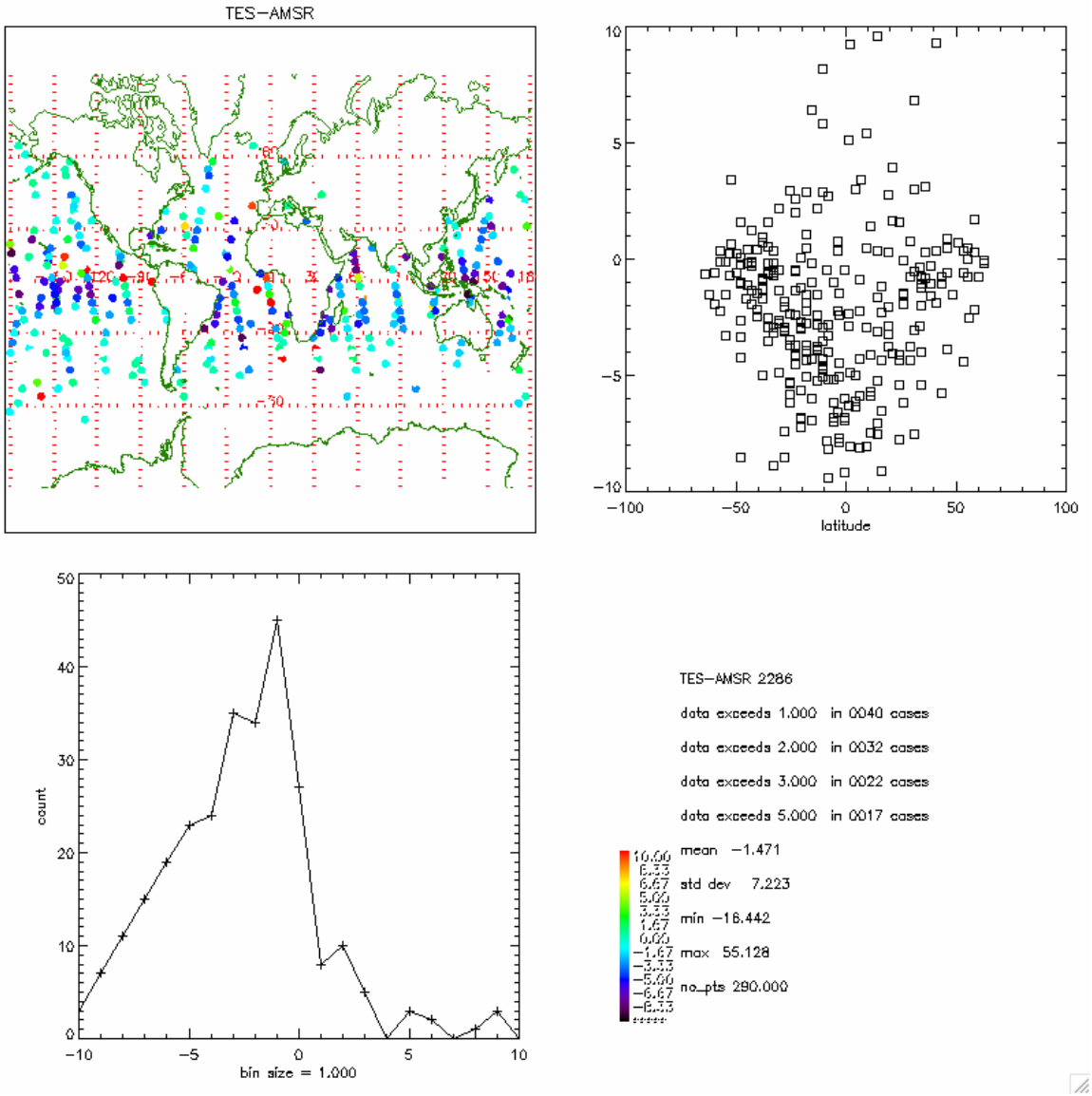

Figure 53: Differences of total water vapor column (TES-AMSR) in mm of precipitable water for Run ID 2286. Plot is laid out as described in caption of Figure 48.

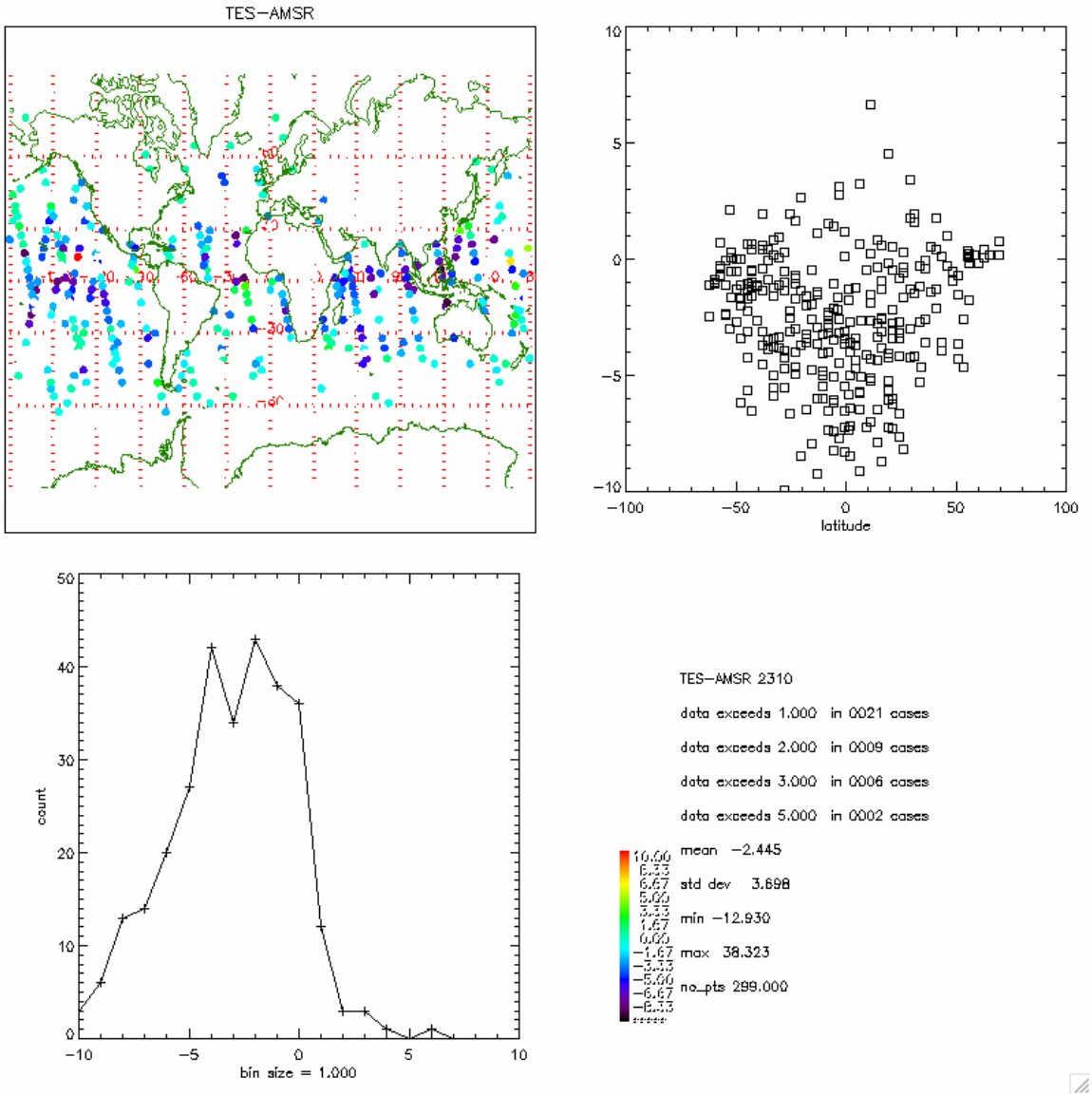

Figure 54: Differences of total water vapor column (TES-AMSR) in mm of precipitable water for Run ID 2310.

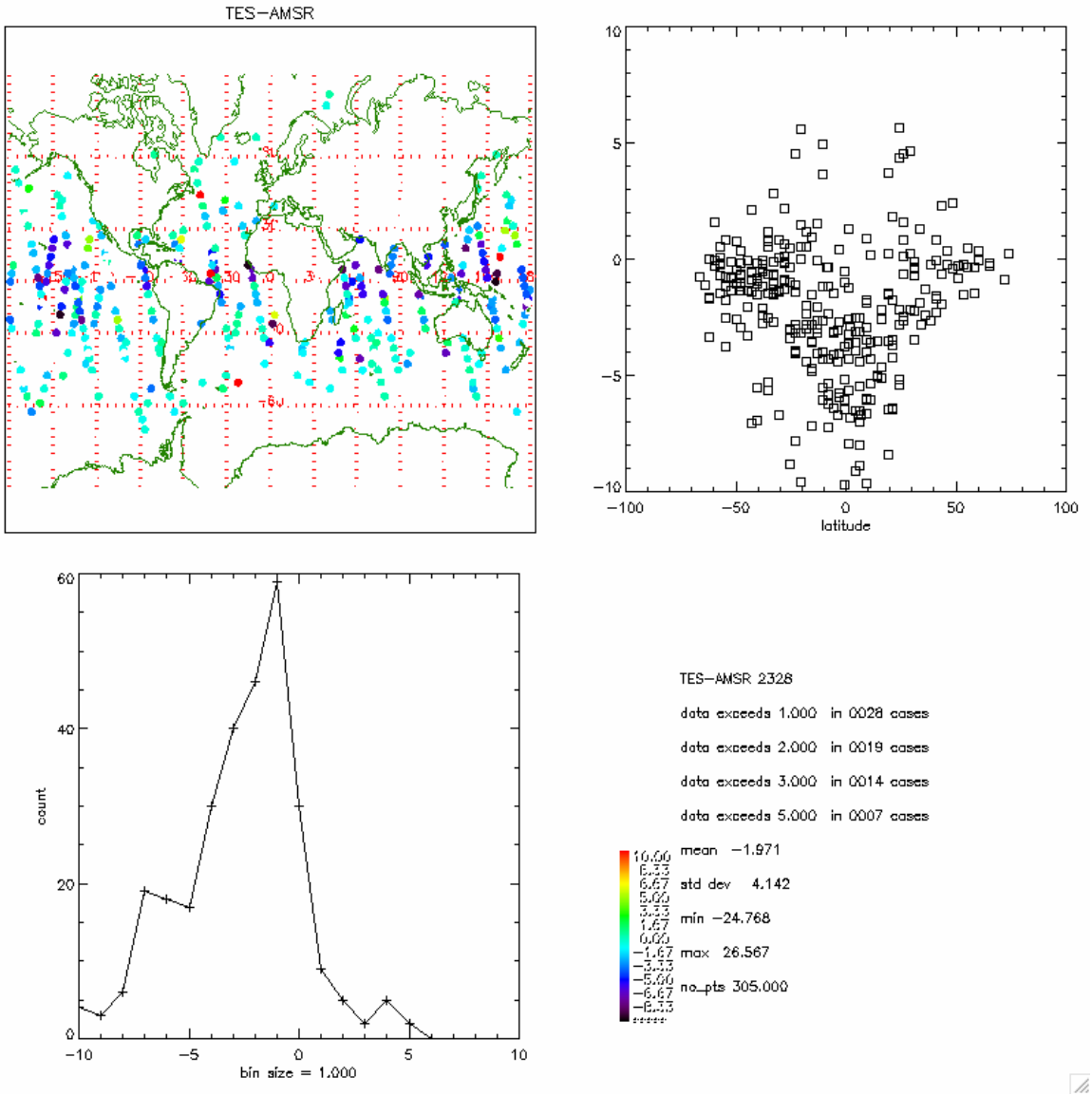

Figure 55: Differences of total water vapor column (TES-AMSR) in mm of precipitable water for Run ID 2328.

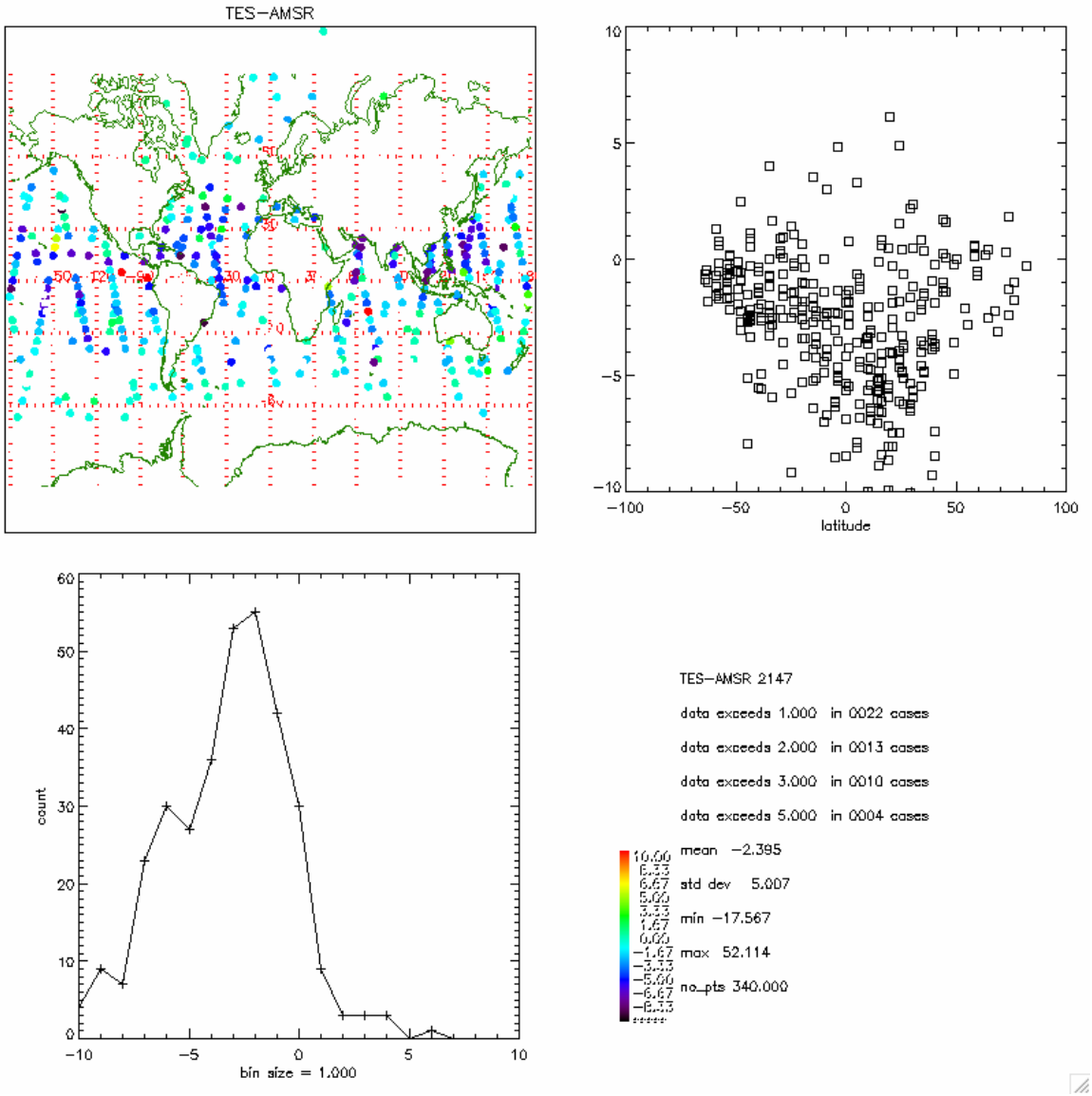

Figure 56: Differences of total water vapor column (TES-AMSR) in mm of precipitable water for Run ID 2147.

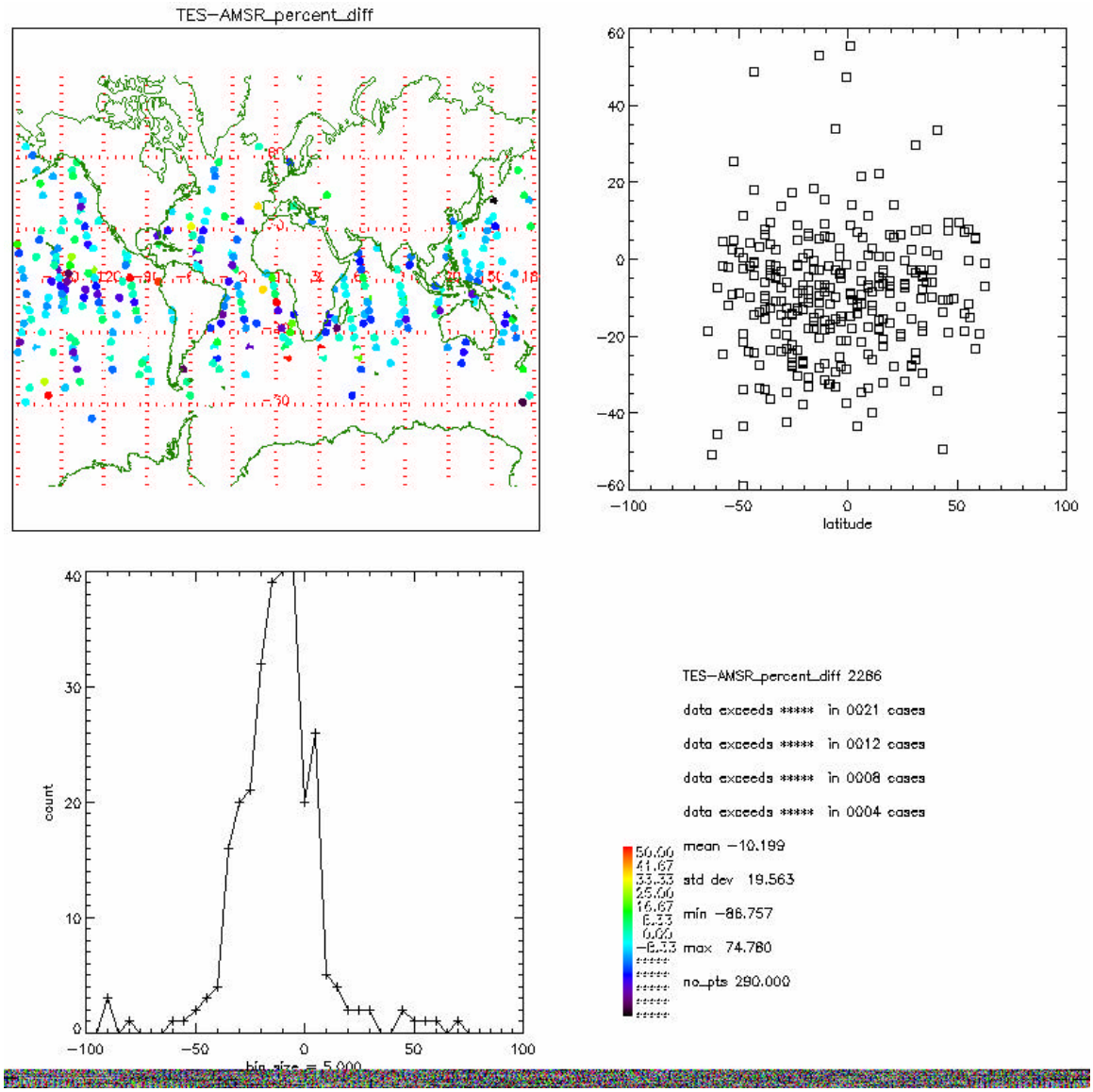

Figure 57: Percent differences of total water vapor column ((TES-AMSR)/TES) in for Run ID 2286. More details of plot layout as described in caption of Figure 48.

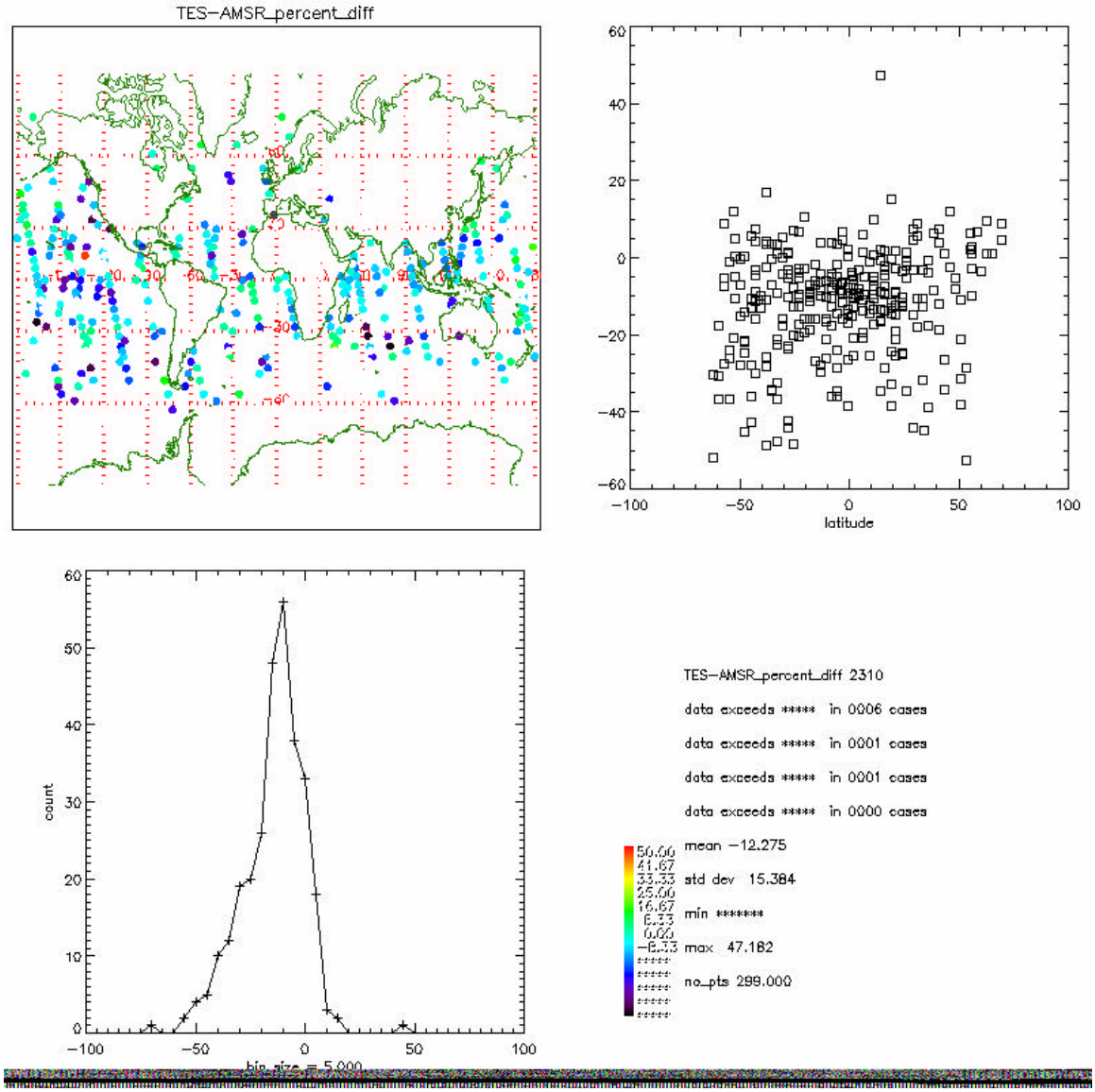

Figure 58: Percent differences of total water vapor column ((TES-AMSR)/TES) in for Run ID 2310.

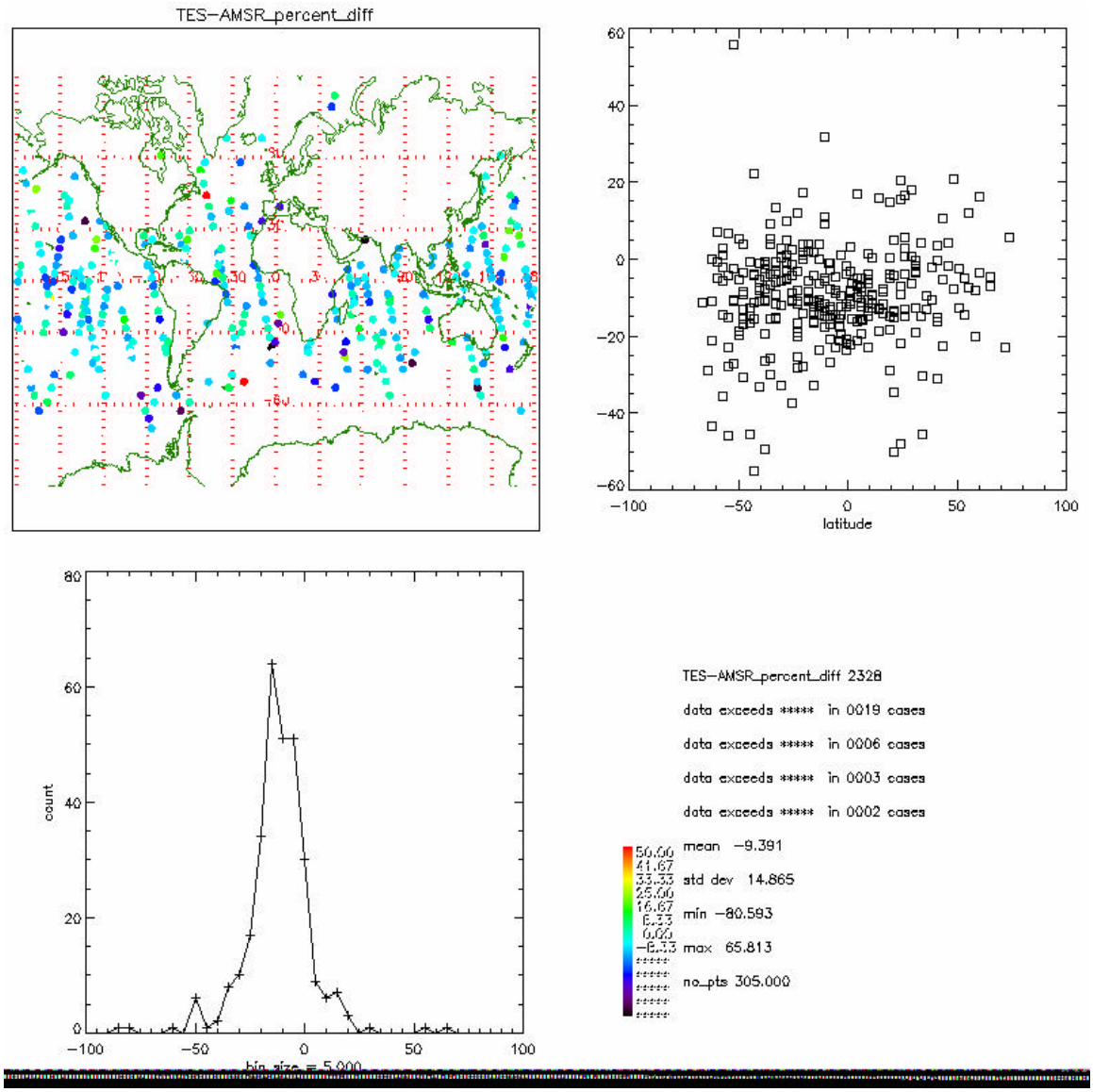

Figure 59: Percent differences of total water vapor column ((TES-AMSR)/TES) in for Run ID 2328.

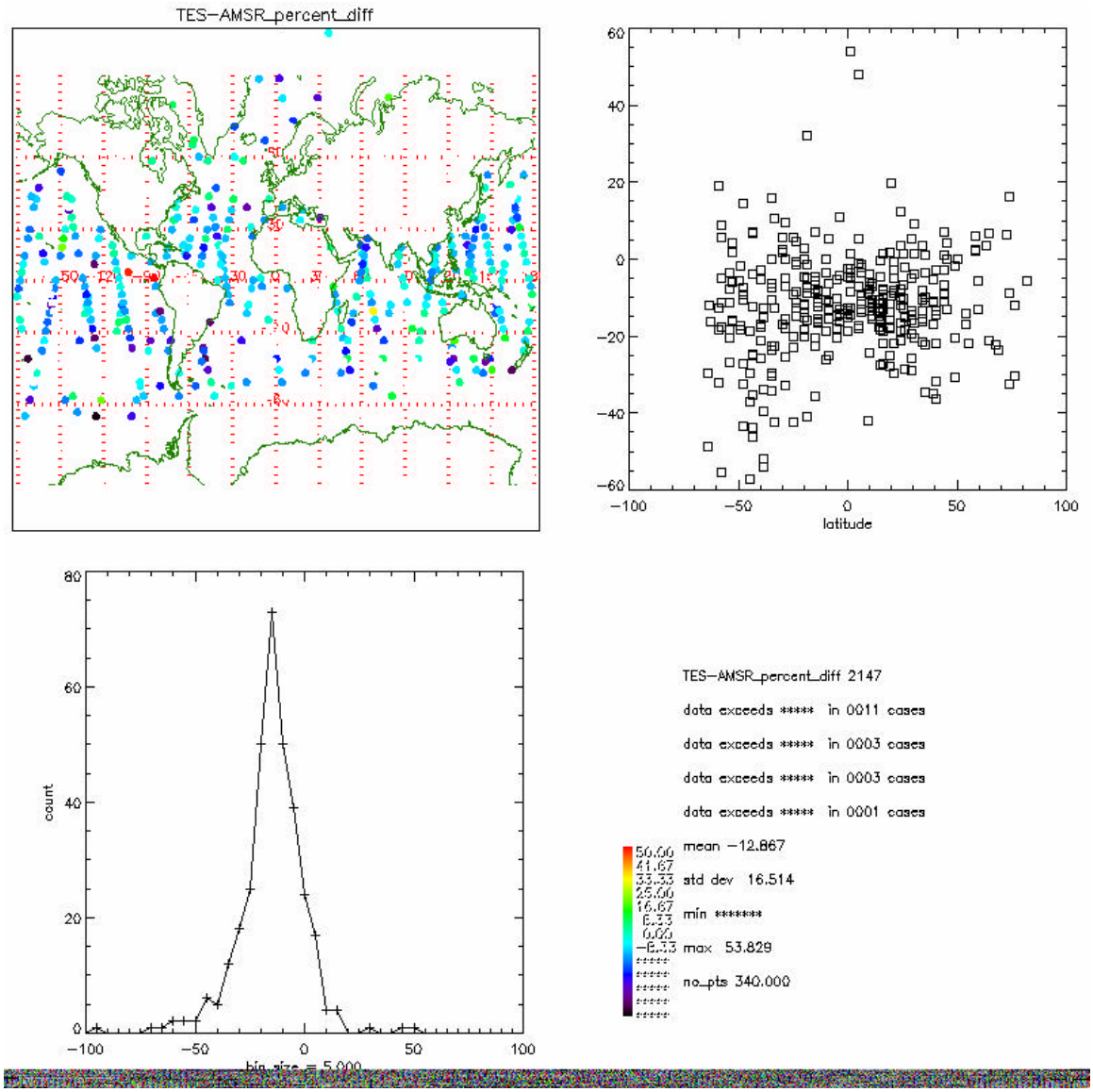

Figure 60: Percent differences of total water vapor column ((TES-AMSR)/TES) in for Run ID 2147.

6.2 TES Water Vapor Profile Comparisons with AIRS

In this section will show comparisons of AIRS and TES vertical profiles of water vapor. Statistics are shown for the bias and rms differences aggregated over global surveys and sets of step and stare measurements.

The AIRS products are reported on 28 layers, so for this comparison, the TES products were integrated to matching vertical layers. The bias, standard deviation of the difference,

rms of differences, standard deviation of the AIRS data, and standard deviation of the TES data are reported.

Figure 61 and Figure 62 have two panels each. The left panel shows the mean profile for TES and AIRS, and the right panel shows the bias and standard deviations. Note that there is an inconsistency in the way that the statistics are presented in Figure 61 and Figure 62, since the bias is shown as (AIRS-TES)/TES For all of the Run IDs examined, the vertical structure was similar. The largest absolute differences in the vertical profiles occur in the layers between 700 and 900 mb. This accounts for most of the bias in the total water vapor column between AIRS and TES. There are also large percentage differences in the 150 to 300 mb region, where the rms differences also become large. The number of data points used in the comparison is shown on the right hand side of the left-hand panel. There are fewer data points in the profile comparison than in the total water vapor column because the AIRS data quality flagging for profile data is stricter than for the total column.

Figure 63, Figure 64 and Figure 65 are scatter plots of the AIRS and TES data at each pressure level, along with histograms of the differences for Run ID 2310. In the layers where there is a larger bias, the differences have a clearly non-Gaussian distribution. Other runs have similar characteristics, and are not shown here.

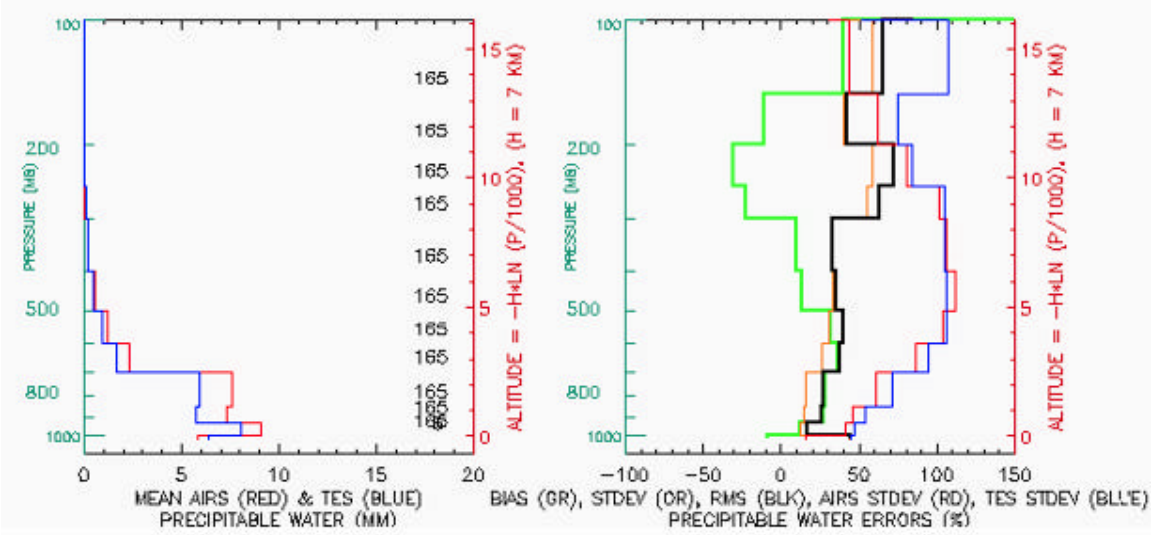

Figure 61: The mean water vapor profile (left panel) and bias and standard deviations (right hand panel) for Run ID 2310.

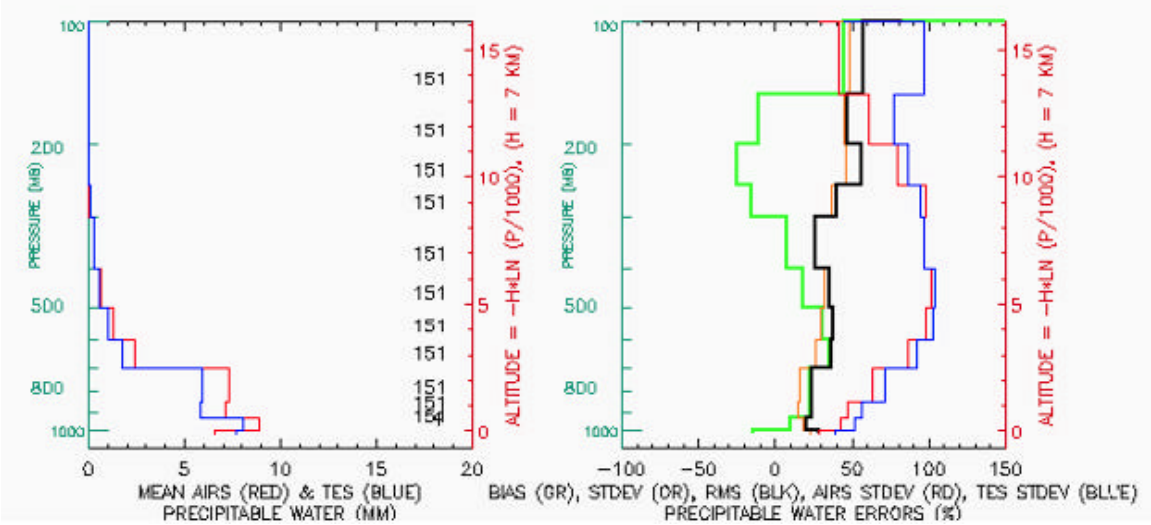

Figure 62: The mean water vapor profile (left panel) and bias and standard deviations (right hand panel) for Run ID 2328.

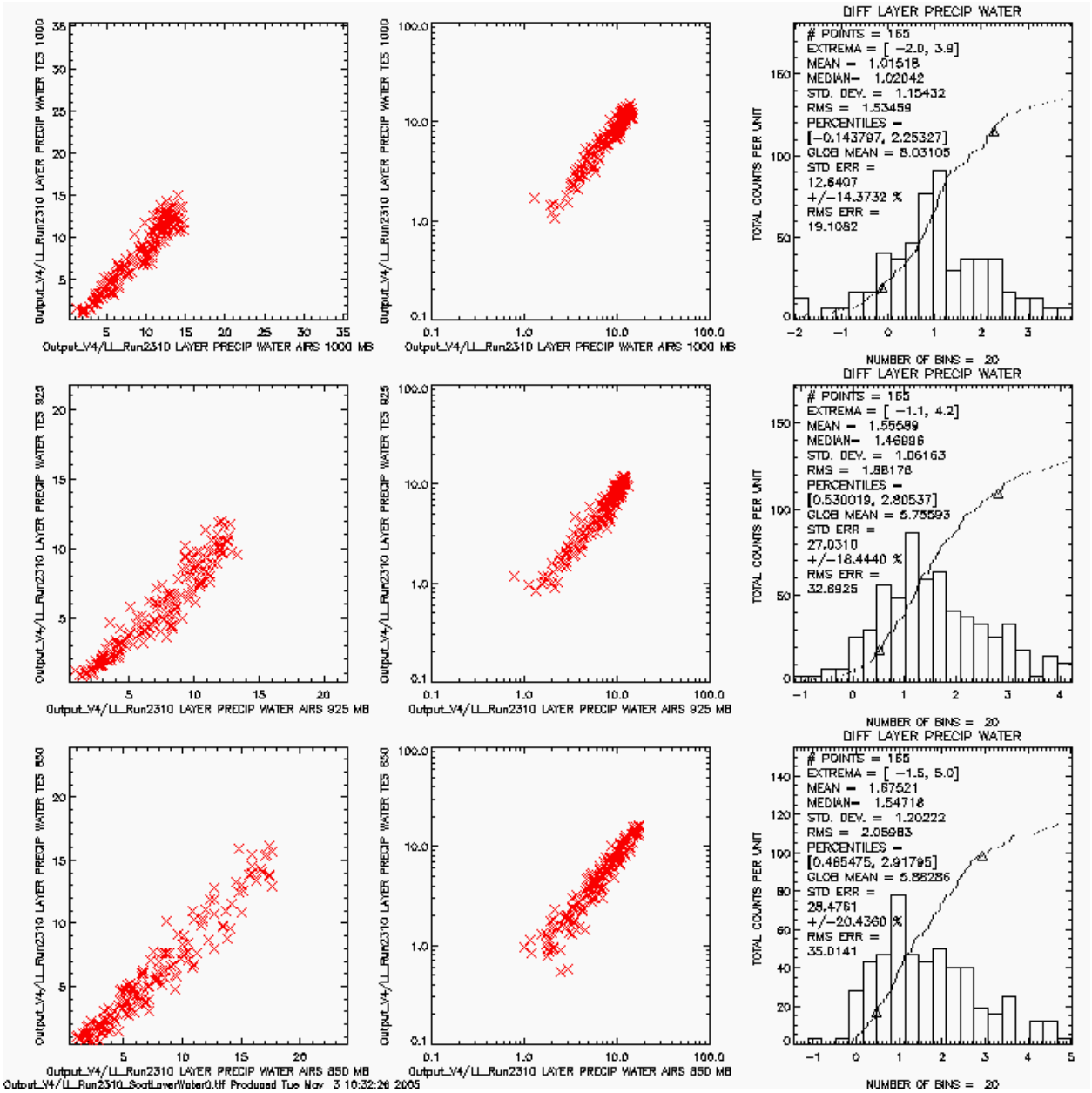

Figure 63: Scatterplots of layer precipitable water for the near surface layers of Run ID 2310. The figures have AIRS data plotted on the x-axis and TES data plotted on the y-axis.

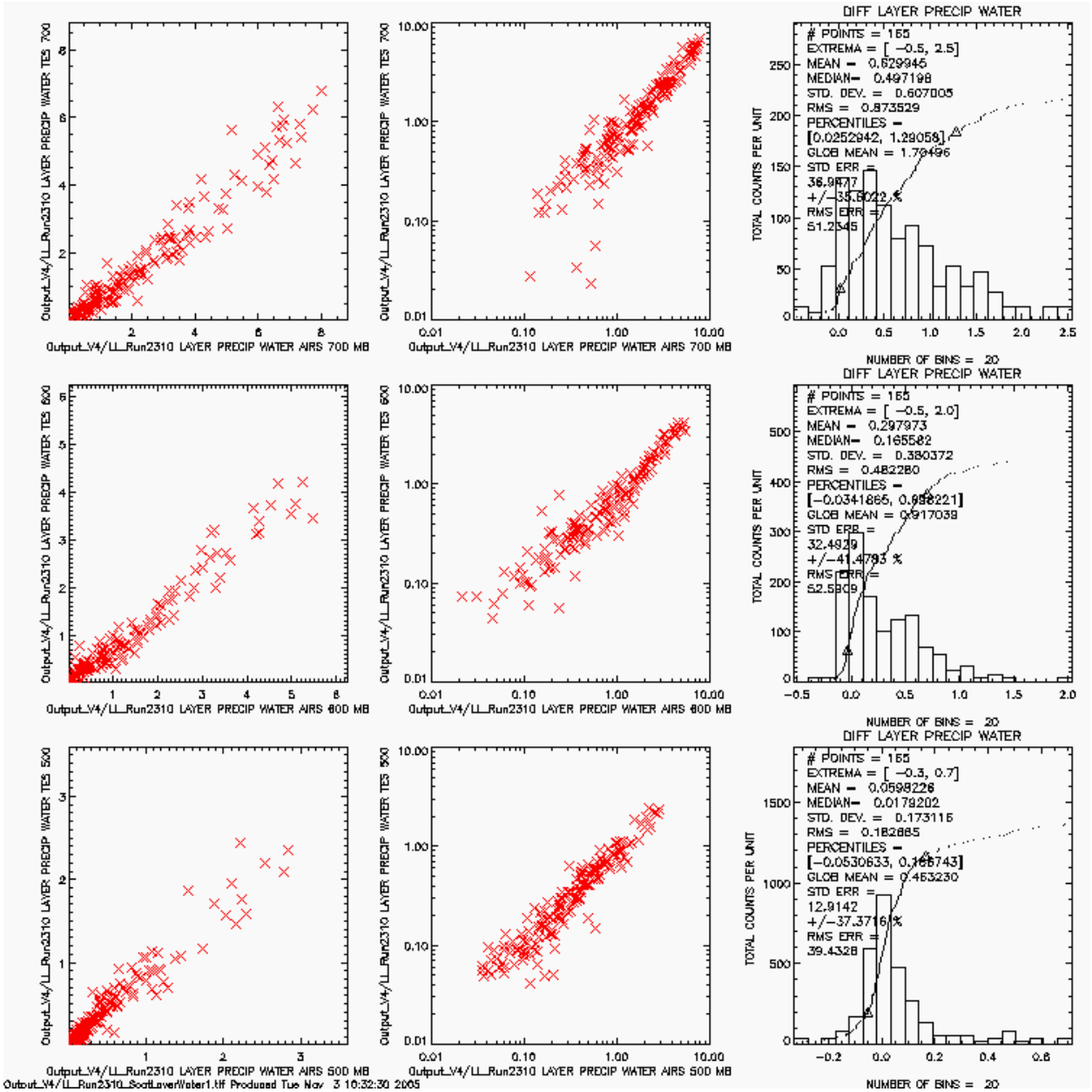

Figure 64: Scatterplots of layer precipitable water for the near mid-atmosphere layers of Run ID 2310.

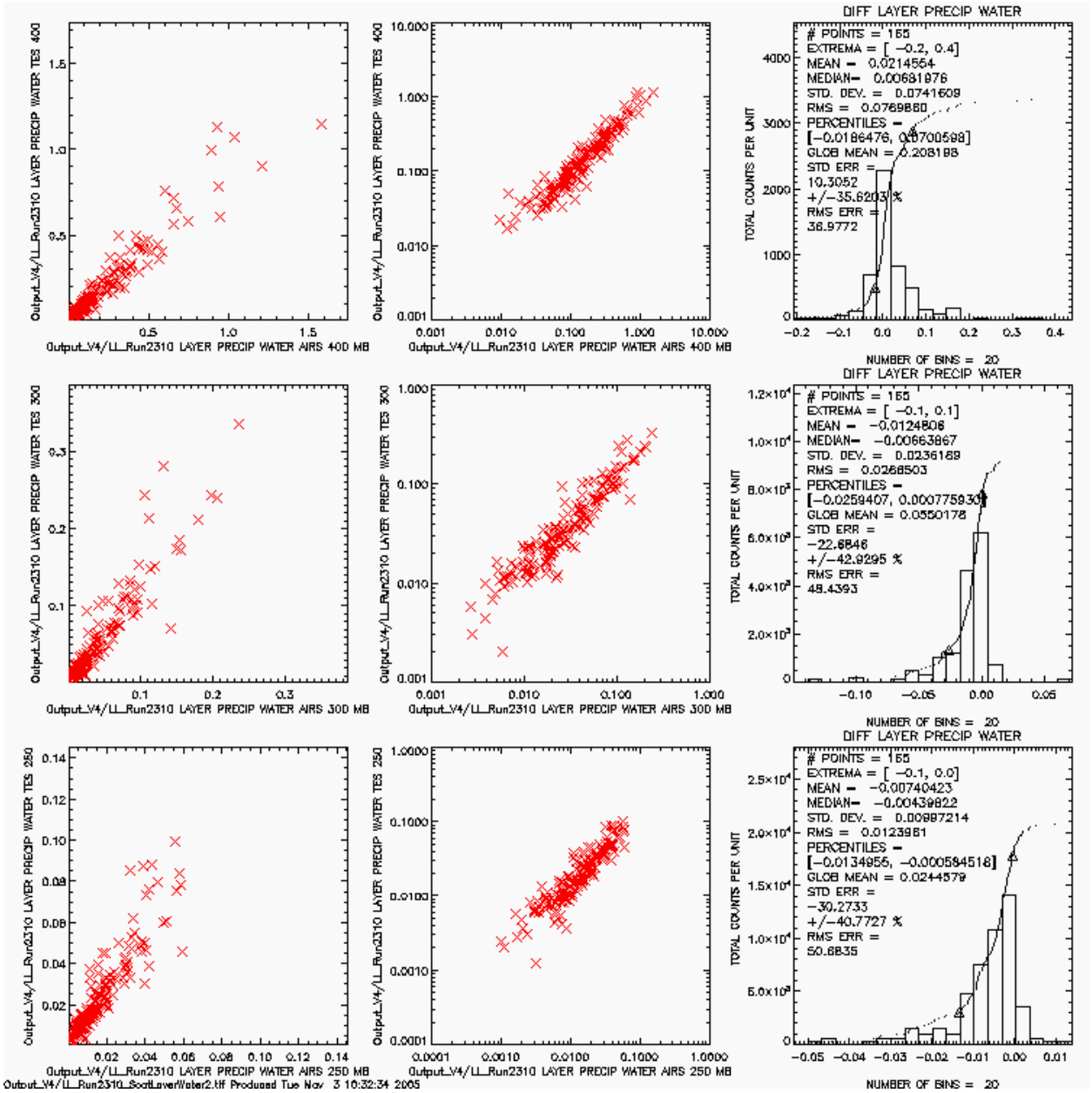

Figure 65: Scatterplots of layer precipitable water for the upper layers of Run ID 2310.

6.3 TES Water Vapor Comparisons with Aircraft Measurements

During the Aura Validation Experiment (AVE) in October 2004, two instruments measured water vapor *in situ* from the WB-57 high-altitude aircraft: the NOAA Aeronomy Laboratory frost point hygrometer and the JPL Laser Hygrometer (JLH). The frost point hygrometer determines the frost point of the ambient environment by

measuring the temperature required to maintain a layer of frost on a mirror. The reflected signal from a blue light-emitting diode is used to control a heater that maintains the frost thickness. A platinum RTD thermistor is used to measure the mirror temperature to 0.1 C precision. The mirror can be heated or cooled at a rate of 20°C per second. Frost point temperatures are converted into water vapor mixing ratios using the Clausius-Clapeyron equation and pressure measurements by the PT instrument on the WB-57 aircraft. JLH is a tunable diode laser spectrometer that measures water vapor by near-infrared absorption in the 7300 cm-1 absorption band [May, 1998]. Pressure and temperature measurements by the PT instrument are used to convert JLH water concentrations to mixing ratios. JLH has a reported accuracy of 7%. Both hygrometers report water vapor at 1-sec time resolution, which corresponds to approximately 200 meters along the aircraft path.

Planned TES step and stare nadir observations coincided with WB-57 aircraft flight paths on five days, as listed in Table 4. Tropospheric water vapor was highly variable during AVE due to local convection, clouds, and the passage of weather systems. As a result, it was desirable to carry out water comparisons between TES and the aircraft that were close in time and location.

The best comparison opportunity was during the October 31, 2004, WB-57 flight in clear sky over the Gulf of Mexico. The WB-57 aircraft spiraled from 130 mb down to 380 mb and back up again directly between two TES Step & Stare scans at 27.3°N, 88.6°W and 26.9°N, 88.5°W (Figure 66). The vertical profiles of tropospheric water vapor from this spiral are shown in Figure 67. The two aircraft instruments and TES water vapor compare favorably, although the *in situ* measurements show lower mixing ratios at 300 mb. On October 31, the aircraft profile occurred within 35 km and 1 hour of the TES scans. Some of the differences seen may be due to atmospheric variability. The next plot (Figure 68) shows an example of variability in two JLH water profiles (takeoff and landing) and the nearest TES Step & Stare scan on November 5, 2004. The differences between aircraft and TES water profiles are comparable to the differences in water vapor between takeoff and landing in Houston, 4.8 hours apart. These comparisons do not take into account the fact that TES has variable sensitivity and resolution throughout the atmosphere. A more thorough comparison using TES averaging kernels is currently underway.

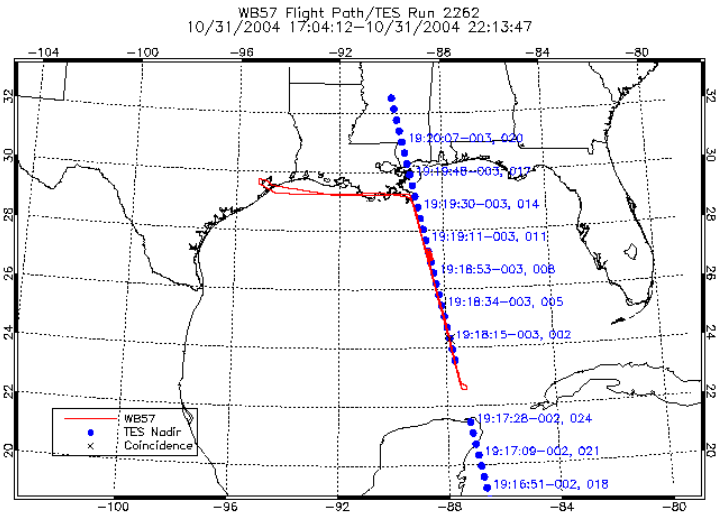

Figure 66: Flight path of the WB-57 aircraft (red line) superimposed on the TES nadir Step & Stare ground track. The spiral is located between two consecutive TES scans (figure prepared by Ming Luo).

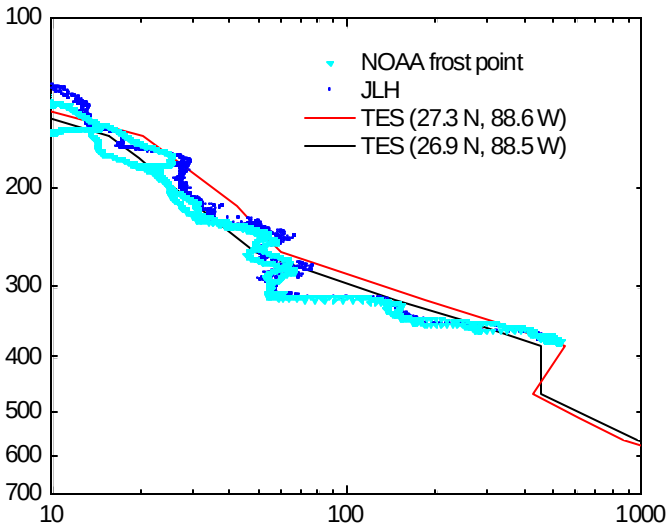

Figure 67: Comparison of TES water profiles on October 31, 2004, with WB-57 aircraft instruments NOAA frost point hygrometer (cyan) and JLH (blue). The aircraft data are within 35 km of two adjacent TES Step & Stare scans (black line and red line).

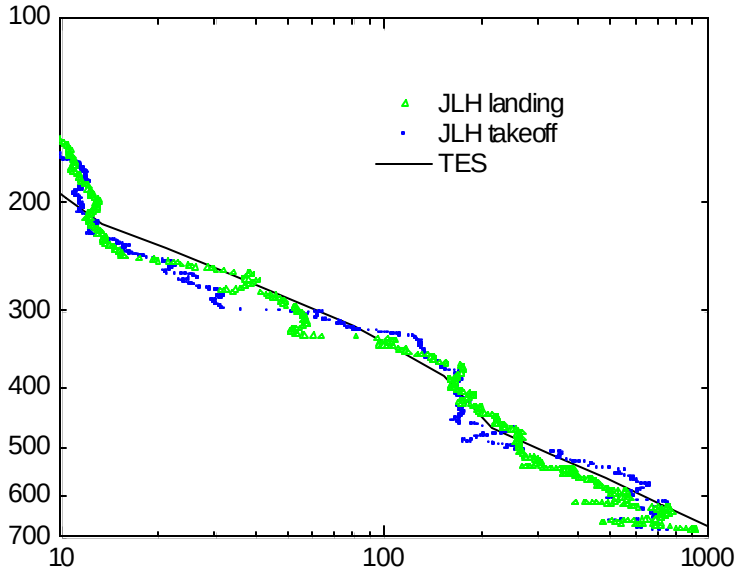

Figure 68: Comparison of TES water profile on November 5, 2004, with WB-57 high-altitude aircraft instrument JLH on takeoff (blue) and landing (green). The aircraft measurements are within 130 km and 2.7 hours of the TES overpass.

7 Validation of TES Temperature Retrievals

7.1 Validation of TES Temperature Profiles

Figure 69 through Figure 73 show comparisons of temperature profiles measured by AIRS and TES. The differences (AIRS-TES) are less than 1K for pressures between900 and 300mb. In the upper troposphere and near the tropopause, TES is about 2K warmer than AIRS.

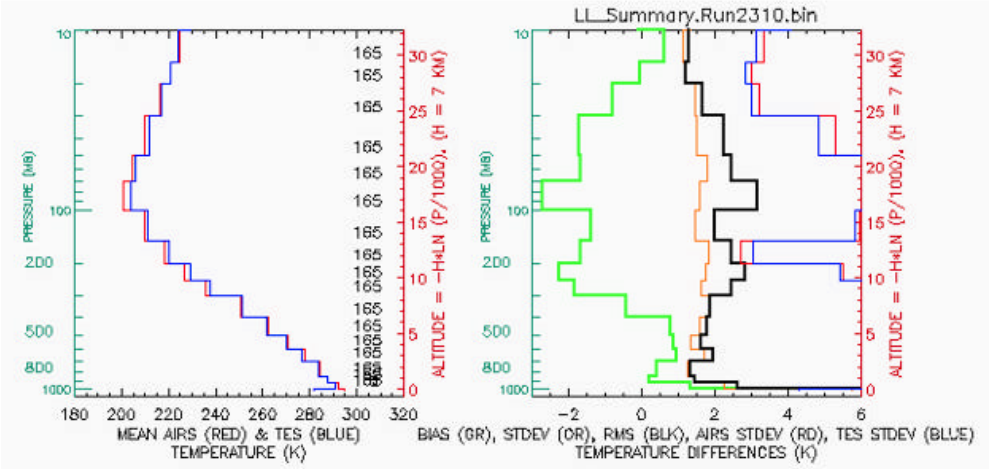

Figure 69: The mean temperature profile (left panel) and bias and standard deviations (right hand panel) for Run ID 2310.

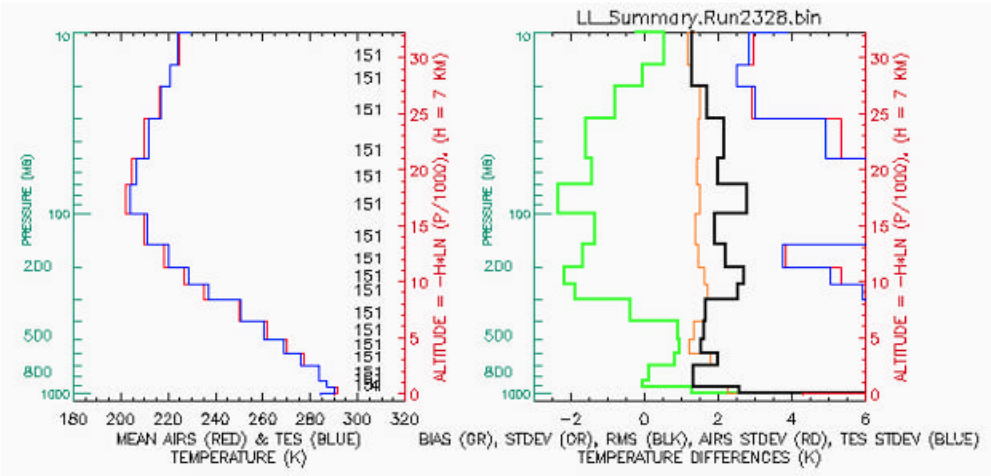

Figure 70: The mean temperature profile (left panel) and bias and standard deviations (right hand panel) for Run ID 2328.

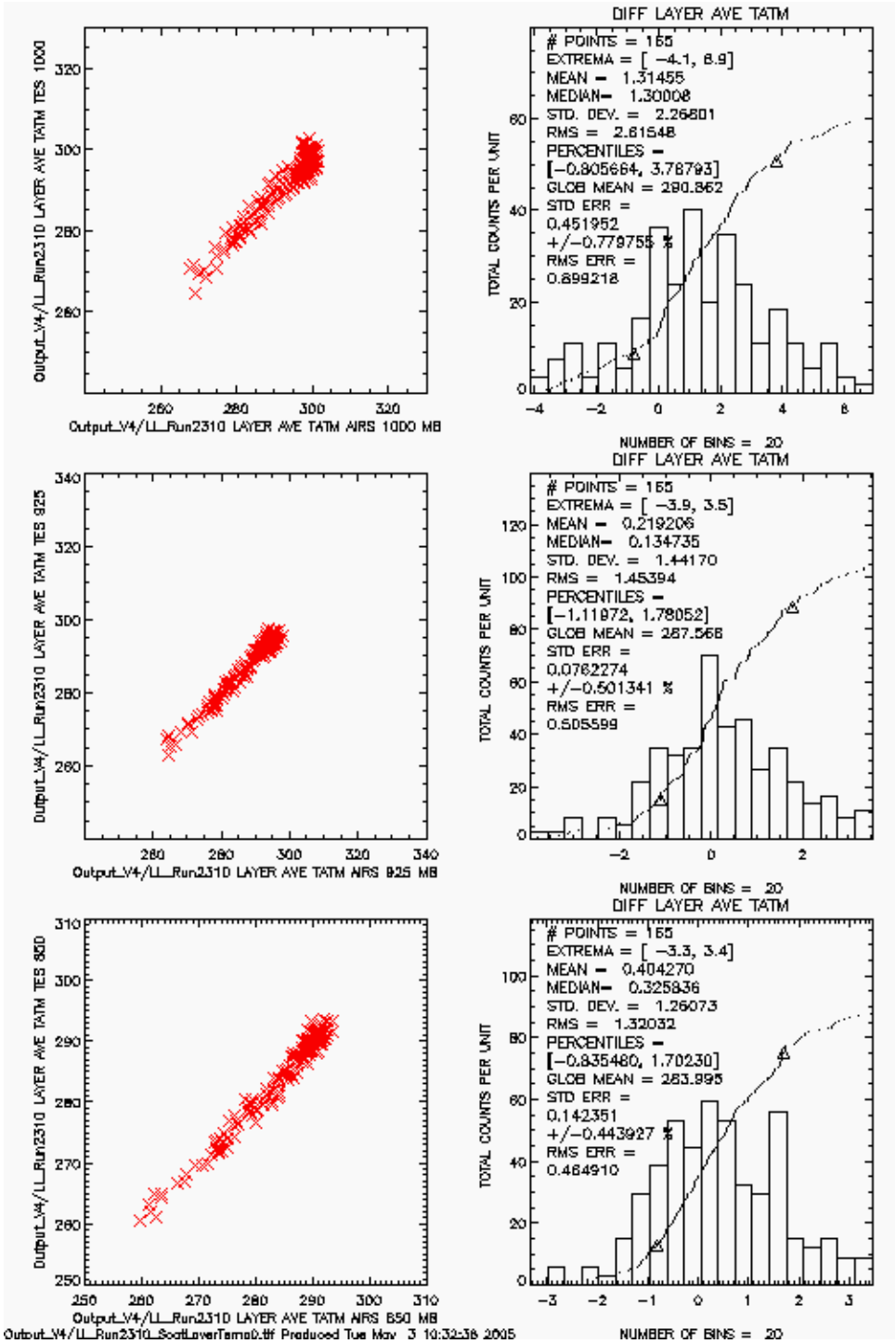

Figure 71: Scatter plots of temperature for the lower layers of Run ID 2310.

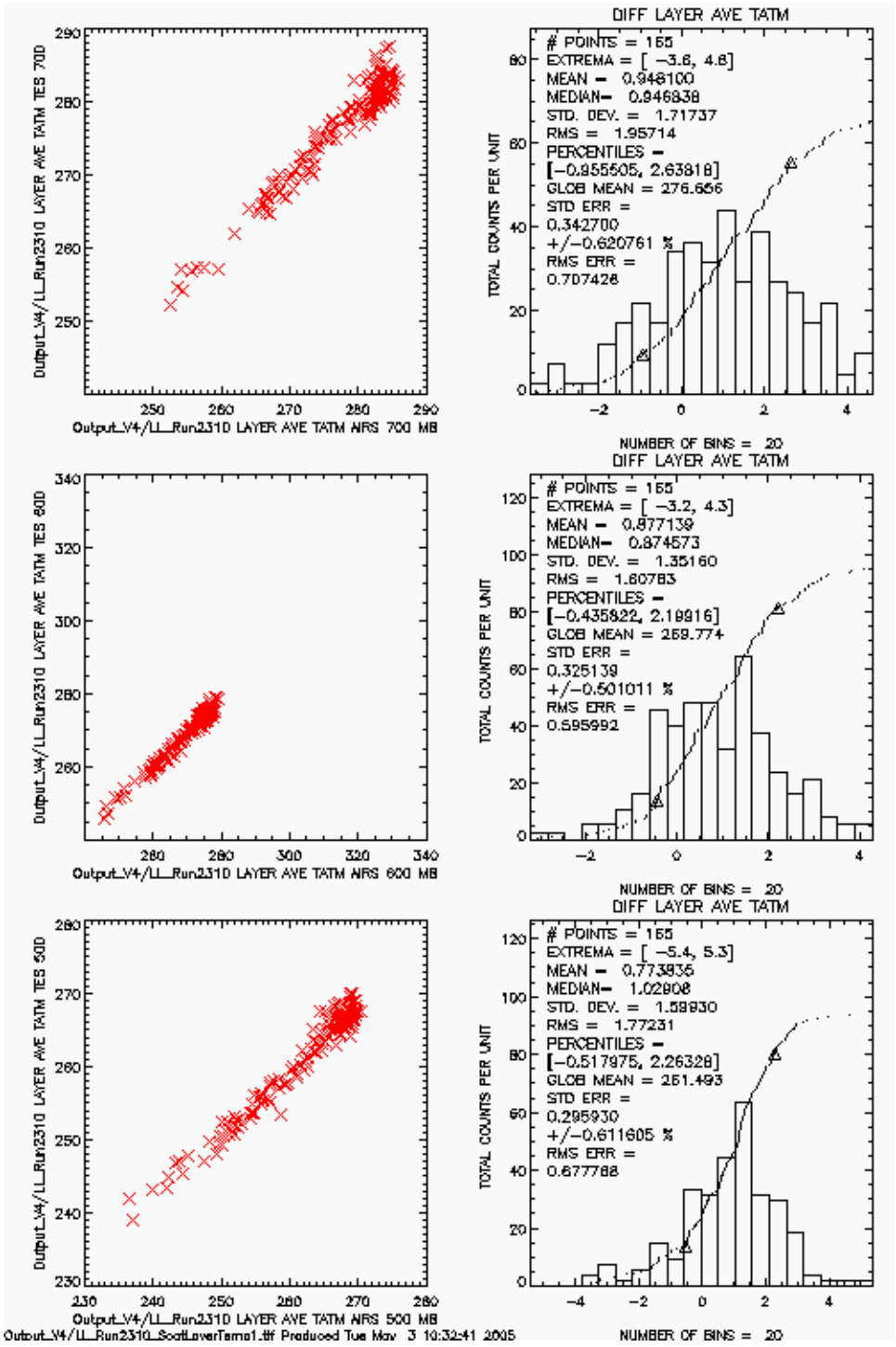

Figure 72: Scatter plots of temperature for the middle layers of Run ID 2310.

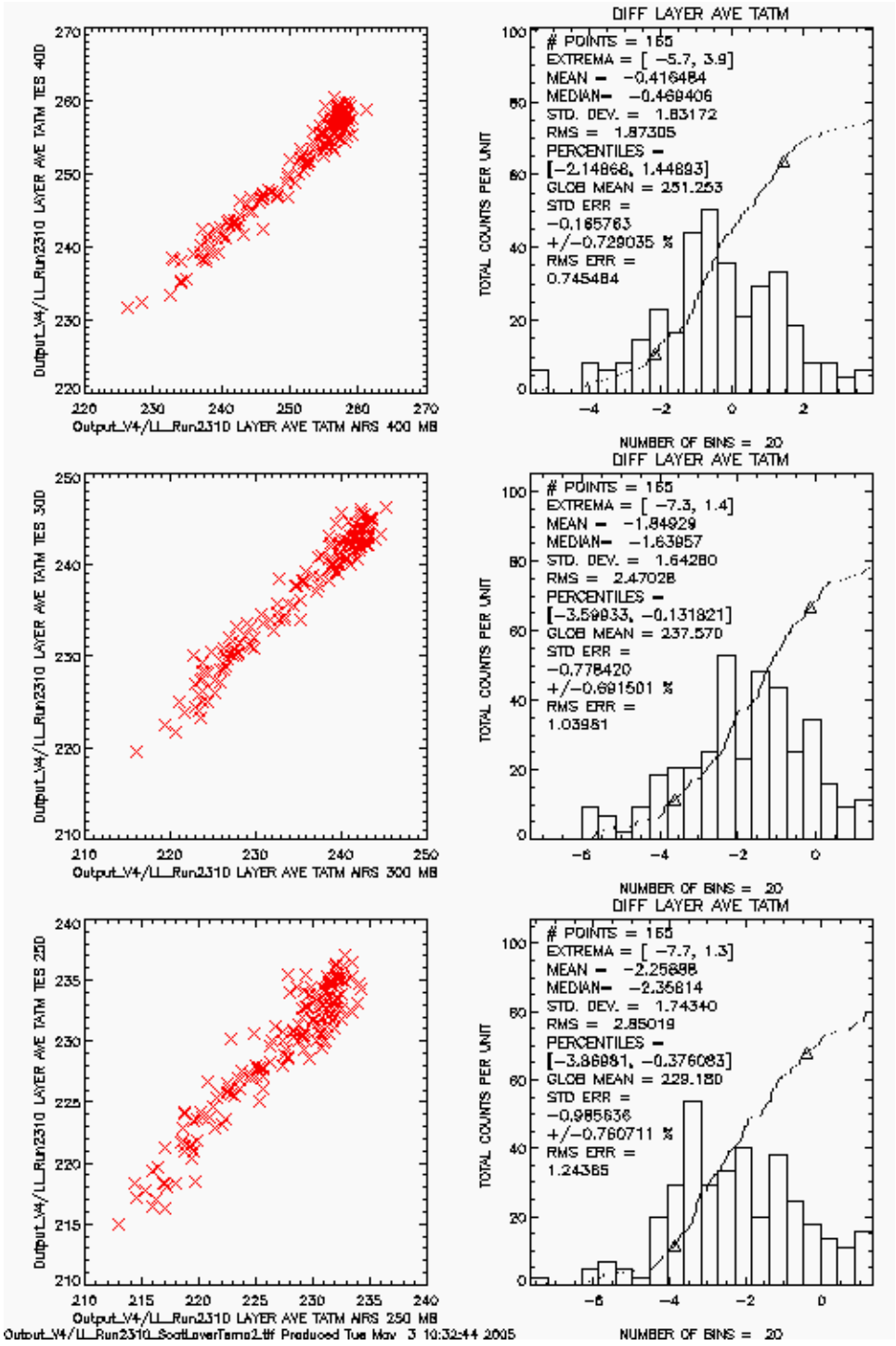

Figure 73: Scatter plots of temperature for the upper layers of Run ID 2310.

7.2 AIRS Case Studies for Validating TES Temperature Retrievals

The objective of an accurate retrieval of species profiles from TES using thermal remote sensing is critically dependent on the accuracy with which the temperature profiles can be established. TES presently performs a simultaneous temperature, water vapor, and ozone retrieval using the water vapor and ozone spectral regions in the TES 2A1 (1100 – 1325 cm^{-1}) and1B2 (920-1160 cm^{-1}) filters, respectively. Initially the magnitude of the noise in the TES 2B1 filter (650-900 cm^{-1}) was considered to be such that this band would not make a positive contribution to the retrieval accuracy of the temperature profiles. A preliminary assessment has indicated that inclusion of this band does provide additional information (degrees of freedom) and can lead to improved temperature profile accuracy (J. Worden, private communication). Our past research efforts have suggested that there may be a systematic difference in the forward model between the v_2 region of carbon dioxide and other spectral regions involving carbon dioxide as well as other species (e.g. water vapor). Systematic errors of this type must be eliminated to assure a positive impact on the temperature retrieval.

In order to reach this objective the TES absorption coefficients, generated using LBLRTM and spectroscopic line parameters, must provide consistency both between and within species. Previous aircraft HIS CAMEX validations showed inconsistencies between temperature profiles retrieved using the CO_2 v_2 and H_2O v_2. Since then we have performed additional validations with AIRS observations. AIRS high radiometric accuracy (on the order of tenths of degrees in brightness temperature) and extended spectral coverage makes it a good tool for investigating these type of issues in the forward model calculations. Three AIRS clear sky nighttime cases are being critically investigated.

The three AIRS observations presented are from: 1) an AIRS validation campaign off the Virginia coast near the Chesapeake Bay Light Platform, 2) the Mediterranean Sea just off the Italian coast during Aerosol Direct Radiative Impact EXperiment (ADRIEX), and 3) the Tropical Western Pacific (TWP) ARM site. All three cases are over water where the surface emissivity is well characterized and during the nighttime in order to avoid Non-LTE effects in the CO_2 v_3 band. All three cases show inconsistencies in the temperature retrievals between CO_2 v_2 and CO_2 v_3 spectral regions. Figure 74 is from the AIRS Chesapeake Bay case where the top panel shows the AIRS upwelling observations, which have a resolution resolving power of 1200 (e.g. resolution = 0.5 cm^{-1} at 600 cm^{-1}). The next three panels are residual plots (AIRS – LBLRTM) using: (i) radiosonde, (ii) the retrieved temperature profile from the CO_2 v_3 spectral region, (iii) the retrieved temperature profile from the CO_2 v_2 spectral region. The temperature values above radiosonde measurements at 100 mb were supplemented with AIRS temperature retrieved values. The spectral regions used for the retrievals are indicated with dashed lines. The CO_2 v_3 and CO_2 v_2 retrieved temperature profiles and corresponding differences from the original radiosonde are plotted in Figure 75 and Figure 76, respectively. It is apparent in Figure 75 and Figure 76 that the retrieved temperature profiles retrieved CO_2 v_2 vs. CO_2 v_3 are not consistent. For example, there are differences between the two retrieved profiles in the middle to upper troposphere of approximately 4K with CO_2 v_2 being warmer. Another important retrieval metric to look at is the averaging kernels for the

temperature retrievals from both spectral regions. The averaging kernels in Figure 77 and Figure 78 show that both retrievals are sensitive over the whole temperature profile.

For the other two AIRS observations over the Mediterranean Sea and the ARM TWP we applied the same retrieval methodology. The initial input for the Mediterranean Sea calculation is a coincident and collocated NCEP NWP profile. Figure 79 contains the AIRS Mediterranean Sea observations and residuals. Again, the results for the temperature retrievals using the CO_2 v_2 and v_3 regions are inconsistent; refer to Figure 80 and Figure 81. The AIRS observations for the ARM TWP case are shown in Figure 82. The initial temperature profile was obtained from an ARM radiosonde with ECMWF temperature values supplemented above 60 mb. As in the previous two case studies the retrieved temperature profiles from the CO_2 v_2 and v_3 regions are inconsistent with CO_2 v_2 being warmer by approx. 4 K in the middle to upper troposphere.

In summary the impact on the retrieved temperature profile as a consequence of retrieving using CO_2 v_2 or v_3 is effectively the same for all three cases. Furthermore, the resulting spectral residuals for all three cases for CO_2 v_2 and v_3 are effectively the same, with differences of up to 2 K in brightness temperature (see Figure 74, Figure 79 and Figure 82). We are presently investigating which spectral region is correct by utilizing HIS and SHIS aircraft data. The near term solution will be to empirically correct CO_2 absorption coefficients based on the observations. For the long-term more physical solution we are collaborating with Mary Ann Smith and her group at NASA Langley who are performing CO_2 laboratory measurements.

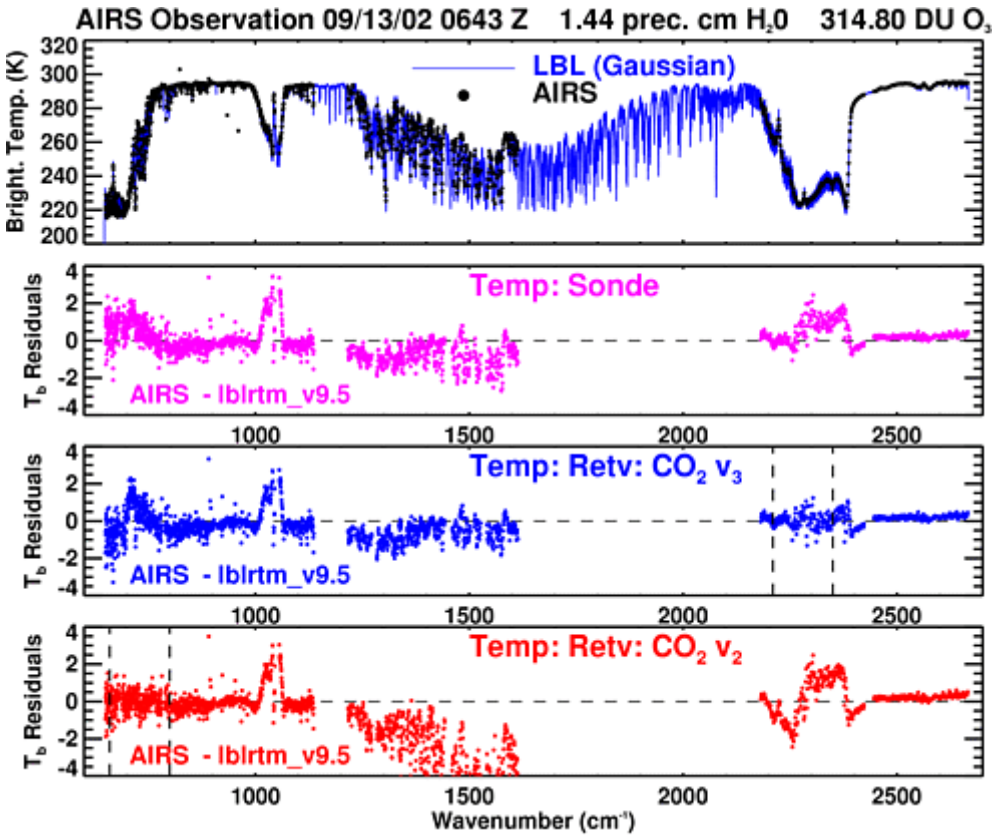

Figure 74: The top panel is contains AIRS Chesapeake Bay observations and a line-by-line radiance spectrum plotted in the background for reference only. The bottom three panels are residual plots between the AIRS observations and the Forward Model calculations using temperature inputs from: 1) radiosonde, 2) retrieved temperature profile from the CO_2 v_3 band (as outlined with black vertical dashed lines, and 3) retrieved temperature profile from the CO_2 v_2 band.

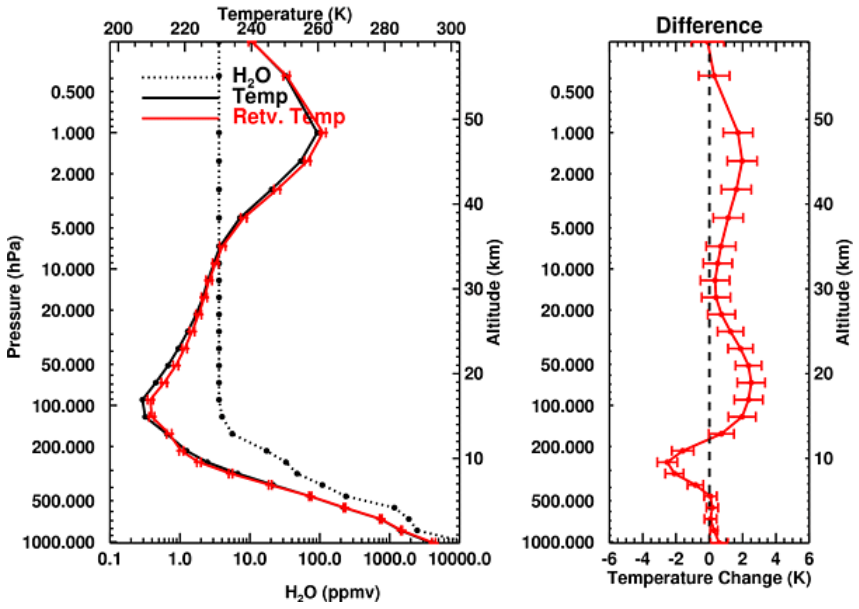

Figure 75: AIRS Chesapeake Bay retrieved temperature profile from the CO2 v3 spectral region.

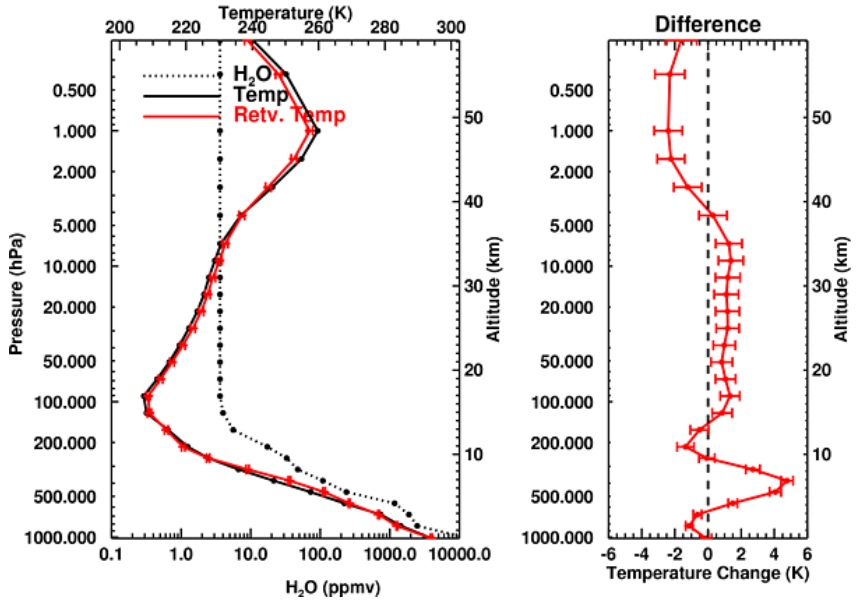

Figure 76: AIRS Chesapeake Bay retrieved temperature profile using CO2 v2 spectral region.

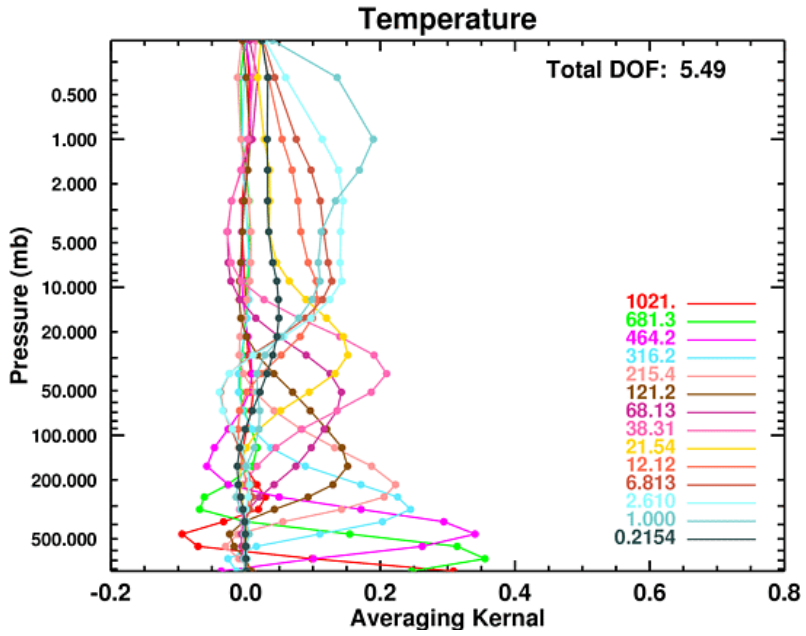

Figure 77: Averaging kernel from the temperature retrieval using the CO2 v3 band. The averaging kernel for every-other retrieval pressure level is plotted.

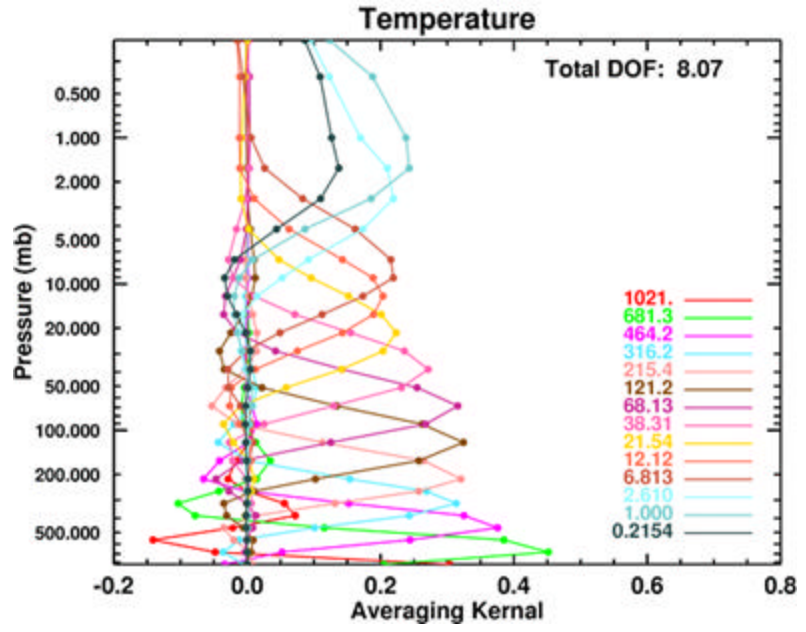

Figure 78: Averaging kernel from the temperature retrieval using the CO2 v2 band. The averaging kernel for every-other retrieval pressure level is plotted.

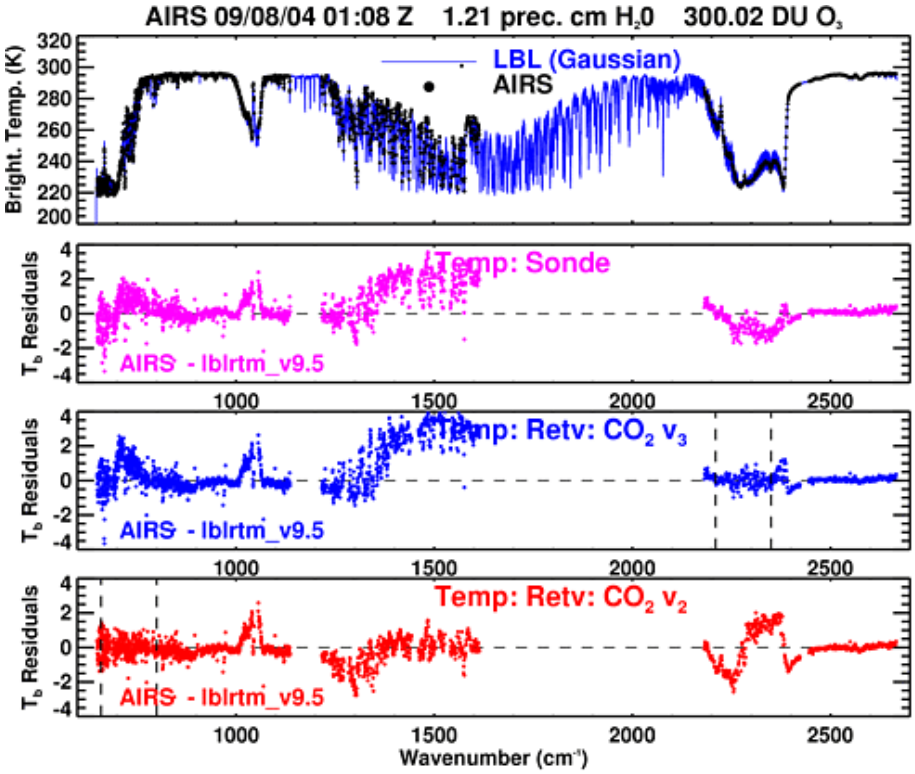

Figure 79: AIRS Italy Mediterranean Sea observations using the same plotting methods as in Figure 74.

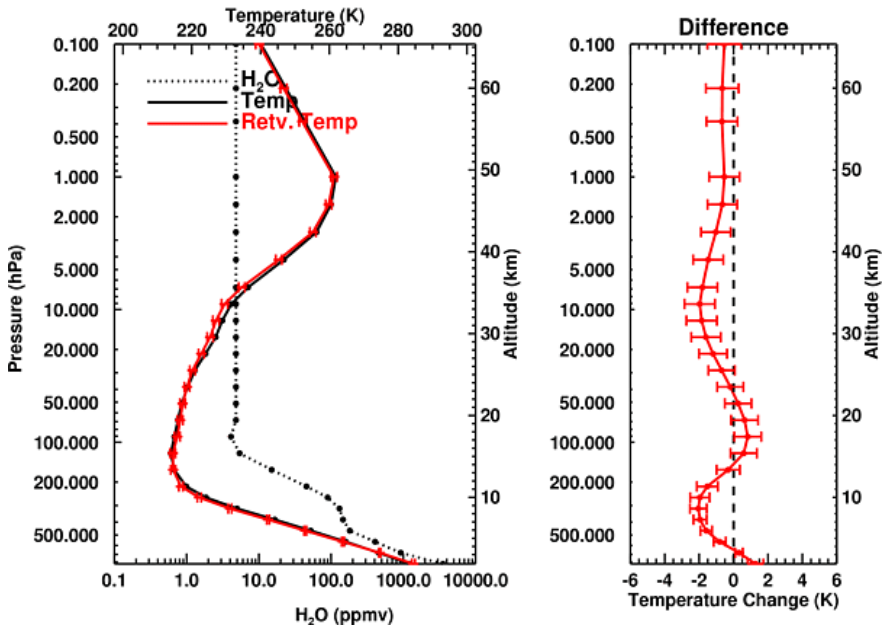

Figure 80: AIRS Italy Mediterranean Sea retrieved temperature profile from the CO2 v3 spectral region.

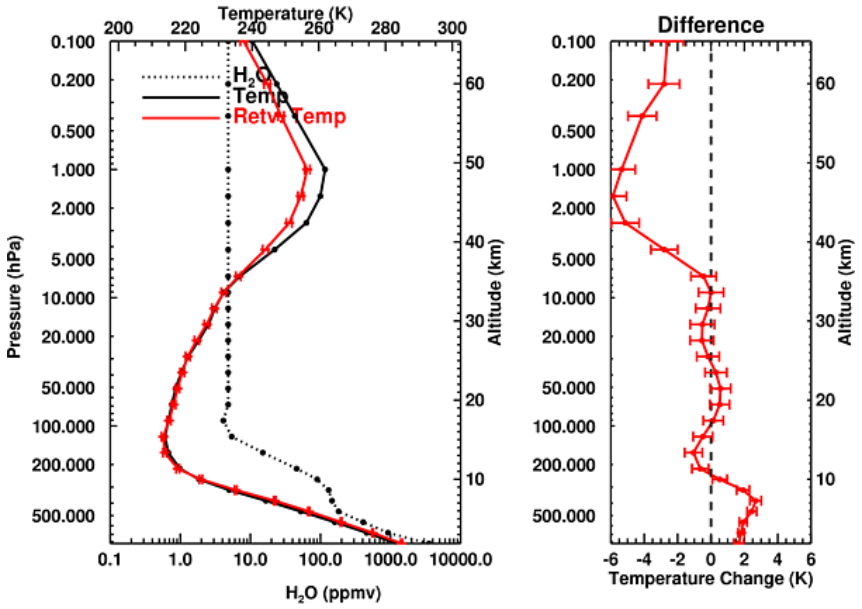

Figure 81: AIRS Italy Mediterranean Sea retrieved temperature profile from the CO2 v2 spectral region.

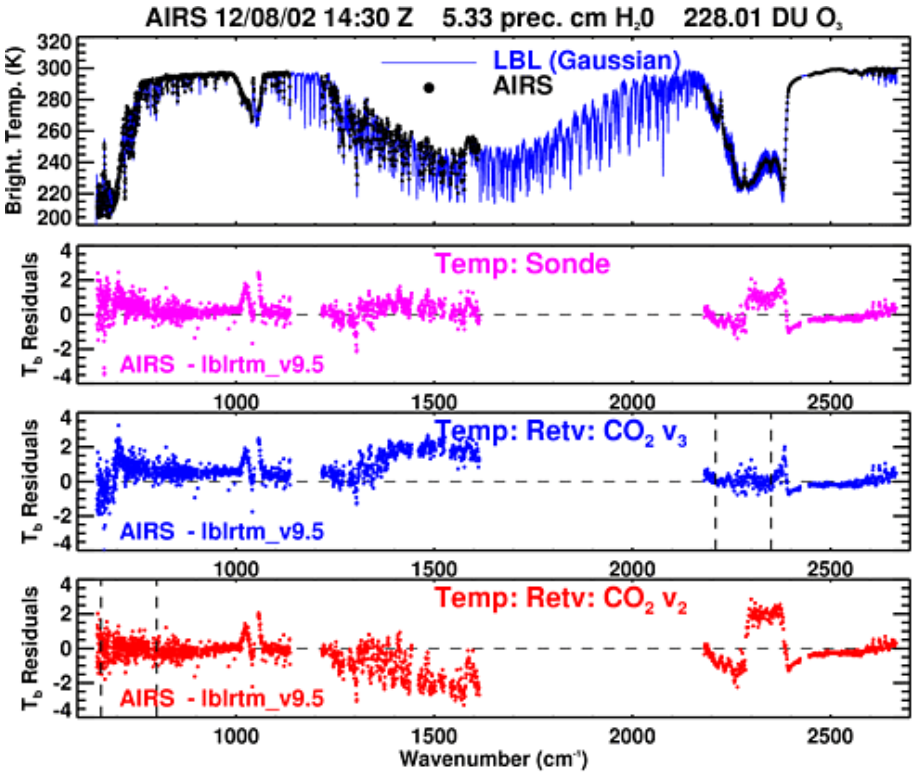

Figure 82: AIRS observations over the ocean near the ARM Tropical Western Pacific site using the same plotting methods as in Figure 74.

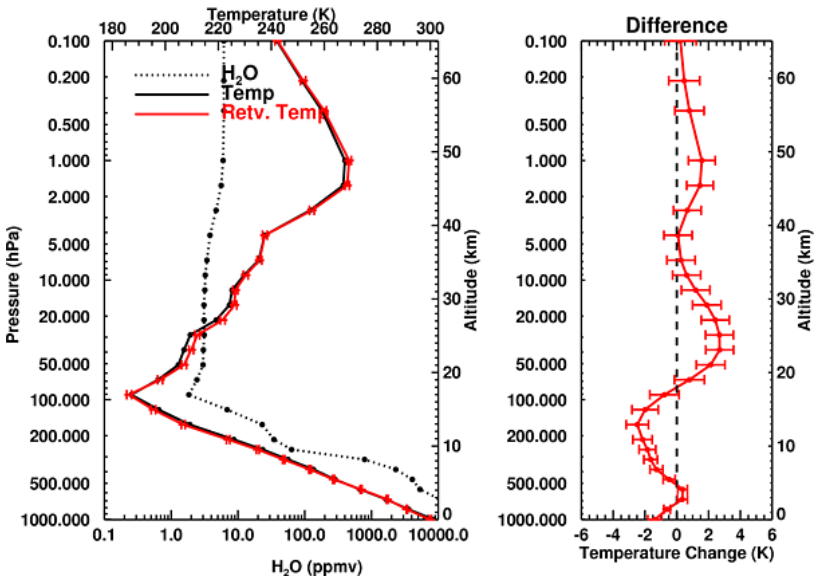

Figure 83: AIRS ARM TWP retrieved temperature profile from the CO2 v3 spectral region.

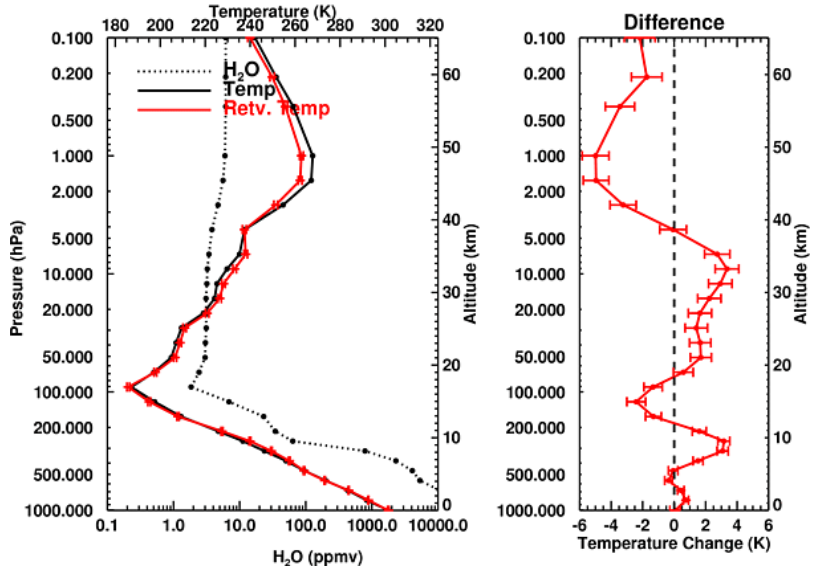

Figure 84: AIRS ARM TWP retrieved temperature profile from the CO2 v2 spectral region.

8 Validation of TES Cloud Top Pressure

The validation of cloud top pressures is challenging, as there are limited sources of data for comparison. As an initial comparison, we matched MODIS cloud products to TES observations. The optical depths are expected to be different, given that MODIS relies on visible channels in the daytime, but there should be good agreement with cloud top pressure. MODIS is located on EOA-Aqua, so it has a 15 minute time mismatch, and exact location matching.

Figure 85, Figure 86 and Figure 87 show AIRS visible imagery, with the TES footprints marked in blue. The nearest MODIS 5km by 5km cloud product is matched to each TES footprint. The clouds are plotted on a pressure-latitude figure, and the size of the marker is proportional to the cloud optical depth. These figures show the cloud comparisons for three step and stare measurement sets. The MODIS cloud mask colors indicate cloudy (black), probably cloud (blue), probably clear (green), and clear (red). There is generally good agreement when MODIS is confident in their cloud detection. We see that there are times when TES reports small optical depths at cloud top pressure very different from MODIS, but many of these cases are when MODIS reports near surface clouds.

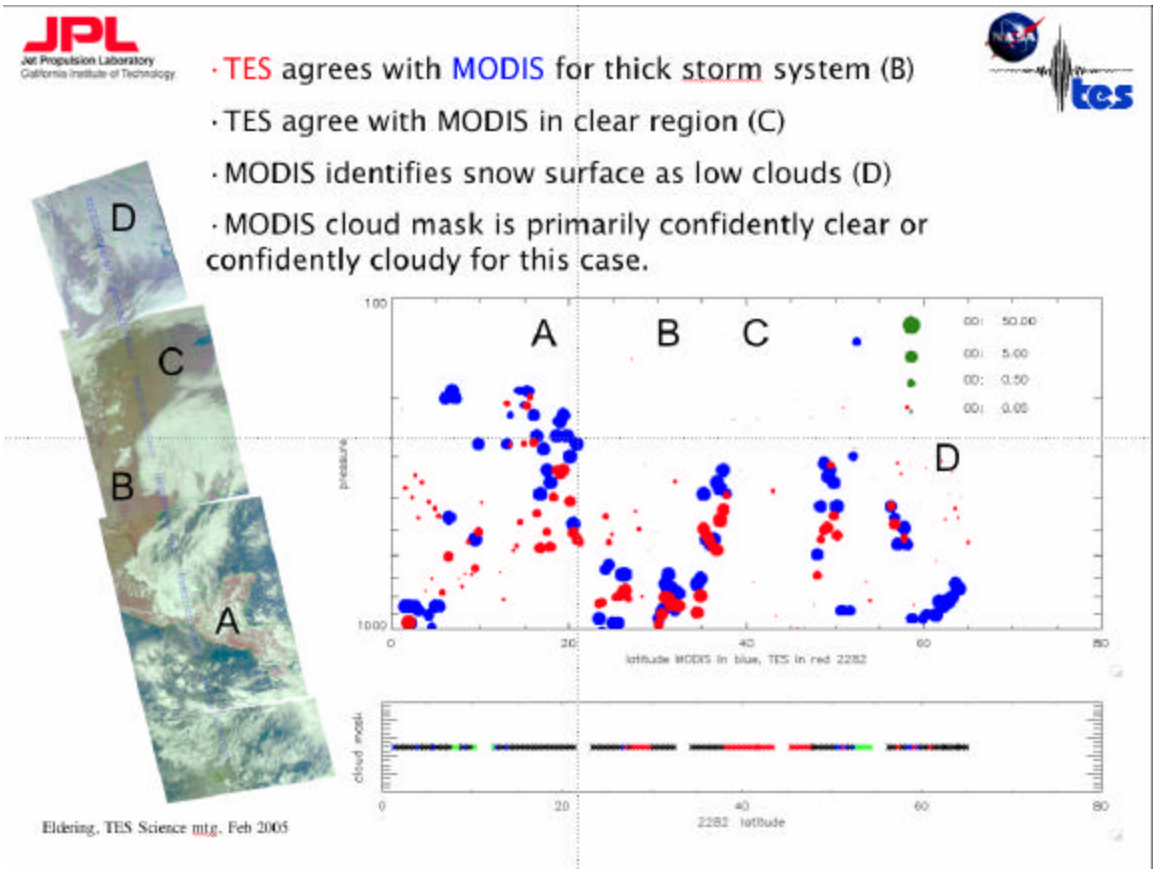

Figure 85: AIRS visible imagery, MODIS and TES cloud top pressure as a function of latitude, and MODIS cloud mask for Run ID 2282.

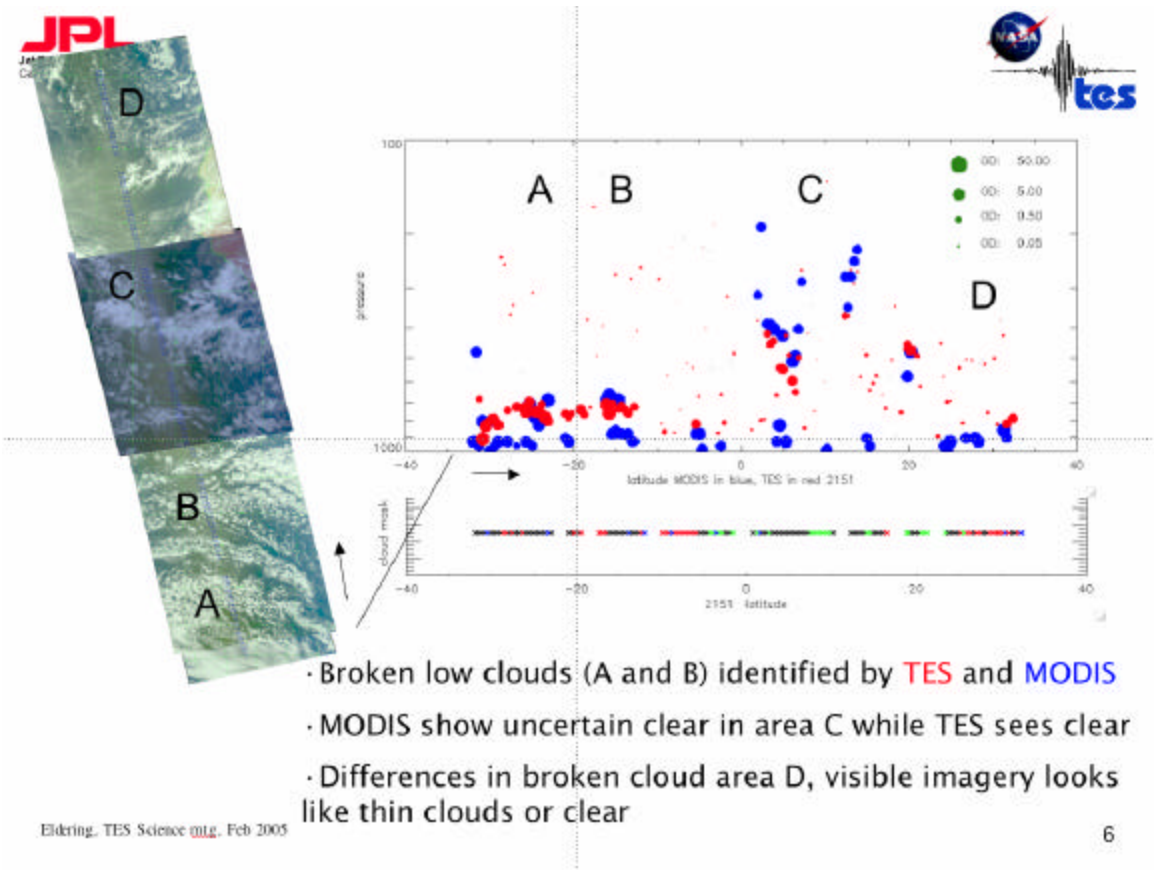

Figure 86: AIRS visible imagery, MODIS and TES cloud top pressure as a function of latitude, and MODIS cloud mask for Run ID 2151.

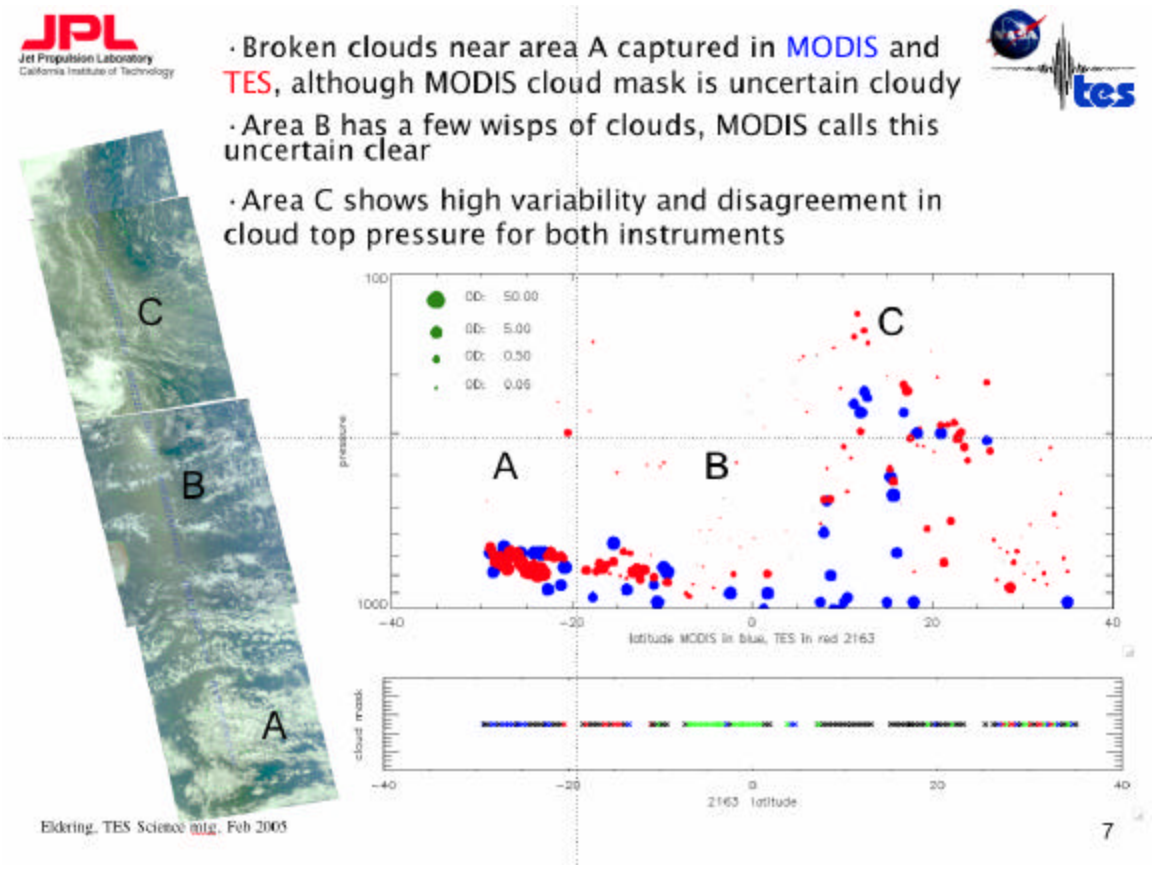

Figure 87: AIRS visible imagery, MODIS and TES cloud top pressure as a function of latitude, and MODIS cloud mask for Run ID 2163.

9 Validation of TES Retrievals of Carbon Monoxide

Limited TES CO retrievals are compared to MOPITT measurements and the *in situ* Argus measurements during October 2004 AVE aircraft campaign. These comparisons not only offer good qualitative checks for TES data, *e.g.*, the characteristics of the CO global distribution or the shapes of their vertical profiles, but also offer initial quantitative validations of TES CO retrievals. The understanding and the usage of the characteristics of TES retrievals, including the roles of *a priori* profiles and the averaging kernels are also demonstrated in these comparisons.

9.1 Comparisons between TES and MOPITT

The retrieval results of TES 16-orbit global survey measurements in Sept 20-21, 2004 (Run ID 2147) have been examined extensively by the TES science team. Figure 88 illustrates CO total column amounts at TES nadir footprints for Run ID 2147. Over 90% of the profiles met the requirements for a successful retrieval according to the current quality criteria. In the future, TES Level 2 retrievals and column values will be mapped to a uniform latitude/longitude grid for each global survey (Level 3 products). An illustration of this is provided in Figure 89 for the CO column. Enhanced tropospheric CO is observed over parts of S. America and Africa, and along the east coast of Asia. These are associated with the well-known seasonal biomass burning or polluted regions. Figure 90 shows TES CO retrievals at two pressure levels in the lower and upper troposphere. They are distinguished by elevated CO at the source regions near the surface and the effect of atmospheric transport on CO distribution in the upper troposphere. The degree-of-freedom for signal from TES CO retrievals are plotted as a function of latitude in Figure 91. Values for the *dofs* of 0.5-2 are achieved, meaning TES measurements provide 0.5-2 pieces of independent vertical information for tropospheric CO. The better *dofs* normally occurred for the daytime tropics with high surface temperatures and clear sky conditions where fewer scan signals were rejected due to clouds.

The CO profiles from MOPITT instrument on Terra are gathered for the same time period of the TES global survey on Sept.20-21, 2004. Figure 92 shows the MOPITT measurement of CO total column overlaid with TES geolocations. It is immediately realized that TES (Figure 88) and MOPITT (Figure 92) global CO agree well qualitatively, *e.g.*, they both detected enhanced CO near the polluted sources. In examining the model field of CO, *e.g.*, the MOZART simulation used as *a priori* for TES CO retrievals, TES and MOPITT measurements revealed some more detailed CO distributions.

Figure 93 and Figure 94 show the comparisons of TES and MOPITT CO total column as functions of latitude for the TES global survey time period in Sept.20-21, 2004. The reported percent errors for the two instruments are plotted as functions of latitude. The global averages of total column errors for CO are 8.7% for TES and 11.7% for MOPITT respectively. Again, we see general good agreement between the two instruments at most

latitudes with the exception of southern high latitudes, where the column CO amounts measured by TES are slightly lower than that of MOPITT. This is believed to be due to the effect of the *a priori* in CO retrievals which will be demonstrated below for different pressure levels.

The TES CO profiles are compared to those of MOPITT closest to TES geolocations. For each given TES profile, a same day MOPITT profile is selected closest to the TES location within 500 km (100 and 200 km range data are examined, but there are less MOPITT data available for the comparison and the conclusions drawn here are the same). The TES CO profiles (~25 levels in troposphere) are interpolated to six MOPITT pressure levels, 850, 700, 500, 350, 250, and 150 hPa.

Figure 95 shows TES and MOPITT CO comparisons at 850 hPa. The averaged CO VMRs over a sliding +/-5^{o} latitude box and the percent difference between the two instruments are shown as functions of latitude. The CO retrieved by the two instruments agrees well in the northern hemisphere but TES is lower in the southern hemisphere. At 700 hPa (not shown), the comparisons are similar to the 850 hPa plots.

Figure 96 shows TES and MOPITT CO comparisons at 500 hPa. Compared to 850 and 700 hPa (Figure 8), the agreement between the two measurements improves. At 350 and 250 hPa (not shown), the comparisons are very similar to the 500 hPa plots. Except the very high latitudes and some location sensitive CO source regions, the agreement between TES and MOPITT CO is less than 10% for these three pressure levels.

Figure 97 shows TES and MOPITT CO comparisons at 150 hPa. The difference between the two instruments is latitude dependent, strongly shown in TES data.

The retrieved profile from an optimal method (x_{ret}) can be expressed as (ref: Clive's book)

$$x_{ret} = Ax + (I - A)x_a + \text{retrieval error due to measurement error}$$

where x is the true profile, A is the averaging kernel of which the rows are regarded as vertical smoothing functions, and x_a is the *a priori* profile. This equation clearly describes that the retrievals of atmospheric vertical profiles (x_{ret}), *e.g.*, CO, for the nadir looking measurements are influenced by the selections of the *a priori* profiles, x_a. The rows of the averaging kernel determined by the sensitivity of the measurement spectra to the profile perturbation and the *a priori* correlation between pressure levels used for the retrieval will affect the retrieved profile by vertically smoothing the true profile.

It can be reasonably concluded that the disagreements between TES and MOPITT CO profiles at 850-700 hPa and at 150 hPa illustrated in Figure 95 and Figure 97 are due to the different *a priori* CO profiles used in the retrievals of the two instruments. The second term in the above equation has a large influence on the retrievals at these levels for both instruments. Currently, TES uses MOZART model results as the *a priori* for CO retrievals, while MOPITT uses a single CO profile that is derived from aircraft measurements (mainly in northern hemisphere). The averaging kernels (or the degree of freedom for signal) calculated for the two instruments from their retrievals are similar

(Deeter et al., 2004). At pressures 500-250 hPa, both instruments obtain more information from their measurements or the first term in above equation dominates showing why better agreement is achieved.

Since the nadir retrievals of CO profile (CO column as well) are influenced by the choices of *a priori*, a comparison with both *a priori* taken into account (ref: Connor & Clive's paper) would be more conclusive than what has been done here. This will be continued effort in validating TES CO retrievals via comparisons to MOPITT and also AIRS data.

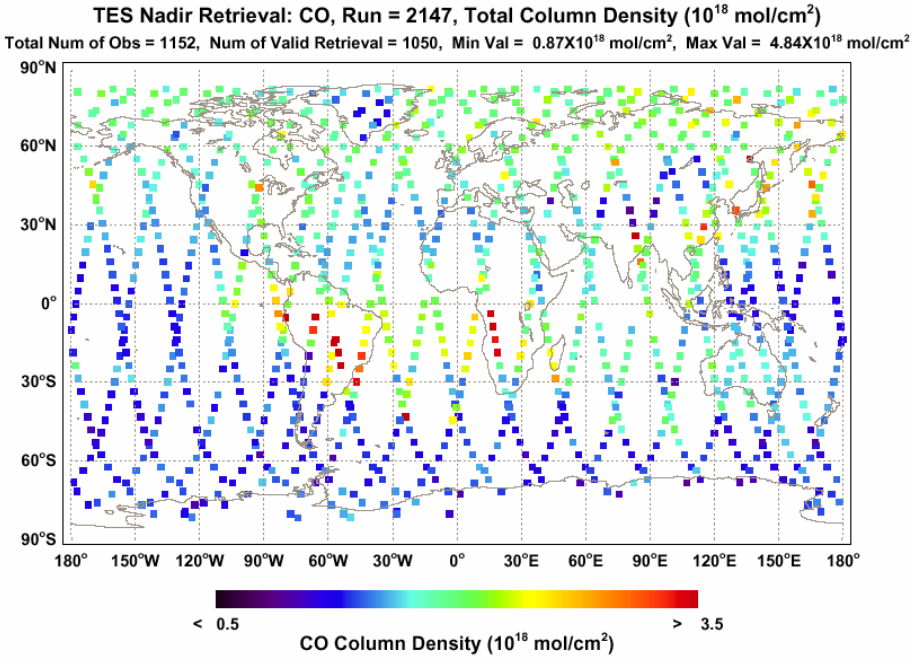

Figure 88: Total column of TES CO at enlarged nadir footprints, for TES Run ID 2147, Sept.20-21, 2004. Elevated CO over and near the coasts of S. America and Africa are observed due to extensive biomass burnings in both regions. Larger CO values also showed up in expected pollution regions in E. Asia.

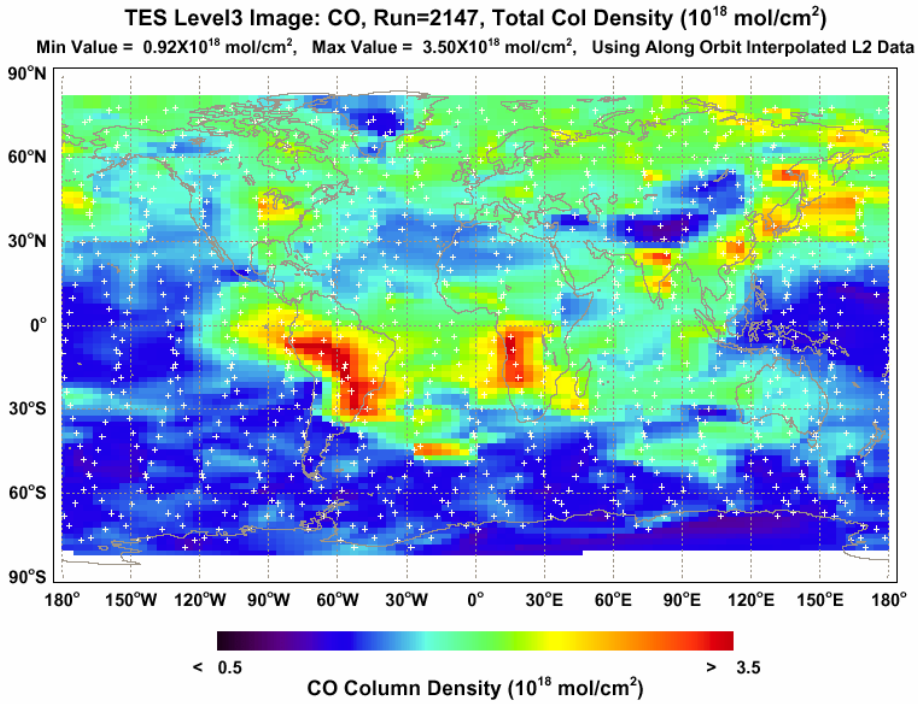

Figure 89: TES CO column in Figure 88 mapped to uniform grids in latitude and longitude, using Delaunay triangulations and 2-D linear interpolation method. White marks are TES geolocations. The features in CO global distributions are more clearly displayed.

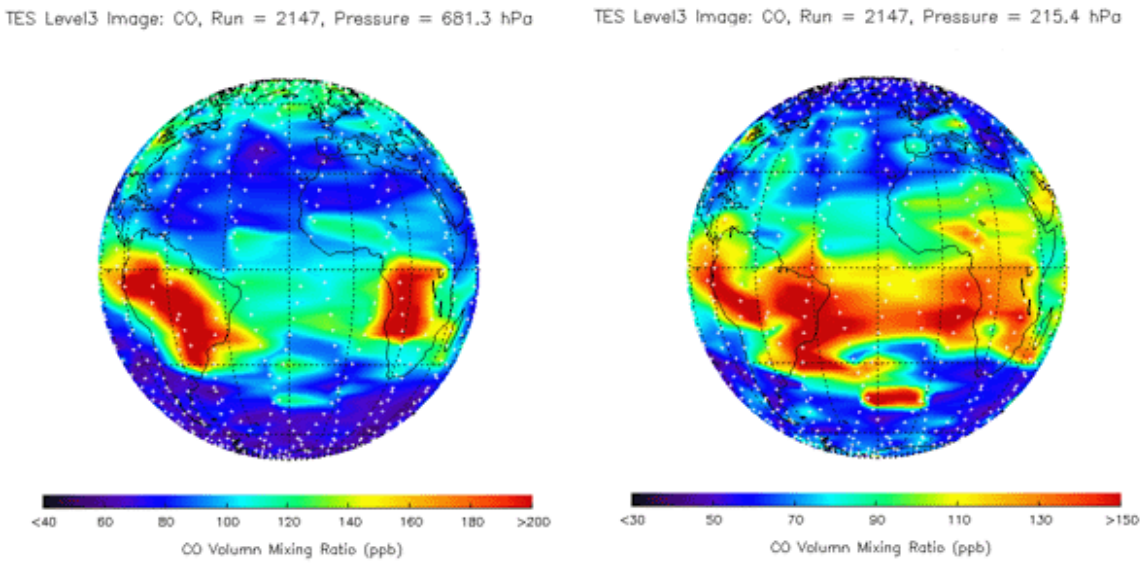

Figure 90: TES CO observations at lower troposphere (left) and upper troposphere (right). They illustrate CO enhancement at the source regions near the surface and the effect of transport on CO distributions near the tropopause.

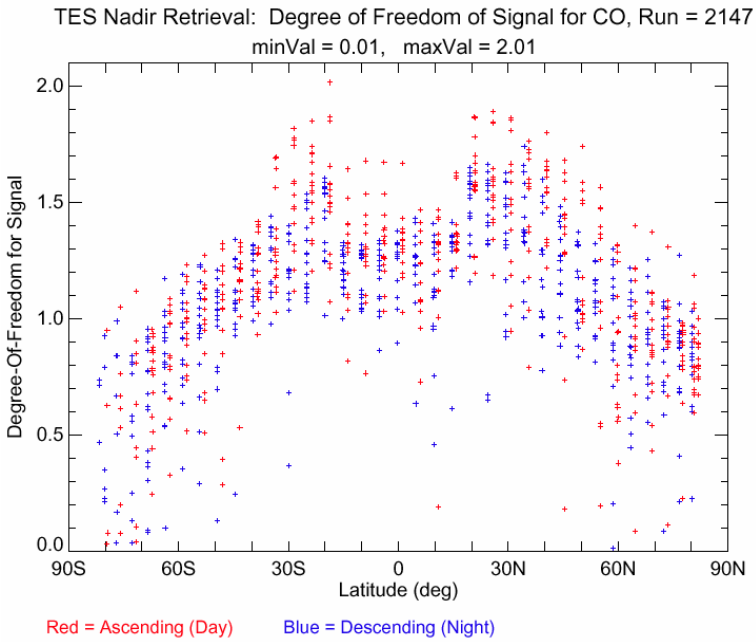

Figure 91: Degree of freedom for signal as a function of latitude for TES nadir CO retrieval in Sept. 20-21, 2004.

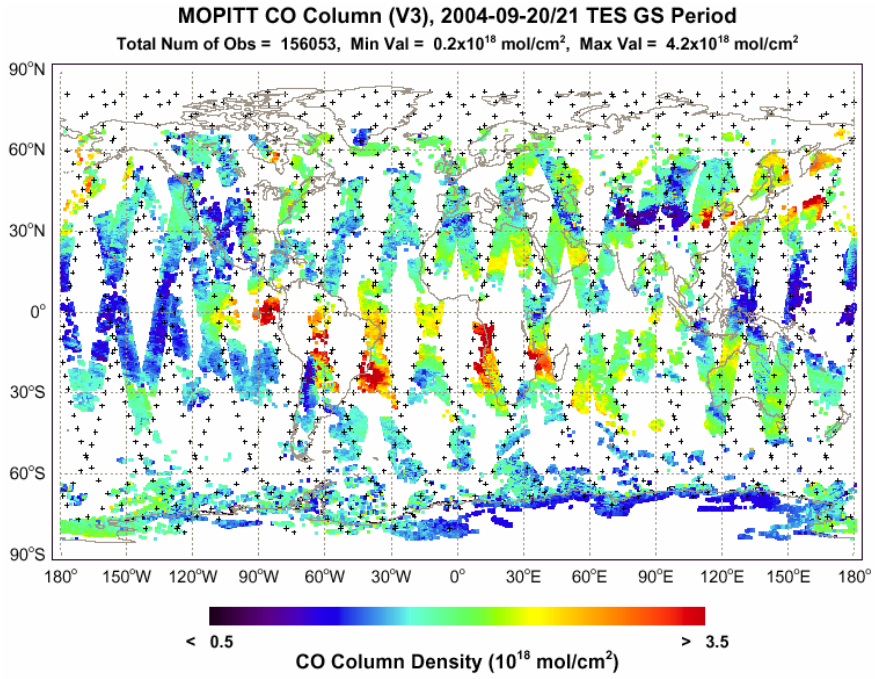

Figure 92: Terra-MOPITT CO total column observed in TES Global Survey period of Run ID 2147, Sept.20-21, 2004. Black marks are TES geolocations. Orbits of Terra and Aura have equator ascending crossing times of about 9:30 am and 1:45 pm respectively.

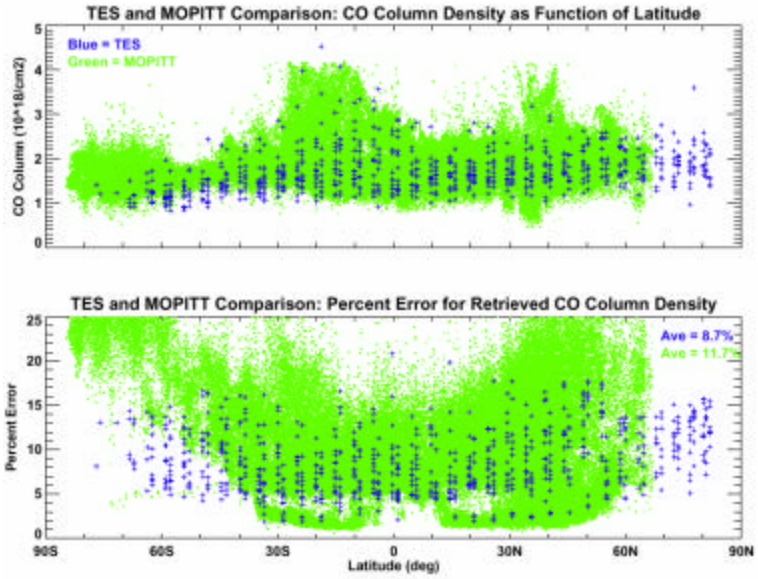

Figure 93: The top panel shows the comparisons of TES and MOPITT total CO columns as functions of Latitude for TES Run ID 2147, Sept.20-21, 2004. Note that TES CO column is visibly lower than that of MOPITT in Southern high latitudes. The bottom panel is the percent errors in TES and MOPITT CO columns. The global average values of their percent errors are 8.7% for TES and 11.7% for MOPITT, respectively.

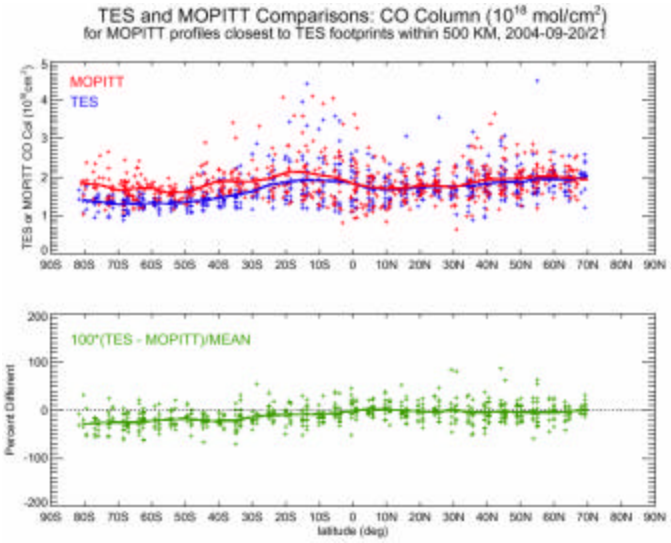

Figure 94: The closest MOPITT CO profile to a given TES CO measurement is selected within 500 km of TES location in a same day of observation, September 20-21, 2004. The top panel shows TES total CO column in blue and the selected MOPITT total CO column in red as functions of latitude. The solid lines are the averages in a latitude dependent +/- 5^{o} latitude box for the two instruments respectively. Lower TES CO in southern latitudes is clearly seen.

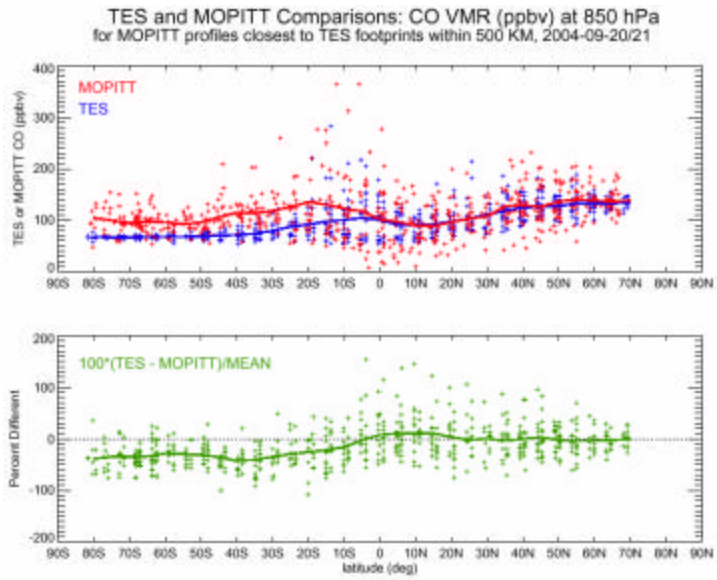

Figure 95: Similar to Figure 94, except the CO values are their volume mixing ratios (VMR) at 850 hPa. TES CO profiles are interpolated to the six MOPITT CO pressure levels for these plots. TES CO VMRs are seen lower than that of MOPITT in the southern hemisphere here. The comparisons at 700 hPa show a similar bias in southern hemisphere (not shown).

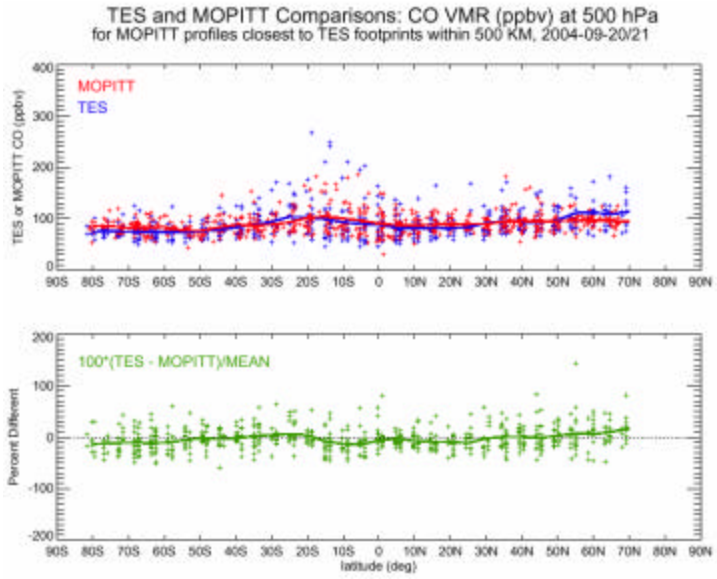

Figure 96: Same as Figure 95, for 500 hPa. Similarly good agreement is also seen in 350 hPa and 250 hPa comparisons (not shown here).

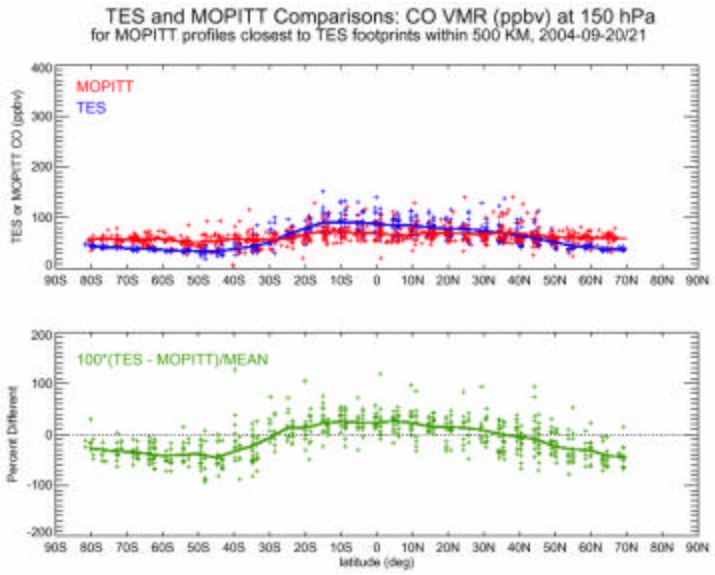

Figure 97: Same as Figure 95, for 150 hPa. The bias between TES and MOPITT CO VMR at this upper troposphere level shows latitudinal dependences.

9.2 Comparisons between TES and Aircraft Data (Argus)

During the October-November 2004 Aura Validation Experiment (AVE) aircraft campaign near Houston, TX, TES made step and stare nadir observations between equator and 60°N along Aura orbits. Table 4 lists information about the aircraft tracks and TES measurements for five comparison days.

Date		Oct. 31	Nov. 3	Nov. 5	Nov. 7	Nov. 9
TES Run		2262	2282	2290	2298	2305
Distance to Argus (km)	Takeoff/ Landing	560-100	160-170	130-20	410-270	700-420
	Diving	10-15	130-150	60-150		20-200
Time from Argus (hours)	Takeoff/ Landing	2.0 & 2.5	2.5 & 2.2	1.9 & 2.7	2.0 & 2.5	3.0 & 1.7
	Diving	0.5-1.5	0.4-1.0	0.4-1.3		(-1.0)-0.75
dofs of TES	Takeoff/ Landing	1.3	1.2-1.0	1.2	1.2	1.2-1.3
	Diving	1.3	1.2	1.2		1.1

Cloud OD of TES	Takeoff/ Landing	<0.1	<0.1 – 10.	<0.1	<0.1	<0.1
	Diving	<0.1	<0.1	<0.1		<0.6

Table 4: This table includes information pertaining to TES – Aircraft comparisons for the AVE 2004 campaign near Houston, TX.

The Argus instrument on the WB-57 aircraft is a two channel, tunable diode laser instrument setup for simultaneous, *in situ* measurement of CO and CH_4 in the troposphere and lower stratosphere. As an example, Figure 98 shows the WB-57 flight track in four different views for October 31 flight. The TES footprints are also show in the region where WB-57 track overlaps with the Aura track. It is very difficult to obtain coincident profile measurements both in geographic location and time for satellite and *in situ* observations.

TES CO measurements made on October 31 are presented by a curtain plot shown in Figure 99. Overlaid is the flight track along which Argus made *in situ* CO measurements. Measurements of CO made by Argus are qualitatively in good agreement with profiles retrieved by TES (Figure 100).

All Argus CO profiles taken during aircraft takeoff/landing and dives are compared with selected TES profiles. For each Argus profile, 4-6 TES profiles are selected that are closest in distance to the Argus profile location area. These TES profiles are also retrieved with a *dofs* of about 1.2-1.3 and small effective optical depth for cloud.

Figure 101 shows TES CO profiles with retrieval errors and the Argus takeoff/landing profiles for October 31 flight. The Argus profiles are then vertically smoothed with rows of TES CO averaging kernel, also in the figure: $x_{Argus\_withA} = Ax_{Argus} + (I - A)x_a$. The percent differences between all TES profiles and these Argus smoothed profiles are shown. The same procedure is used for Argus CO profiles taken during the aircraft profiling period as shown in Figure 102 In this case, the Argus profiles were extended downward/upward with the shifted TES *a priori* profile before applying TES averaging kernel to them.

In five days of aircraft flights, a total of 18 Argus CO profiles are compared with 4-6 TES CO profiles for each of them. The percent differences for these comparisons and some statistics for Argus and TES measurements are summarized in Figure 103. In conclusion, the differences between Argus and TES CO profiles are within TES retrieval errors and equivalent to CO spatial/temporal variability detected in both TES and Argus measurements.

We would like to acknowledge the Argus team at NASA Ames Research Center for participating in the AVE campaigns and providing their data.

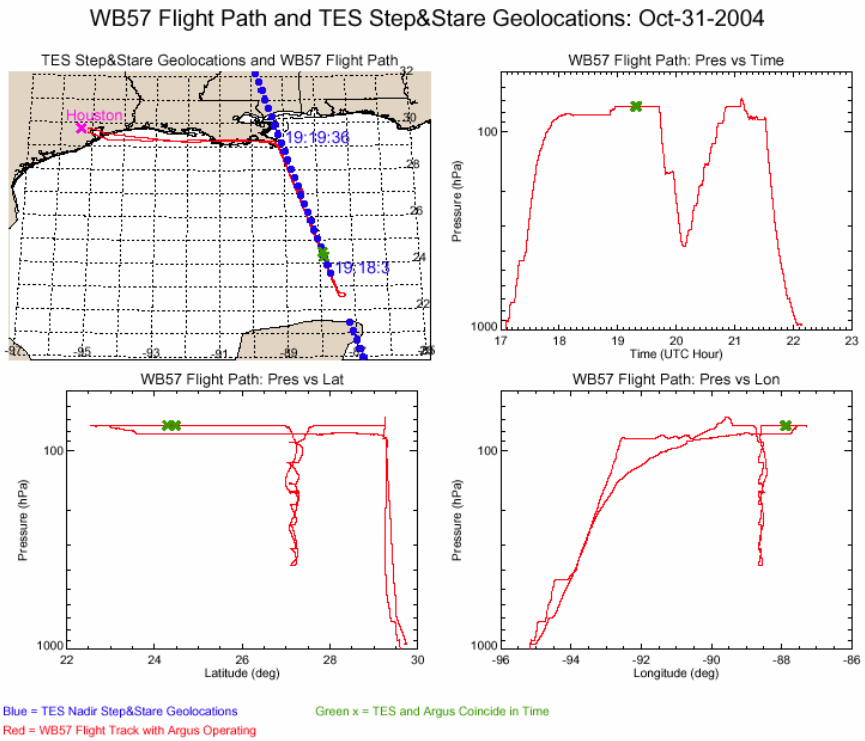

Figure 98: For one day (October 30, 2004) during AVE-04 campaign, plots show the WB-57 flight track in red and a fraction of TES step and stare observation geolocations in blue plotted in four different ways. The green cross marks the start and end points when TES made the nadir observations along a portion of the aircraft track.

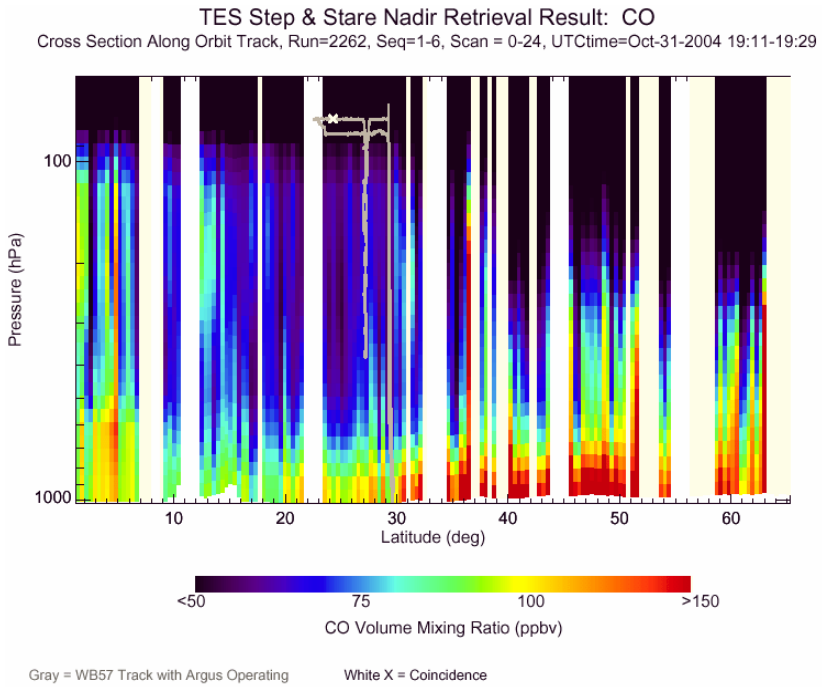

Figure 99: The cross section of TES CO profiles along its orbit track from equator to 63°N latitude, from a step and stare special observation on October 31, 2004. The flight pressures of WB-57 as a function of latitude are overlaid in gray.

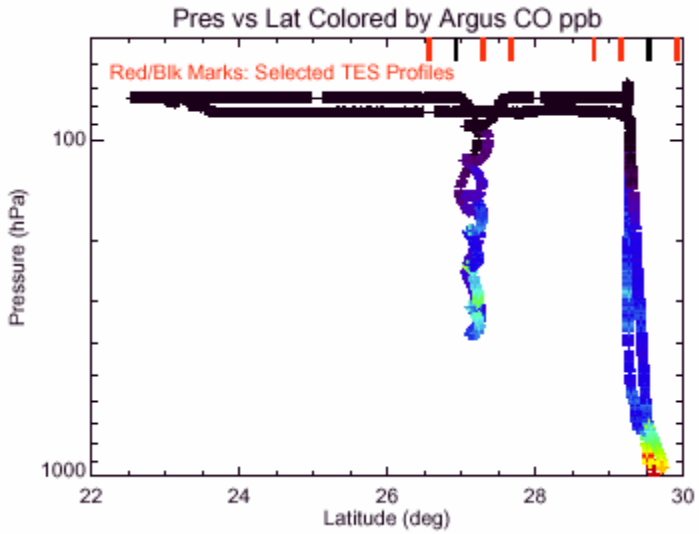

Figure 100: The Argus measurements of CO VMR plotted along the flight track in comparison to that of TES in Figure 98for October 31, 2004. Several TES profiles are chosen for comparisons as their latitudes marked by red or black bars on top.

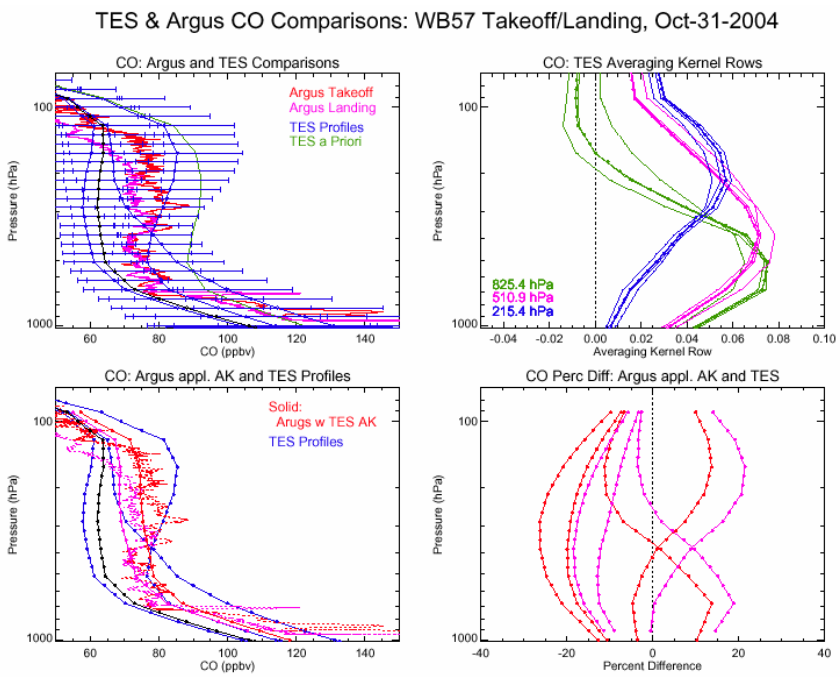

Figure 101: CO profile comparisons between TES and Argus takeoff and landing measurements taken on October 31, 2004. Shown in top left panel are the Argus CO profiles, the four TES CO profiles (blue or black) with error bars, and the a priori profile (green) used for these TES retrievals. The top right panel shows the rows of TES averaging kernels at three pressure levels. The bottom left panel shows TES and Argus profiles again and the vertically smoothed profiles for Argus CO measurements with TES averaging kernel and a priori profile applied described in detail in the text. The bottom right panel shows the percent differences between the four TES CO profiles and the two vertically smoothed Argus CO profiles.

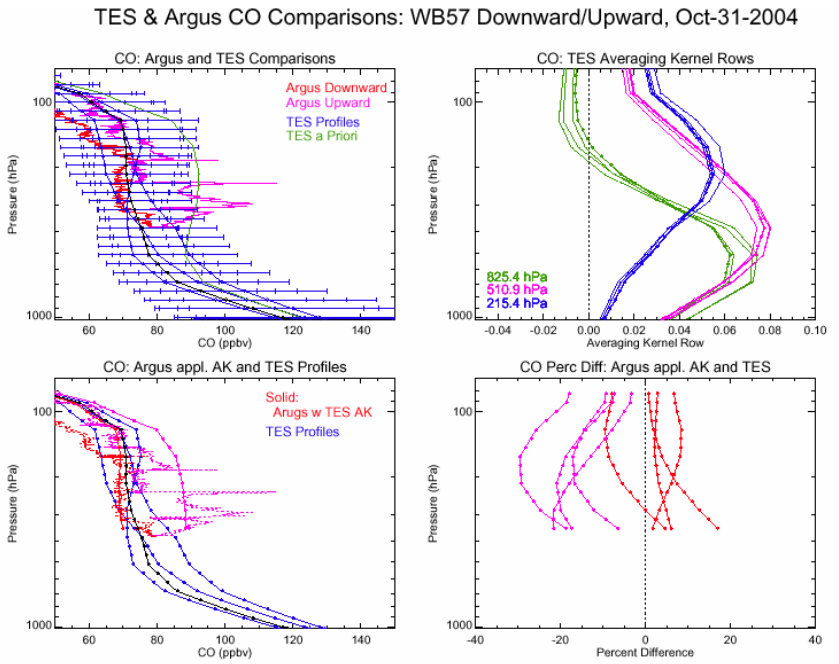

Figure 102: Same as Figure 13, except that the Argus CO profiles are from the profiling portion of the flight. For this case, before applying the averaging kernel to the Argus profiles, they are extended downward with shifted TES a priori profile.

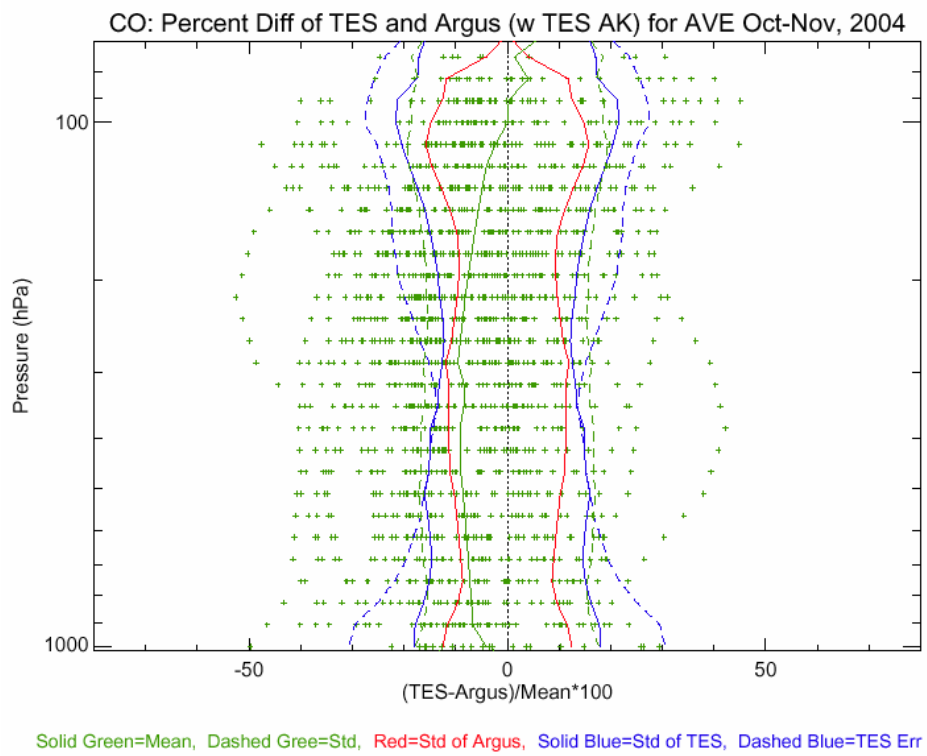

Figure 103: Percent differences between TES and Argus CO profiles from all five days of measurements during AVE-04 WB-57 campaign listed in Table 1. The solid green is the mean of all comparisons. The other curves are plotted with respect to zero: the standard deviation (STD) of all percent difference (dashed green), the STD of all Argus measurements (red), the STD of all TES (solid blue), and the averaged percent error for the TES measurements (dashed blue).

9.3 Latitudinal Structure of Carbon Monoxide: Comparisons with GEOS-Chem

GEOS-Chem and TES data show the same broad latitudinal structure in CO at all altitudes and consistent inter-hemispheric gradients. Latitudinal variability in TES CO is strongly related to that of the *a priori*, although deviations are found in regions where TES sensitivity is high, for example in the mid troposphere over tropical latitudes. TES CO data exhibit a generally positive bias with respect to GEOS-Chem, which increases from 5% at the surface reflecting the strong *a priori* influence on the GEOS-Chem data after the application of the TES averaging kernels, to 13.5% in the mid-upper troposphere where TES sensitivity is greater. The bias also shows a latitudinal dependence with the largest values observed in the southern tropics where, at this time of year, biomass burning is occurring leading to high CO concentrations.

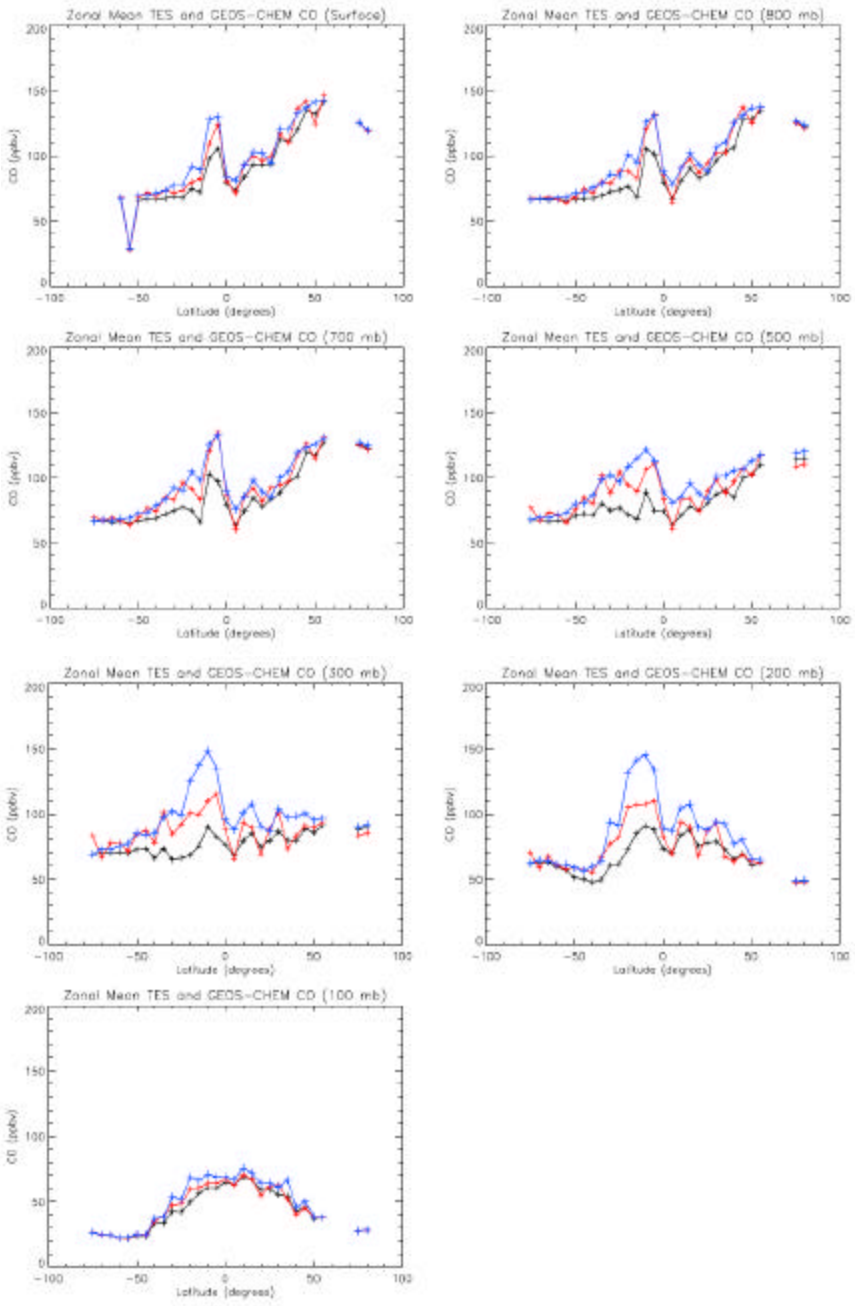

Figure 104: TES (Red), GEOS-Chem (black) and TES a priori (blue) zonal mean CO profiles for TES Run ID 2147 (September 20/21 2004). Both TES and the transformed GEOS-Chem profiles are averaged over all longitudes into 5 degree latitude bins to obtain zonal mean profiles for comparison.

9.4 Conclusions and Future Work

The global distribution characteristics of TES observed CO at tropospheric levels and total column agree well qualitatively with that of MOPITT observations, *e.g.*, elevated CO in biomass burning or other pollution source regions in the lower troposphere. TES and MOPITT CO in the mid-troposphere agree within 10% where the retrievals of both instruments are most sensitive to their measured signals. Near the surface and tropopause or at high latitudes, TES and MOPITT displayed larger disagreements and they are believed due to the greater influences of different *a priori* CO profiles and constraints used in retrievals of the two instruments respectively. This effect will be examined in future studies. The comparisons of TES and the "vertically smoothed" Argus *in situ* CO profiles indicate reasonable agreement within TES measurement errors and the CO variability shown in both set of measurements.

Future validation of TES CO product will include expanded comparisons with MOPITT data over periods of different seasons and comparisons with AIRS retrievals of CO. More correlative CO profiles obtained from aircraft, ground-based solar occultation, surface *in situ* sampling measurements in both hemispheres and different seasons (*e.g.*, CMDL) are also sources for future validation of TES CO retrievals.

10 Future Work for Validation of TES Data

All of the work discussed in this report is being continued beyond the "launch + 1 year" time frame. More data sets are being incorporated into the validation effort. We intend to update this document on a regular basis to inform potential data users of the validation status of the TES data. Furthermore, additional species in the nadir and limb products will be included in future reports.

11 References

Aumann, H.H., M.T. Chahine, C. Gautier, M.D. Goldberg, E. Kalnay, L.M. McMillin, H. Revercomb, P.W. Rosenkranz, W.L. Smith, D.H. Staelin, L.L. Strow, and J. Susskind, AIRS/AMSU/HSB on the aqua mission: Design, science objectives, data products, and processing systems, Ieee Transactions on Geoscience and Remote Sensing, 41 (2), 253-264, 2003.

Beer, R., T. A. Glavich, and D. M. Rider, Tropospheric emission spectrometer for the Earth Observing System's Aura satellite, Appt. Opt., 40(15), 2356-2367, 2001.

Beer, R., TES on the Aura Mission: Scientific Objectives, Measurements and Analysis Overview, IEEE Transactions on Geoscience and Remote Sensing, 2005.

Best, F. A., H. E. Revercomb, D. D. LaPorte, R. O. Knuteson, and W. L. Smith, Accurately calibrated airborne and ground-based Fourier transform spectrometers II: HIS and AERI calibration techniques, traceability, and testing, In Proceedings of the Council for Optical Radiation measurements (CORM) 1997 Annual Meeting, National Institute of Standards and Technology (NIST), Gaithersburg, MD, 1997.

Best, F. A., H. E. Revercomb, R. O. Knuteson, D. C. Tobin, R. G. Dedecker, T. P. Dirkx, M. P. Mulligan, N. N. Ciganovich, and Y. Te, Traceability of Absolute Radiometric Calibration for the Atmospheric Emitted Radiance Interferometer (AERI), In Proceedings of the 2003 Conference on Characterization and Radiometric Calibration for Remote Sensing, September 15 to 18, 2003, Utah State University, Space Dynamics Laboratory, Logan, Utah, 2003.

Bey I., D.J. Jacob, R.M. Yantosca, J.A. Logan, B.D. Field, A.M. Fiore, Q. Li, H. Liu, L.J. Mickley, and M.G. Schultz, Global modeling of tropospheric chemistry with assimilated meteorology: Model description and evaluation, J. Geophys. Res., 106, 23,073-23,09, 2001.

Bowman, K., C. D. Rodgers, S. S. Kulawik, J. Worden et al., Tropospheric Emission Spectrometer: Retrieval method and error analysis, IEEE Transactions on Geoscience and Remote Sensing, 2005.

Bowman Kevin, Clive D. Rodgers, Susan Sund-Kulawik, John Worden, Edwin Sarkissian, Greg Osterman, Tilman Steck, Ming Lou, Annmarie Eldering, Mark Shepherd, Helen Worden, Michael Lampel, Shepherd Clough, Pat Brown, Curtis Rinsland, Michael Gunson, Reinhard Beer, "Tropospheric Emission Spectrometer: Retrieval Method and Error Analysis", submitted to IEEE TGARS Aura special issue, May 2005.

Deeter, M. N., L. K. Emmons, D. P. Edwards, J. C. Gille, and J. R. Drummond, 2004, Vertical resolution and information content of CO profiles retrieved by MOPITT, Geophys. Res. Lett., 31, L15112, doi:10.1029/2004GL020235.

Hagan D. and P. Minnett, "AIRS Radiance Validation Over Ocean From Sea Surface Temperature Measurements", IEEE Trans. Geosci. Remote Sensing, vol 41, pp. 432-441, Feb. 2003.

Jones, D. B. A., K. W. Bowman, P. I. Palmer, J. R. Worden, D. J. Jacob, R. N. Hoffman, I. Bey, and R. M. Yantosca, Potential of observations from the Tropospheric Emission Spectrometer to constrain continental sources of carbon monoxide, J. Geophys. Res., 108(D24), 4789, doi:10.1029/2003JD003702, 2003.

Knuteson, R. O., H. E. Revercomb, F. A. Best, N. C. Ciganovich, R. G. Dedecker, T. P. Dirkx, S. C. Ellington, W. F. Feltz, R. K. Garcia, H. B. Howell, W. L. Smith, J. F. Short, and D. C. Tobin, Atmospheric Emitted Radiance Interferometer. Part I: Instrument Design, J. Atmos. Ocean. Tech., 21, 1763-1776, 2004a.

Knuteson, R. O., H. E. Revercomb, F. A. Best, N. C. Ciganovich, R. G. Dedecker, T. P. Dirkx, S. C. Ellington, W. F. Feltz, R. K. Garcia, H. B. Howell, W. L. Smith, J. F. Short, and D. C. Tobin, Atmospheric Emitted Radiance Interferometer. Part II: Instrument Performance, J. Atmos. Ocean. Tech., 21, 1777-1789, 2004b.

Kulawik, S. S., H. Worden, G. Osterman, M. Luo, B. Beer, et al., TES Atmospheric Profile Retrieval Characterization: An obit of simulated observations, IEEE Transactions on Geosciecne and Remote Sensing, 2005.

Li, Q., D. J. Jacob, et al., A tropospheric ozone maximum over the Middle East, Geophys. Res. Lett., 28, 3235-3238, 2001.

Liu, H., D.J. Jacob, L.Y. Chan, S.J. Oltmans, I. Bey, R.M. Yantosca, J.M. Harris, B.N. Duncan, and R.V. Martin, Sources of tropospheric ozone along the Asian Pacific Rim: An analysis of ozonesonde observations, J. Geophys. Res., 107, 4573, 2002.

Martin, R.V., D.J. Jacob, et al., Interpretation of TOMS observations of tropical tropospheric ozone with a global model and in-situ observations, J. Geophys. Res., 107, 4351, 2002.

May, R. D., Open-path, near-infrared tunable diode laser spectrometer for atmospheric measurements of H2O, J. Geophys. Res., 103, 19161-72, 1998.

Minnett, P. J., R. O. Knuteson, F. A. Best, B. J. Osborne, J. A. Hanafin, and O. B. Brown, The Marine-Atmospheric Emitted Radiance Interferometer (M-AERI), a high-accuracy, sea-going infrared spectroradiometer, J. Atmos. and Ocean. Tech., 18, 994-1013, 2001.

Moncet, J.L., and S.A. Clough, Accelerated monochromatic radiative transfer for scattering atmospheres: Application of a new model to spectral radiance observations, Journal of Geophysical Research-Atmospheres, 102 (D18), 21853-21866, 1997.

Pagano T. S., H. H. Aumann, D. Hagan and K. Overoye, "Prelaunch and In-Flight Radiometric Calibration of the Atmospheric Infrared Sounder (AIRS)." IEEE Trans. Geosci. Remote Sensing, vol 41, pp. 265-273, Feb. 2003.

Revercomb, H. E., D. D. LaPorte, W. L. Smith, H. Buijs, D. G. Murcray, F. J. Murcray, and L.A. Sromovsky, High-Altitude Aircraft Measurements of Upwelling IR Radiance: Prelude to FTIR from Geosynchronous Satellite. Mikrochimica Acta [Wien], II, 439-444, 1988b.

Revercomb, H. E., W. L. Smith, F. A. Best, J. Giroux, D. D. LaPorte, R. O. Knuteson, M. W. Werner, J. R. Anderson, N. N. Ciganovich, R. W. Cline, S. D. Ellington, R. G. Dedecker, T. P. Dirkx, R. K. Garcia, and H. B. Howell, Airborne and ground-based Fourier transform spectrometers for meteorology: HIS, AERI and the new AERI-UAV. Proceedings SPIE Optical Instruments for Weather Forecasting, ed. G.W. Kamerman, 2832, 106-117, 1996.

Revercomb, H., H. Buijs, D. L. H.B. Howell, W. Smith, and L. Sromovsky, Radiometric calibration of IR Fourier transform spectrometers: solution to a problem with the high-resolution interferometer sounder, Appl. Opt., 27, 3210, 1988a.

Rodgers 2000-Clive D. Rodgers, Inverse Methods for Atmospheric Sounding: Theory and Practice, World Scientific Pub, 2000

Rodgers C. D. and B. Conners, "Intercomparison of remote sounding instruments," J. Geophys. Res., vol. 108(D3), p. 4119, 2003.

Rodgers, C.D., Inverse Methods for Atmospheric Sounding: Theory and Practice, World Scientific, Singapore, 2000.

Susskind, J., C.D. Barnet, and J.M. Blaisdell, Retrieval of atmospheric and surface parameters from AIRS/AMSU/HSB data in the presence of clouds, Ieee Transactions on Geoscience and Remote Sensing, 41 (2), 390-409, 2003.

Tobin, D. C, H. E. Revercomb, R. O. Knuteson, On-orbit Spectral Calibration of the Geosynchronous Imaging Fourier Transform Spectrometer (GIFTS), In Proceedings of the 2003 Conference on Characterization and Radiometric Calibration for Remote Sensing, September 15 to 18, 2003, Utah State University, Space Dynamics Laboratory, Logan, Utah, 2003.

Tobin, D. C., H. E. Revercomb, C. C. Moeller, and T. S. Pagano, Use of AIRS high spectral resolution infrared spectra to assess the calibration of MODIS on EOS Aqua, J. Geophys. Res., 2005, in press.

Tobin, D. C., H. E. Revercomb, R. O. Knuteson, F. A. Best, W. L. Smith, P. van Deslt, D. D. LaPorte, S. D. Ellington, M. W. Werner, R. G. Dedecker, R. K. Garcia, N. N. Ciganovich, H. B. Howell, S. B. Dutcher, J. K. Taylor, K. Vinson, T. S. Pagano, S. A. Mango, Radiometric and Spectral Validation of AIRS Observations with the Aircraft based Scanning High resolution Interferometer Sounder, J. Geophys. Res., 2005, submitted.

Worden J., S. S. Kulawik, M. Shepard, S. Clough, H. Worden, K. Bowman, and A. Goldman, "Predicted errors of Tropospheric Emission Spectrometer nadir retrievals from spectral window selection," J. Geophys. Res., vol. 109, no. D09308, May 2004.

Worden, J., et al., Predicted errors of tropospheric emission spectrometer nadir retrievals from spectral window selection, J. Geophys. Res., 109, D09308, 2004.

12 Appendix: TES Run ID, Observation Types and Dates

TES Run ID	Start Date	End Date	TES Observation Type
2026	22-Aug-04	22-Aug-04	Mini Global Survey
2044	24-Aug-04	25-Aug-04	Mini Global Survey
2092	3-Sep-04	4-Sep-04	Mini Global Survey
2135	18-Sep-04	18-Sep-04	Mini Global Survey
2147	20-Sep-04	21-Sep-04	Global Survey
2151	21-Sep-04	21-Sep-04	Step & Stare
2163	22-Sep-04	22-Sep-04	Step & Stare
2195	9-Oct-04	10-Oct-04	Global Survey
2199	11-Oct-04	11-Oct-04	Step & Stare
2202	13-Oct-04	14-Oct-04	Global Survey
2207	15-Oct-04	16-Oct-04	Global Survey
2210	16-Oct-04	16-Oct-04	Step & Stare
2219	20-Oct-04	20-Oct-04	Step & Stare
2222	20-Oct-04	20-Oct-04	Step & Stare
2228	21-Oct-04	21-Oct-04	Step & Stare
2256	30-Oct-04	30-Oct-04	Step & Stare
2262	31-Oct-04	31-Oct-04	Step & Stare
2269	1-Nov-04	1-Nov-04	Step & Stare
2275	2-Nov-04	2-Nov-04	Step & Stare
2282	3-Nov-04	3-Nov-04	Step & Stare
2286	4-Nov-04	5-Nov-04	Global Survey
2290	5-Nov-04	5-Nov-04	Step & Stare
2294	6-Nov-04	7-Nov-04	Global Survey
2298	7-Nov-04	7-Nov-04	Step & Stare
2302	8-Nov-04	9-Nov-04	Global Survey
2305	9-Nov-04	9-Nov-04	Step & Stare
2310	10-Nov-04	11-Nov-04	Global Survey
2313	11-Nov-04	11-Nov-04	Step & Stare
2317	12-Nov-04	13-Nov-04	Global Survey
2321	13-Nov-04	13-Nov-04	Step & Stare
2324	13-Nov-04	13-Nov-04	Step & Stare
2328	14-Nov-04	15-Nov-04	Global Survey
2332	15-Nov-04	15-Nov-04	Step & Stare
2336	16-Nov-04	17-Nov-04	Global Survey
2345	21-Nov-05	21-Nov-05	Global Survey
2352	26-Nov-04	27-Nov-04	Global Survey
2357	28-Nov-04	29-Nov-04	Global Survey
2362	30-Nov-04	1-Dec-04	Global Survey

TES Run ID	Start Date	End Date	TES Observation Type
2367	2-Dec-04	3-Dec-04	Global Survey
2372	4-Dec-04	5-Dec-04	Global Survey
2377	6-Dec-04	7-Dec-04	Global Survey
2410	10-Dec-04	11-Dec-04	Global Survey
2414	12-Dec-04	13-Dec-04	Global Survey
2418	14-Dec-04	15-Dec-04	Global Survey
2423	16-Dec-04	17-Dec-04	Global Survey
2428	18-Dec-04	19-Dec-04	Global Survey
2433	20-Dec-04	21-Dec-04	Global Survey
2439	22-Dec-04	23-Dec-04	Global Survey
2443	24-Dec-04	25-Dec-04	Global Survey
2448	26-Dec-04	27-Dec-04	Global Survey
2453	28-Dec-04	29-Dec-04	Global Survey
2458	30-Dec-04	31-Dec-04	Global Survey
2463	1-Jan-05	2-Jan-05	Global Survey
2468	3-Jan-05	4-Jan-05	Global Survey
2476	9-Jan-05	10-Jan-05	Global Survey
2481	11-Jan-05	12-Jan-05	Global Survey
2486	13-Jan-05	14-Jan-05	Global Survey
2491	15-Jan-05	16-Jan-05	Global Survey
2496	17-Jan-05	18-Jan-05	Global Survey
2501	19-Jan-05	20-Jan-05	Global Survey
2506	21-Jan-05	22-Jan-05	Global Survey
2509	22-Jan-05	22-Jan-05	Step & Stare
2512	22-Jan-05	22-Jan-05	Step & Stare
2515	22-Jan-05	22-Jan-05	Step & Stare
2519	22-Jan-05	22-Jan-05	Step & Stare
2522	22-Jan-05	22-Jan-05	Step & Stare
2525	23-Jan-05	23-Jan-05	Step & Stare
2529	23-Jan-05	23-Jan-05	Step & Stare
2532	23-Jan-05	23-Jan-05	Step & Stare
2535	23-Jan-05	24-Jan-05	Global Survey
2538	24-Jan-05	24-Jan-05	Step & Stare
2542	24-Jan-05	24-Jan-05	Step & Stare
2545	24-Jan-05	24-Jan-05	Step & Stare
2548	24-Jan-05	24-Jan-05	Step & Stare
2551	24-Jan-05	24-Jan-05	Step & Stare
2554	24-Jan-05	24-Jan-05	Step & Stare
2558	25-Jan-05	25-Jan-05	Step & Stare
2561	25-Jan-05	25-Jan-05	Step & Stare
2564	25-Jan-05	25-Jan-05	Step & Stare
2567	25-Jan-05	25-Jan-05	Step & Stare
2570	25-Jan-05	26-Jan-05	Global Survey
2573	26-Jan-05	26-Jan-05	Step & Stare

TES Run ID	Start Date	End Date	TES Observation Type
2576	26-Jan-05	26-Jan-05	Step & Stare
2579	26-Jan-05	26-Jan-05	Step & Stare
2584	27-Jan-05	28-Jan-05	Global Survey
2587	28-Jan-05	28-Jan-05	Limb Special Obs
2592	29-Jan-05	30-Jan-05	Global Survey
2597	31-Jan-05	1-Feb-05	Global Survey
2601	1-Feb-05	1-Feb-05	Step & Stare
2604	1-Feb-05	1-Feb-05	Step & Stare
2608	2-Feb-05	3-Feb-05	Global Survey
2611	3-Feb-05	3-Feb-05	Step & Stare
2614	3-Feb-05	3-Feb-05	Step & Stare
2619	4-Feb-05	5-Feb-05	Global Survey
2622	5-Feb-05	5-Feb-05	Step & Stare
2625	5-Feb-05	5-Feb-05	Step & Stare
2630	6-Feb-05	7-Feb-05	Global Survey
2633	7-Feb-05	7-Feb-05	Step & Stare
2637	7-Feb-05	7-Feb-05	Step & Stare
2649	10-Feb-05	11-Feb-05	Global Survey
2654	12-Feb-05	13-Feb-05	Global Survey
2657	13-Feb-05	13-Feb-05	Step & Stare
2660	13-Feb-05	13-Feb-05	Step & Stare
2664	13-Feb-05	13-Feb-05	Step & Stare
2668	14-Feb-05	15-Feb-05	Global Survey
2671	15-Feb-05	15-Feb-05	Step & Stare
2674	15-Feb-05	15-Feb-05	Step & Stare
2677	15-Feb-05	15-Feb-05	Step & Stare
2681	16-Feb-05	17-Feb-05	Global Survey
2684	17-Feb-05	17-Feb-05	Step & Stare
2687	17-Feb-05	17-Feb-05	Step & Stare
2690	17-Feb-05	17-Feb-05	Step & Stare
2695	19-Feb-05	19-Feb-05	Global Survey
2698	19-Feb-05	19-Feb-05	Step & Stare
2701	19-Feb-05	19-Feb-05	Step & Stare
2705	19-Feb-05	19-Feb-05	Step & Stare
2709	20-Feb-05	21-Feb-05	Global Survey
2712	21-Feb-05	21-Feb-05	Step & Stare
2715	21-Feb-05	21-Feb-05	Step & Stare
2719	21-Feb-05	21-Feb-05	Step & Stare
2723	22-Feb-05	23-Feb-05	Global Survey
2726	23-Feb-05	23-Feb-05	Step & Stare
2730	23-Feb-05	23-Feb-05	Step & Stare
2733	23-Feb-05	23-Feb-05	Step & Stare
2738	24-Feb-05	25-Feb-05	Global Survey
2741	25-Feb-05	25-Feb-05	Step & Stare

TES Run ID	Start Date	End Date	TES Observation Type
2744	25-Feb-05	25-Feb-05	Step & Stare
2749	27-Feb-05	27-Feb-05	Global Survey
2752	27-Feb-05	27-Feb-05	Step & Stare
2755	27-Feb-05	27-Feb-05	Step & Stare
2759	27-Feb-05	27-Feb-05	Step & Stare
2766	4-Mar-05	5-Mar-05	Global Survey
2771	6-Mar-05	7-Mar-05	Global Survey
2776	8-Mar-05	9-Mar-05	Global Survey
2781	10-Mar-05	11-Mar-05	Global Survey
2786	12-Mar-05	13-Mar-05	Global Survey
2791	14-Mar-05	15-Mar-05	Global Survey
2796	16-Mar-05	17-Mar-05	Global Survey
2801	18-Mar-05	19-Mar-05	Global Survey
2805	20-Mar-05	21-Mar-05	Global Survey
2810	22-Mar-05	23-Mar-05	Global Survey
2815	24-Mar-05	25-Mar-05	Global Survey
2820	26-Mar-05	27-Mar-05	Global Survey
2825	28-Mar-05	29-Mar-05	Global Survey
2829	29-Mar-05	29-Mar-05	Stare - PNNL
2833	30-Mar-05	31-Mar-05	Global Survey
2836	31-Mar-05	31-Mar-05	Stare - PNNL
2841	1-Apr-05	2-Apr-05	Global Survey
2846	3-Apr-05	4-Apr-05	Global Survey
2851	5-Apr-05	6-Apr-05	Global Survey
2856	7-Apr-05	8-Apr-05	Global Survey
2861	9-Apr-05	10-Apr-05	Global Survey
2931	21-May-05	22-May-05	Global Survey
2935	23-May-05	24-May-05	Global Survey
2939	25-May-05	26-May-05	Global Survey
2945	4-Jul-05	5-Jul-05	Global Survey
2949	6-Jul-05	7-Jul-05	Global Survey
2952	8-Jul-05	9-Jul-05	Global Survey
2956	10-Jul-05	11-Jul-05	Global Survey
2960	12-Jul-05	13-Jul-05	Global Survey

Table 5: List of TES Run ID and the corresponding dates and observation type through July 13, 2005.

13 Appendix: Validation Status Definitions

We used definitions similar to other EOS instruments to describe the validation status of TES data. The definition for AIRS and for Terra products can be found at:

http://disc.gsfc.nasa.gov/AIRS/airs_whom_disclaimer.shtml

http://eosdatainfo.gsfc.nasa.gov/eosdata/terra/terra_dataprod.html

Beta -- Early release product, minimally validated and may still contain significant errors. This version of the data allows users to gain familiarity with data formats and how to properly use the data. The data is generally not appropriate as the basis for quantitative scientific publications.

Provisional -- Product quality may not be optimal and incremental product improvements are still occurring. General research community is encouraged to participate in the QA and validation of the product, but need to be aware that product validation and QA are ongoing. Users are urged to contact science team representatives prior to use of the data in publications.

Validated -- Formally validated product, although validation is still ongoing. Uncertainties are well defined, and products are ready for use in scientific publications, and by other agencies. There may be later improved versions of these products.